Advantages of Singular Configurations in Robot Motion

Wan, Xianglong

(Degree)
博士（工学）

(Date of Degree)
2016-03-25

(Date of Publication)
2017-03-01

(Resource Type)
doctoral thesis

(Report Number)
甲第6647号

(URL)
https://hdl.handle.net/20.500.14094/D1006647

Advantages of Singular Configurations in Robot Motion

Wan Xianglong

Department of Systems Science
Graduate School of System Informatics

Kobe University, Japan

This dissertation is submitted for the degree of

Doctor of Philosophy in Engineering

January, 2016

Abstract

In robotics, a robot configuration that has a degenerated Jacobian matrix is called singular configuration. The kinematic properties of singular configurations are well-studied. In a singular configuration, the robot end-effector loses one or more degrees of freedom, and cannot be freely controlled in each direction. For this reason, many control and motion planning strategies have been used to avoid the singularities. However, these strategies lead to a complex control and motion-planning process, and a restricted range of feasible tasks.

As we know, everything has two sides. Some researches showed that singular configurations are advantageous in several robot motions, even though the advantage has been neglected for a long time. To give an explanation of the advantage, it is necessary to examine the dynamics near the singular configurations. Serial manipulators are commonly utilized in industry and faculty, and the understanding of the corresponding dynamics is very important. The investigation of the dynamics of serial manipulators near the singular configurations is the main emphasis in this dissertation. This dissertation summarizes the features of singular configurations. Two of them have been observed and theoretically explained in previous studies. To theoretically analyze the rest of the features, a two-link manipulator with a heavy object grasped at the end-effector is considered. This dissertation focuses on how to accelerate the heavy object efficiently. The acceleration of the object is divided into three components, torque-dependent, gravity-dependent and velocity-dependent accelerations. These correspond to three terms including joint torques, gravity and joint velocities in the equations of motion of the object respectively. Each component of acceleration of the object is approximately expressed by the function of joint angle under several assumptions. The behavior of the approximate expressions with different postures can clearly explain the rest of the features.

The goal of this dissertation is to understand how to utilize the features in robot motions. The ideas gained from these studies will be useful for making a robot perform highly dynamic motions from a practical viewpoint. This dissertation pays attention to some dynamic motions, including lifting motions of a two-link robot manipulator, dragging motions of a two-link mobile manipulator, jumping motions of two/four-link legged robots and landing motions of a four-link legged robot. A heavy object or body is considered to be strongly moved by a manipulator or leg in a limited time. For each dynamic motion, the optimal one that minimizes

the necessary joint torques is obtained by numerical optimization. Simulation results show that the features of singular configurations are utilized in the obtained motions to reduce the necessary joint torques. From the simulation results, the way of using the features in each motion is also clarified.

I would like to dedicate this dissertation to my loving family.

To EVA

Acknowledgements

I would like to thank my advisors, Professor Takateru Urakubo and Professor Yukio Tada, for giving me the chance to do this work, and for the guidance. Especially I would like to express my deepest gratitude to Professor Urakubo for the many helpful technical discussions and for his many useful suggestions and advices on my research. Many thanks to Professor Zhiwei Luo for thoughtful discussion, and to Professor Hideki Sano for careful review of my Ph.D. dissertation. I am grateful to Professor Tomoaki Mashimo for assistance in building experimental equipment. Further thanks go to all the members in CS22 as well as my many good friends.

Contents

Chapter 1

Introduction

1.1 Background

The development of the robots that can perform human-like movements has attracted many researchers [1–3]. Over the past decades, researchers have proposed several robot manipulators to perform highly dynamic tasks such as grasping [4–7], batting [8–10] and throwing [11–14] by their end-effectors. The lifting motion performed by the robots in behalf of us has been studied well [15, 16].

Mobile manipulators are expected to perform various tasks by using the manipulator fitted on the mobile platform [17, 18]. In [17], a quadruped robot (BigDog) with a manipulator has successfully performed lifting and throwing heavy objects. Due to fukushima daiichi nuclear disaster [19], the mobile manipulators that can work in unknown and dangerous environment instead of human beings attract the interest of many researchers recently [20, 21]. Mobile manipulators have been used inside the fukushima daiichi reactor buildings for several purposes such as opening door and picking up debris.

Many of the robot manipulators (including the mobile ones) are equipped with the actuators with high performance. However, powerful actuators often have heavy weight, and may bring external energy consumption during robot motions, especially for the mobile robots which are powered by the batteries. When these mobile robots work in an unknown environment such as an earthquake rubble or a nuclear rubble, there should be enough remaining battery capacity for any emergency issue. If the tasks are performed efficiently even by small actuators, energy consumption can be reduced and the tasks can be achieved as much as possible before running out of batteries. Therefore, there is a pressing need to find a way of efficiently achieving dynamic tasks.

Several approaches to develop jumping robots have been proposed so far [22–26]. Most of them are based on the biological structure and biomechanics. In [22], biped robots with

musculoskeletal system are constructed to realize a jumping motion from take-off to stable landing. Dynamic movements such as walking, running and jumping need coordination of many degrees of freedom under the gravitational force and the ground reaction force, and are difficult for robots to perform. As we have known, when something is exerting force on the ground, the ground will push back with equal force in the opposite direction. If someone wants to jump, the gravity force and ground reaction force should act upon him or her in the period that the foot touches the ground, and the period is called "stance phase". When no part of him or her touches the ground, only gravity force acts in this case, and the period is called "aerial phase". The jumping motion can be divided into three parts, jumping (stance phase), floating (aerial phase) and landing (stance phase). If we want to jump higher vertically, we need to generate enough upward acceleration while overcoming gravity in stance phase. In other words, the jumping movement is a highly dynamic motion and needs a large amount of energy in a short time [27, 28]. Electro-magnetic actuators for robots could be saturated due to a torque limit during the jumping movement. To achieve the jumping movement within the torque limit, an efficient way of supplying the energy from the joint torques has to be adopted.

During a landing motion, large ground reaction force, called impact force, occurs due to the impact between the foot and the ground. Reducing the impact force (or momentum) is important for humans to prevent injuries and for robots to avoid mechanical breakdowns. When a robotic arm or leg collides with other object, the impact force caused by the collision depends on the configuration (posture) of the robot. The optimal configuration that minimizes the impact force can be calculated by using a mathematical model of the impact force. Two different impact force models have been considered in the references [29–31]. For the model in [29, 30], the impact with stiff objects occurs in an infinitesimally small period of time. The joint velocities and the momentum of the robot change discontinuously at the instant of collision. It is called discontinuous model in this dissertation. In [31], landing of a legged robot that has a foot equipped with a soft pad is considered. The soft pad generates a spring damper force between the foot and the ground. The impact through the pad occurs in a finite duration, and the changes in joint velocities and momentum of the robot are continuous. It is called continuous model in this dissertation. For both models, the configuration of the robot where the leg is bent, that is, the configuration far from the singular configuration where the leg is stretched out, is advantageous to reduce the impact force or momentum.

To complete a landing motion after the collision, joint torques of a legged robot have to bring the configuration to a stable stance and absorb the kinetic energy of the robot to stop the motion. The joint torques for human landing motion have been investigated so far. It was found in [32] that the joint stiffness alters during the ground contact phase in human hopping. The leg stiffness modulation is sensitive to changes in ankle joint stiffness [33]. Inspired

by those results, a body stiffness and damping control method has been proposed to achieve soft landing of a legged robot in [26]. Time varying stiffness and damping coefficients were optimized to reduce the peak value of ground reaction force. On the other hand, minimization of necessary joint torques during a landing motion is also important for reducing the energy consumption of joint motors. More importantly, the weight of the robot can be reduced by using small motors if the necessary joint torques are small. The lighter weight makes the realization of a jumping robot much easier.

Human beings can dexterously perform highly dynamic motions. For instance, we achieve efficient walk by utilizing the posture with extended knees and hips [34]. We push or pull a heavy object as a habitual and physically strenuous task. When we pull an extremely heavy object, we use our whole bodies. The translational momentum (or kinetic energy) of the trunk is generated before we apply a pulling force to the object with our hands, and then a large force is applied to the object near a configuration where the arm is fully extended. Human beings usually lift up heavy objects to a higher place in the daily life. In a weight lifting motion, an athlete lifts up a heavy barbell. The athlete firstly extends his arms and then suddenly starts to lift the barbell from the ground. After lifting it above his head, the body stretches to sustain the barbell. In a vertical jumping motion of human beings, the leg stretches rapidly in an aligned position in stance phase, and the take-off posture is almost stretched out. In these motions, the extended postures of human beings, that are called singular configurations in robotics, seem to be very useful. As we know, both human beings and robots can be modeled as multibody systems, and they have much in common. The features of singular configurations that will be mentioned later, might have a great ability to solve the above problems for the robots.

Robot kinematics describes the motion of the robot, such as the relation among displacement, velocity, acceleration and time, without considering the cause of the motion (force). Forward kinematics calculates the position and orientation of the end-effector in terms of the joint variables. In general, by denoting the end-effector position and orientation by $\boldsymbol{x} \in R^m$ and the set of joint angles as $\boldsymbol{q} \in R^n$ for a robot manipulator, the forward kinematics map is expressed as

$$\boldsymbol{x} = \boldsymbol{f}(\boldsymbol{q}). \tag{1.1}$$

The following equation will be obtained by differentiating the forward kinematics map

$$\dot{\boldsymbol{x}} = \boldsymbol{J}\dot{\boldsymbol{q}}, \tag{1.2}$$

where $\boldsymbol{J} = \partial \boldsymbol{x}/\partial \boldsymbol{q}$, and is called $(m \times n)$ Jacobian matrix. The Jacobian relates how movement of the elements of $\boldsymbol{q}$ causes movement of the elements of $\boldsymbol{x}$. In robot kinematics, the Jacobian

matrix is very important and arises in almost every aspect of robotic manipulation, such as in motion planning and in the derivation of equations of motion. Based on the Jacobian matrix, manipulability ellipsoid has been proposed to geometrically interpret the ability for the robot manipulator to change its end-effector position [35]. A round ellipsoid suggests that the robot can produce equal velocities in all directions. In robotics, inverse kinematics problem is very fundamental. There are many researches for solving the joint space solution to a required end-effector position and orientation [36–39].

According to the principle of virtual work, there exists a symmetric relation between the force/torque and velocity/angular velocity. In statics, the relationship between the force $\boldsymbol{F}$ applied at the end-effector and the joint torques $\boldsymbol{\tau}$ can be derived as

$$\boldsymbol{\tau} = \boldsymbol{J}^T \boldsymbol{F}. \tag{1.3}$$

For a robot manipulator, singular configuration is a configuration where the Jacobian matrix relating the end-effector velocity to the joint velocities drops rank [40]. The solution to the inverse kinematics problem is undefined in a singular configuration. At a kinematic singularity, the rank of the Jacobian matrix r is less than m, and some column vectors of the Jacobian matrix become linearly dependent. Thus, the end-effector loses one or more degrees of freedom, and can not move in the directions corresponding to the degenerated freedoms. In motion planning and precise control for the robot end-effector, it is widely common to avoid the singular configurations [41–43]. To understand the properties of singular configuration, many researchers focus on the analysis of kinematic singularities for parallel manipulators [44–52] and for serial ones [53–58]. The literature [45] has developed a general framework for the singularity analysis of non-redundant mechanisms. The singular configurations of redundant manipulators have been classified based on the possibility of reconfiguration into a nonsingular posture using self-motion in [55].

The robot dynamics describes how the robot moves in response to actuator forces. The derivation of equations of motion is central to the dynamics. There are many methods of generating dynamic equations or equations of motion of a mechanical system based on Lagrangian equation and Newton-Euler formulation. All the methods generate the same equations, but some approaches could reduce the computation complexity [59–63]. The kinematics and dynamics are highly coupled, that is, kinematic properties have a strong effect on the dynamics. The dynamic manipulability takes the robot dynamics into consideration in order to measure how easily the position and orientation of the end-effector can change in motion [64, 65]. It is derived from the Jacobian matrix and the inertia matrix of the robot. In a singular configuration, both the manipulability ellipsoid and dynamic manipulability ellipsoid become degenerate, and the acceleration along the degenerate direction cannot be caused in-

stantaneously by the joint torques. However, the variation of the dynamic manipulability near singular configurations has not been examined sufficiently. As the robot moves slightly from the singular configuration along the degenerate direction, the dynamic manipulability ellipsoid changes drastically, which will be shown in Appendix 2.A. The dynamic performance in terms of inertial or mass properties has also been characterized in [66, 67], and the one in terms of the end-effector acceleration has been described in [68]. In the dynamic model of a robot manipulator, joint velocities generally appear as nonlinear terms which include the Coriolis and centrifugal forces. However, these researches have not considered the velocity effects sufficiently, that can play an important role in the acceleration of the end-effector [69, 70]. The Coriolis and centrifugal forces become larger for dynamic motions with large joint velocities, and could be major causes for the acceleration of the end-effector. The analysis of the velocity effects near the singular configurations will become one of the emphases in this dissertation.

1.2 Motivation and Goal

Since the demerit of singular configurations in robot kinematics is so obvious, the role of singular configurations in robot dynamics has been neglected for a long time. Until recently, singular configurations have shown the usefulness for achieving dynamic motions of the robots [71–73]. Some static and dynamic features of singular configurations have been noticed in [16, 74, 75]. A heavy weight is lifted (or pulled) up in [16], while a heavy door is pulled in [74]. Through theoretical analysis and numerical simulations, the literature [16, 74] has shown that energy can be efficiently generated by the joint torques near the singular configurations, and the heavy object is strongly pulled simultaneously. However, the researches have not theoretically explained how to accelerate the object near singular configurations in pulling motions.

So far there has been little research on the dynamics of the robots near singular configurations, and it is still not understood sufficiently. Therefore, the singular configurations have not been widely utilized in robot motions. As mentioned earlier, human beings dexterously utilize the singular configurations in several motions such as jumping and pulling. When we make the robots perform such dynamic tasks like human beings, it becomes necessary to understand the dynamic features of robot near their singular configurations. This dissertation focuses on the relation between the robot motion and the singular configurations.

In this dissertation, the features of singular configurations will be summarized, and their dynamic advantages in the motions of robot manipulators and legged robots will be verified. Since the dynamics of the robots with more than two links is extremely complex, the model of a two-link robot manipulator will be considered for analysis. Two-link mechanisms are

Table 1.1: Classification of the robot motions in this dissertation and the ones in our previous studies

	In vertical plane	In horizontal plane
Fixed robot base	Lifting motion of a two-link manipulator (Sections 3.2, 3.3 and [16])	Pulling motion of a two-link manipulator ([74])
Unfixed robot base	Jumping and landing motions of two-link/four-link legged robots (Sections 4.2, 4.3 and 4.4)	Dragging motion of a two-link mobile manipulator (Section 3.4)

commonly used, and considered as a simplified model of our arms and legs. The analysis of the two-link manipulator could be important for a fundamental understanding of singular configurations and its future extension. The robot motions in this dissertation and the ones in our previous studies are classified in Table 1.1, according to whether the robot bases are fixed or unfixed, and whether the robots move in a vertical or horizontal plane. In the lifting motion of a two-link robot manipulator and dragging motion of a two-link mobile manipulator, a heavy object is pulled by the manipulator. Numerical optimization will be performed to clarify the usefulness of the singular configuration in the pulling motions. More precisely, the necessary joint torques in the robot motion are minimized, and the corresponding motion is analyzed to check whether the result is concerned with the features of singular configurations or not. In the jumping motion of two/four-link legged robots and landing motion of a four-link legged robot, a heavy body is pushed by the leg. The utilization of singular configurations in these motions will also be examined.

1.3 Outline

The main structure of this dissertation is shown in Fig. 1.1. The main theme is to study the relation between the features of singular configurations and their applications, namely, some illustrative robot motions.

Chapter 2 lists four features of singular configurations observed up to now. Section 2.2 derives the kinematic and dynamic equations of a multibody system, which is designed as a series of rigid links, as a general representation. Since this dissertation deals with several kinds of robots, the corresponding kinematics and dynamics can be easily calculated based on the obtained equations. Section 2.3 introduces the model of a two-link robot manipulator, by using the equations obtained in Section 2.2. A brief explanation about two of the features is given in Section 2.4. The other features have been noticed but not theoretically explained before. A simplified model of the two-link manipulator is considered, and the two features are

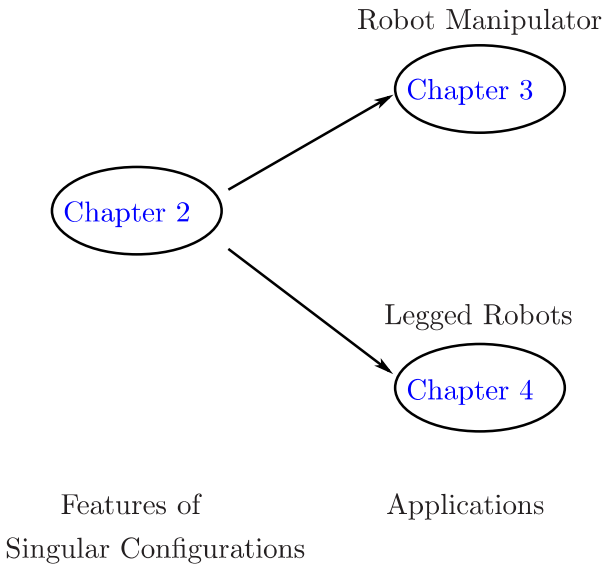

Figure 1.1: Main structure of this dissertation

verified through theoretical analysis in Section 2.5. The main contribution is that this dissertation provides a theoretical explanation about the dynamic features of singular configurations, which can be utilized in robot motion.

Chapter 3 deals with the motions of two-link robot manipulators such as a manipulator with fixed base and a mobile manipulator with unfixed base. Sections 3.2 and 3.3 present the lifting motions of a two-link robot manipulator, a lifting motion and a weight lifting motion, respectively. A heavy object attached to the end-effector is to be moved upward by the manipulator. In the lifting motion, the heavy object is lifted up a certain height from the lowest position, while the heavy object is lifted up to the highest position in the weight lifting motion. These motions are optimized for minimizing the necessary joint torques. The numerical simulation results show that the features of singular configurations are advantageous in generating large energy and causing large acceleration with bounded joint torques. Section 3.4 deals with the optimal motion of a mobile manipulator for dragging a heavy object with the end-effector. When the object is moved a certain distance, the torques that are consumed in the mobile manipulator during the motion are minimized by numerical optimization. In the optimized motion, the arm mounted on the mobile base passes through its singular configuration, and a large force to pull the object is generated simultaneously. A theoretical analysis is performed to explain the numerical results by using a simplified model of the mobile manipulator.

Chapter 4 deals with the motions of legged robots, including a two-link legged robot and a four-link legged one. Sections 4.2 and 4.3 obtain optimal jumping motions of a two-link legged robot and a four-link legged one. For the two-link robot, the robot motion in stance

phase is considered, and a fixed amount of translational energy is supplied to the robot from joint torques by the take-off time when the foot leaves the ground. For the four-link robot, the robot motion in aerial phase in addition to the one in stance phase is also considered, and the rotations of joints are stopped in the air by the time when the robot reaches the maximum height with the joints fully extended. For both the two-link robot and four-link one, the numerical optimization results show that the take-off posture that is close to a singular configuration has the advantage in supplying a large force (or acceleration) efficiently in stance phase. Furthermore, the numerical optimization results of the four-link robot with different take-off postures show that the take-off posture close to a singular configuration is also useful for reducing the rotational energy that has to be eliminated in aerial phase. Even though the model of the four-link robot is more complex, the features of singular configurations can be noticed in the motions of both robots. Section 4.4 deals with optimal landing motions of a four-link legged robot that minimizes the impact force at the contact point and the necessary joint torques during the motion. The cost function for optimization is given as the weighted sum of the impact force and the joint torques. The configuration of the robot that is close to a singular configuration is advantageous in minimizing the joint torques for a heavy body, while the configuration where the leg is bent is advantageous in reducing the impact force. This is shown by numerical optimization results with different weights for the cost function and a theoretical analysis of a simplified model for the legged robot.

Finally, this dissertation is summarized in Chapter 5.

Chapter 2

Features of Singular Configurations

2.1 Introduction

As mentioned in Chapter 1, the disadvantage of singular configurations has been observed based on the investigation of robot kinematics. Due to the disadvantage, singular configurations fell from grace with the scientists.

There exist few studies on the advantage of singular configurations, which is concerned with the robot dynamics. Since the dynamics is much more complex than the kinematics, a detailed investigation of robot dynamics near singular configurations has been neglected until recently. This research gains enlightenment from the analysis of the dynamics related to a two-link manipulator in the literature [16, 74].

Firstly, the derivation of the kinematics and dynamics of a multibody system will be described in detail. Based on the obtained equations, the kinematic and dynamic equations with respect to all the robots considered in this dissertation will be easily calculated. Then, four features of singular configurations related to a two-link robot manipulator will be introduced, and two of them are demonstrated by theoretical analysis. These features will deepen our understanding of singular configurations.

2.2 Kinematics and Dynamics of a Multibody System

In robotics, the general form of equations of motion is expressed as

$$\boldsymbol{M}(\boldsymbol{q})\ddot{\boldsymbol{q}} + \boldsymbol{h}(\boldsymbol{q},\dot{\boldsymbol{q}}) + \boldsymbol{\tau}_g(\boldsymbol{q}) = \boldsymbol{\tau} + \boldsymbol{J}^T\boldsymbol{F}, \tag{2.1}$$

where $\boldsymbol{M}(\boldsymbol{q})$ is the inertia matrix, $\boldsymbol{h}(\boldsymbol{q},\dot{\boldsymbol{q}})$ is the vector with respect to the Coriolis and centrifugal effects, and $\boldsymbol{\tau}_g$ is the gravitational term. The vector $\boldsymbol{F}$ denotes the force at the end-effector

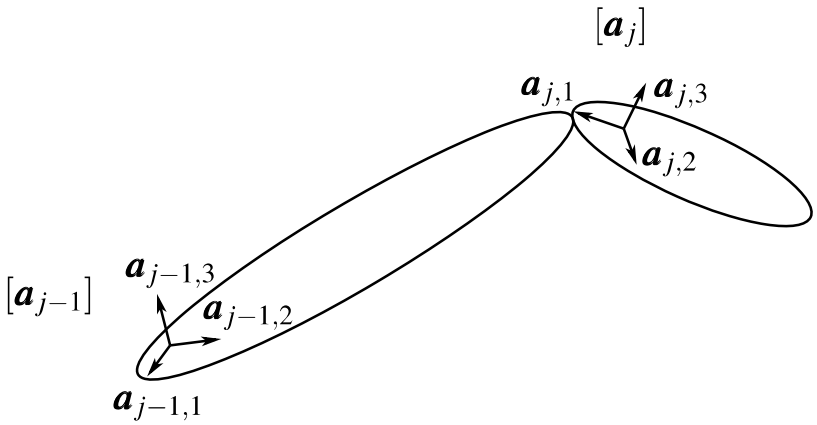

Figure 2.1: Model of link $j-1$ and j of a n-link multibody system

of the manipulator, and $\boldsymbol{J}$ is the corresponding Jacobian matrix. In general, a robot can be modeled as a multibody system.

Since this dissertation deals with several kinds of serial robots, a general representation of kinematic and dynamic equations for these robots will be required to efficiently reduce the computational complexity. The kinematics and dynamics of a multibody system which is designed as a series of rigid links will be introduced in this section.

2.2.1 Kinematics

Firstly, two orthogonal sets of unit vectors, $\{\boldsymbol{a}_{j-1}\} = \{\boldsymbol{a}_{j-1,1}, \boldsymbol{a}_{j-1,2}, \boldsymbol{a}_{j-1,3}\}$ and $\{\boldsymbol{a}_j\} = \{\boldsymbol{a}_{j,1}, \boldsymbol{a}_{j,2}, \boldsymbol{a}_{j,3}\}$, are introduced. As shown in Fig. 2.1, the vectors of $\{\boldsymbol{a}_{j-1}\}$ and $\{\boldsymbol{a}_j\}$ are fixed in the link $j-1$ and link j of a n-link multibody system respectively, where $j = 1, \ldots, n$. The notations $[\boldsymbol{a}_{j-1}]$ and $[\boldsymbol{a}_j]$ denote the coordinate frames for the link $j-1$ and link j, and are defined as $[\boldsymbol{a}_{j-1}] = [\boldsymbol{a}_{j-1,1}, \boldsymbol{a}_{j-1,2}, \boldsymbol{a}_{j-1,3}]^T$ and $[\boldsymbol{a}_j] = [\boldsymbol{a}_{j,1}, \boldsymbol{a}_{j,2}, \boldsymbol{a}_{j,3}]^T$. The following vectors are also defined:

$\boldsymbol{\omega}_{j,i} = [\boldsymbol{a}_j]^{T(j)}\boldsymbol{\omega}_{j,i}$: Angular velocity vector of $[\boldsymbol{a}_j]$ with respect to $[\boldsymbol{a}_i]$,

$\boldsymbol{\rho}_j = [\boldsymbol{a}_j]^{T(j)}\boldsymbol{\rho}_j$: Position vector from an arbitrary point in the link to the mass center of link j,

$\boldsymbol{R}_j = [\boldsymbol{a}_j]^{T(j)}\boldsymbol{R}_j$: Position vector from the origin of $[\boldsymbol{a}_j]$ to the mass center of link j,

$\boldsymbol{r}_j = [\boldsymbol{a}_j]^{T(j)}\boldsymbol{r}_j$: Position vector from the origin of $[\boldsymbol{a}_j]$ to the origin of $[\boldsymbol{a}_{j+1}]$,

$\boldsymbol{\omega}_j = [\boldsymbol{a}_j]^{T(j)}\boldsymbol{\omega}_j \left(= \sum_{j'=1}^{j} \boldsymbol{\omega}_{j',j'-1} \right)$: Angular velocity vector of $[\boldsymbol{a}_j]$ with respect to $[\boldsymbol{a}_0]$,

$\boldsymbol{A}_{j,i}$: Transformation matrix from $[\boldsymbol{a}_i]$ to $[\boldsymbol{a}_j]$.

The vector $\boldsymbol{x}$ in Fig. 2.1 can be expressed in two different frames as $\boldsymbol{x} = [\boldsymbol{a}_j]^{T(j)}\boldsymbol{x} =$

$[\boldsymbol{a}_{j-1}]^{T\,(j-1)}\boldsymbol{x}$. The local coordinate representations ${}^{(j-1)}\boldsymbol{x}$ and ${}^{(j)}\boldsymbol{x}$ of $\boldsymbol{x}$ in $[\boldsymbol{a}_{j-1}]$ and $[\boldsymbol{a}_j]$ satisfy ${}^{(j)}\boldsymbol{x} = [\boldsymbol{a}_j][\boldsymbol{a}_{j-1}]^{T\,(j-1)}\boldsymbol{x} = \boldsymbol{A}_{j,j-1}{}^{(j-1)}\boldsymbol{x}$. The transformation matrix $\boldsymbol{A}_{j,j-1}$ is an orthogonal matrix, and satisfies

$$\boldsymbol{A}_{j,j-1}\boldsymbol{A}_{j,j-1}^{T} = I. \tag{2.2}$$

By differentiating the above equation, the following relation will be obtained:

$$\dot{\boldsymbol{A}}_{j,j-1} = -{}^{(j)}\boldsymbol{\omega}_{j,j-1} \times \boldsymbol{A}_{j,j-1}. \tag{2.3}$$

A cross product of vector $\boldsymbol{x}$ is defined as $\widetilde{\boldsymbol{x}}$:

$$\boldsymbol{x} = \begin{bmatrix} x_1 \\ x_2 \\ x_3 \end{bmatrix}, \tag{2.4}$$

$$\widetilde{\boldsymbol{x}} = -\boldsymbol{x}\times = \begin{bmatrix} 0 & x_3 & -x_2 \\ -x_3 & 0 & x_1 \\ x_2 & -x_1 & 0 \end{bmatrix}. \tag{2.5}$$

Thus, (2.3) can be rewritten as

$$\dot{\boldsymbol{A}}_{j,j-1} = {}^{(j)}\tilde{\boldsymbol{\omega}}_{j,j-1}\boldsymbol{A}_{j,j-1}, \tag{2.6}$$

where ${}^{(j)}\tilde{\boldsymbol{\omega}}_{j,j-1} = \dot{\boldsymbol{A}}_{j,j-1}\boldsymbol{A}_{j,j-1}^{T}$. The following equations are valid with respect to cross product :

$$\dot{\boldsymbol{r}} = \boldsymbol{\omega} \times \boldsymbol{r} = -\boldsymbol{r} \times \boldsymbol{\omega} = \tilde{\boldsymbol{r}}\boldsymbol{\omega}, \tag{2.7}$$

$$\boldsymbol{R}(\boldsymbol{b} \times \boldsymbol{c}) = (\boldsymbol{R}\boldsymbol{b}) \times (\boldsymbol{R}\boldsymbol{c}), \tag{2.8}$$

$$\boldsymbol{R}(\boldsymbol{w}\times)\boldsymbol{R}^{T} = (\boldsymbol{R}\boldsymbol{w})\times, \tag{2.9}$$

$$\frac{d}{dt}[\boldsymbol{a}_j]^{T} = \boldsymbol{\omega}_j \times [\boldsymbol{a}_j]^{T}. \tag{2.10}$$

There are many representations to parameterize $\boldsymbol{A}_{j,j-1}$ such as Euler angles and quaternions. For instance, the 1-2-3 Euler angles are defined as $\boldsymbol{\theta}_{j,j-1} = [\theta_1\ \theta_2\ \theta_3]^{T}$, and the trans-

formation matrix $\boldsymbol{A}_{j,j-1}$ becomes

$$\boldsymbol{A}_{j,j-1} = \boldsymbol{R}_3(\theta_3)\boldsymbol{R}_2(\theta_2)\boldsymbol{R}_1(\theta_1) \tag{2.11}$$

$$= \begin{pmatrix} c\theta_2 c\theta_3 & s\theta_1 s\theta_2 c\theta_3 + c\theta_1 s\theta_3 & -c\theta_1 s\theta_2 c\theta_3 + s\theta_1 s\theta_3 \\ -c\theta_2 s\theta_3 & -s\theta_1 s\theta_2 s\theta_3 + c\theta_1 c\theta_3 & c\theta_1 s\theta_2 s\theta_3 + s\theta_1 s\theta_3 \\ s\theta_2 & -s\theta_1 c\theta_2 & c\theta_1 c\theta_2 \end{pmatrix}, \tag{2.12}$$

where

$$\boldsymbol{R}_1(\theta_1) = \begin{pmatrix} 1 & 0 & 0 \\ 0 & c\theta_1 & s\theta_1 \\ 0 & -s\theta_1 & c\theta_1 \end{pmatrix}, \boldsymbol{R}_2(\theta_2) = \begin{pmatrix} c\theta_2 & 0 & -s\theta_2 \\ 0 & 1 & 0 \\ s\theta_2 & 0 & c\theta_2 \end{pmatrix},$$

$$\boldsymbol{R}_3(\theta_3) = \begin{pmatrix} c\theta_3 & s\theta_3 & 0 \\ -s\theta_3 & c\theta_3 & 0 \\ 0 & 0 & 1 \end{pmatrix}, c\theta = \cos\theta \text{ and } s\theta = \sin\theta.$$

The relative joint velocity ${}^{(j)}\boldsymbol{\omega}_{j,j-1}$ can be expressed by the Euler angle rates as

$${}^{(j)}\boldsymbol{\omega}_{j,j-1} = \boldsymbol{s}(\boldsymbol{\theta})\dot{\boldsymbol{\theta}}, \boldsymbol{s}(\boldsymbol{\theta}) = \begin{pmatrix} c\theta_2 c\theta_3 & s\theta_3 & 0 \\ -c\theta_2 s\theta_3 & c\theta_3 & 0 \\ s\theta_2 & 0 & 1 \end{pmatrix}. \tag{2.13}$$

The system is composed of n links as shown in Fig. 2.2. The origin of $[\boldsymbol{a}_j]$ is located on link i, and $[\boldsymbol{a}_0]$ is fixed to the inertia space. The following vector will be used as generalized coordinates

$$\boldsymbol{x}^T = [{}^{(0)}\boldsymbol{r}_0^T, (\boldsymbol{\theta}_{1,0})^T, (\boldsymbol{\theta}_{2,1})^T \ldots (\boldsymbol{\theta}_{n,n-1})^T]. \tag{2.14}$$

The velocity variables are introduced as follows:

$$\boldsymbol{Z}^T = [{}^{(0)}\dot{\boldsymbol{r}}_0^T, \left({}^{(1)}\boldsymbol{\omega}_{1,0}\right)^T, \left({}^{(2)}\boldsymbol{\omega}_{2,1}\right)^T \ldots \left({}^{(n)}\boldsymbol{\omega}_{n,n-1}\right)^T]. \tag{2.15}$$

The two vectors satisfy the equation below:

$$\dot{\boldsymbol{x}} = \boldsymbol{S}^{-1}\boldsymbol{Z}, \tag{2.16}$$

where $\boldsymbol{S}^{-1} = diag\left(\boldsymbol{I}, \boldsymbol{s}^{-1}(\boldsymbol{\theta}_{1,0}), \boldsymbol{s}^{-1}(\boldsymbol{\theta}_{2,1}), \ldots, \boldsymbol{s}^{-1}(\boldsymbol{\theta}_{n,n-1})\right)$.

The equations of motion based on Newton-Euler formulation will be derived. Firstly, the position vector $\boldsymbol{x}_j$ from the origin of $[\boldsymbol{a}_0]$ to an arbitrary point in link j and velocity vector of

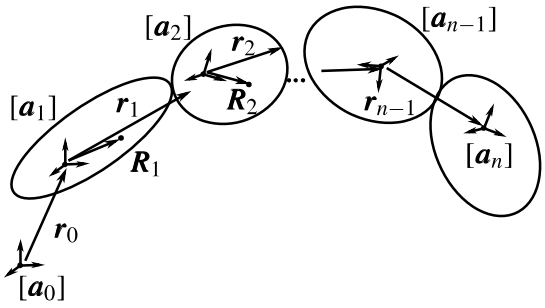

Figure 2.2: Model of n-link serial multibody system

that point $\boldsymbol{u}_j$ can be expressed by

$$\boldsymbol{x}_j = [\boldsymbol{a}_0]^{T\,(0)}\boldsymbol{r}_0 + \sum_{j'=1}^{j-1}[\boldsymbol{a}_{j'}]^{T\,(j')}\boldsymbol{r}_{j'} + [\boldsymbol{a}_j]^T({}^{(j)}\boldsymbol{R}_j + {}^{(j)}\boldsymbol{\rho}_j), \tag{2.17}$$

$$\boldsymbol{u}_j = [\boldsymbol{a}_0]^{T\,(0)}\dot{\boldsymbol{r}}_0 + \sum_{j'=1}^{j-1}[\boldsymbol{a}_{j'}]^T({}^{(j')}\tilde{\boldsymbol{r}}_{j'}{}^{(j')}\boldsymbol{\omega}_{j',0}) + [\boldsymbol{a}_j]^T({}^{(j)}\tilde{\boldsymbol{R}}_j + {}^{(j)}\tilde{\boldsymbol{\rho}}_j){}^{(j)}\boldsymbol{\omega}_{j,0}. \tag{2.18}$$

It should be noted that for the point in link 1, $\boldsymbol{x}_1 = [\boldsymbol{a}_0]^{T\,(0)}\boldsymbol{r}_0 + [\boldsymbol{a}_1]^T\left({}^{(1)}\boldsymbol{R}_1 + {}^{(1)}\boldsymbol{\rho}_1\right)$ and $\boldsymbol{u}_1 = [\boldsymbol{a}_0]^{T\,(0)}\dot{\boldsymbol{r}}_0 + [\boldsymbol{a}_1]^T\left({}^{(1)}\tilde{\boldsymbol{R}}_1 + {}^{(1)}\tilde{\boldsymbol{\rho}}_1\right){}^{(1)}\boldsymbol{\omega}_{1,0}$. The component of $\boldsymbol{u}_j$ in the frame $[\boldsymbol{a}_j]$ becomes

$${}^{(j)}\boldsymbol{u}_j = \boldsymbol{A}_{j,0}{}^{(0)}\dot{\boldsymbol{r}}_0 + \sum_{j'=1}^{j-1}\boldsymbol{A}_{j,j'}({}^{(j')}\tilde{\boldsymbol{r}}_{j'}{}^{(j')}\boldsymbol{\omega}_{j',0}) + ({}^{(j)}\tilde{\boldsymbol{R}}_j + {}^{(j)}\tilde{\boldsymbol{\rho}}_j){}^{(j)}\boldsymbol{\omega}_{j,0}. \tag{2.19}$$

This equation can also be rewritten in matrix form as

$${}^{(j)}\boldsymbol{u}_j = ({}^{(j)}\boldsymbol{L}_j + {}^{(j)}\boldsymbol{\ell}_j + {}^{(j)}\boldsymbol{\rho}_j)\boldsymbol{H}\boldsymbol{Z}, \tag{2.20}$$

where

$$\boldsymbol{H} = \begin{pmatrix} \boldsymbol{I} & \boldsymbol{0} & \boldsymbol{0} & \dots & \boldsymbol{0} \\ \boldsymbol{A}_{1,0} & \boldsymbol{I} & \boldsymbol{0} & & \boldsymbol{0} \\ \boldsymbol{A}_{2,0} & \boldsymbol{A}_{2,1} & \boldsymbol{I} & & \boldsymbol{0} \\ \vdots & & & \ddots & \vdots \\ \boldsymbol{A}_{n,0} & \boldsymbol{A}_{n,1} & \boldsymbol{A}_{n,2} & \dots & \boldsymbol{I} \end{pmatrix} \in R^{3(n+1)\times 3(n+1)},$$

$${}^{(j)}\boldsymbol{L}_j = \left[\begin{array}{cccc|c} \boldsymbol{A}_{j,0} & \boldsymbol{A}_{j,1}{}^{(1)}\tilde{\boldsymbol{r}}_1 & \dots & \boldsymbol{A}_{j,j-1}{}^{(j-1)}\tilde{\boldsymbol{r}}_{j-1} & \overbrace{\boldsymbol{0} \quad \dots \quad \boldsymbol{0}}^{n+1-j} \end{array}\right] \in R^{3\times 3(n+1)},$$

$$^{(j)}\boldsymbol{\ell}_j = \left[\overbrace{\mathbf{0} \quad \dots \quad \mathbf{0}}^{j} \quad {}^{(j)}\tilde{\boldsymbol{R}}_j \quad \overbrace{\mathbf{0} \quad \dots \quad \mathbf{0}}^{n-j} \right] \in R^{3\times 3(n+1)}, \text{ and}$$

$$^{(j)}\boldsymbol{\rho}_j = \left[\overbrace{\mathbf{0} \quad \dots \quad \mathbf{0}}^{j} \quad {}^{(j)}\tilde{\boldsymbol{\rho}}_j \quad \overbrace{\mathbf{0} \quad \dots \quad \mathbf{0}}^{n-j} \right] \in R^{3\times 3(n+1)}.$$

2.2.2 Dynamics

Equations of motion with respect to translational movement

Let dm_j be arbitrary small mass in link j, $\boldsymbol{f}_j$ be distributed force at the mass and $\boldsymbol{x}_j$ be the displacement of the mass. According to newton's second law of motion, the equations of motion for the small mass are expressed as

$$\ddot{\boldsymbol{x}}_j dm_j = \frac{d}{dt}\dot{\boldsymbol{x}}_j dm_j = \boldsymbol{f}_j dm_j. \tag{2.21}$$

For the whole system, the equations of motion are obtained as

$$\frac{d}{dt}\sum_{j=1}^{n} < \dot{\boldsymbol{x}}_j >_j = \sum_{j=1}^{n} < \boldsymbol{f}_j >_j \tag{2.22}$$

$$\dot{\hat{\boldsymbol{L}}}_0 = \boldsymbol{N}_0, \tag{2.23}$$

where the equations are denoted in the inertia frame $[\boldsymbol{a}_0]$,

$< * >_j = \int * dm_j$,

$\hat{\boldsymbol{L}}_0 = \sum_{j=1}^{n} < \dot{\boldsymbol{x}}_j >_j$: Total translational momentum vector,

$\boldsymbol{N}_0 = \sum_{j=1}^{n} < \boldsymbol{f}_j >_j$: Total force vector applied at the whole system.

Equations of motion with respect to rotational movement

A position vector from the origin of $[\boldsymbol{a}_0]$ to joint i is denoted by $\boldsymbol{r}_{0i} = \sum_{j=0}^{i-1} \boldsymbol{r}_j$. By multiplying (2.21) by $(\boldsymbol{x}_j - \boldsymbol{r}_{0i})\times$, it is obtained that

$$(\boldsymbol{x}_j - \boldsymbol{r}_{0i}) \times \ddot{\boldsymbol{x}}_j dm_j = (\boldsymbol{x}_j - \boldsymbol{r}_{0i}) \times \boldsymbol{f}_j dm_j$$

$$\left(\frac{d}{dt}\left((\boldsymbol{x}_j - \boldsymbol{r}_{0i}) \times \dot{\boldsymbol{x}}_j \right) + \dot{\boldsymbol{r}}_{0i} \times \dot{\boldsymbol{x}}_j \right) dm_j = (\boldsymbol{x}_j - \boldsymbol{r}_{0i}) \times \boldsymbol{f}_j dm_j. \tag{2.24}$$

By considering the links from joint i to the end, the above equations can be combined as

$$\frac{d}{dt}\left(\sum_{j=i}^{n} < (\boldsymbol{x}_j - \boldsymbol{r}_{0i}) \times \dot{\boldsymbol{x}}_j >_j\right) + \dot{\boldsymbol{r}}_{0i} \times \sum_{j=i}^{n} < \dot{\boldsymbol{x}}_j >_j = \sum_{j=i}^{n} < (\boldsymbol{x}_j - \boldsymbol{r}_{0i}) \times \boldsymbol{f}_j >_j \tag{2.25}$$

$$\dot{\hat{\boldsymbol{L}}}_i + \tilde{\boldsymbol{\upsilon}}_i^T \hat{\boldsymbol{P}}_i = \boldsymbol{N}_i, (i = 1, \ldots, n), \tag{2.26}$$

where the equations are denoted in the inertia frame $[\boldsymbol{a}_0]$,

$\hat{\boldsymbol{L}}_i = \sum_{j=i}^{n} < (\boldsymbol{x}_j - \boldsymbol{r}_{0i}) \times \dot{\boldsymbol{x}}_j >_j$: Angular momentum vector with respect to the rotations of the links from joint i to the end $(i = 1, ..., n)$,

$\boldsymbol{\upsilon}_i = \dot{\boldsymbol{r}}_{0i}$: Translational velocity vector of joint i in the frame $[\boldsymbol{a}_0]$,

$\hat{\boldsymbol{P}}_i$: Total translational momentum vector of the links from joint i to the end,

$\boldsymbol{N}_i$: Joint torque vector with respect to the forces at the links from joint n to the end .

The obtained equations of motion (2.23) and (2.26) are denoted in the inertia frame $[\boldsymbol{a}_0]$. Next, the expression of the equations of motion related to link i in the local frame $[\boldsymbol{a}_i]$ will be given. Firstly, the generalized momenta are expressed as

$$\hat{\boldsymbol{L}}_i = [\boldsymbol{a}_i]^{T\,(i)}\hat{\boldsymbol{L}}_{i,i-1}. \tag{2.27}$$

By differentiating the above equation, it is obtained that

$$\dot{\hat{\boldsymbol{L}}}_i = \frac{d}{dt}\left([\boldsymbol{a}_i]^{T\,(i)}\hat{\boldsymbol{L}}_{i,i-1}\right) = [\boldsymbol{a}_i]^T \left({}^{(i)}\dot{\hat{\boldsymbol{L}}}_{i,i-1} + \left({}^{(i)}\tilde{\boldsymbol{\omega}}_{i,-1}\right)^T {}^{(i)}\hat{\boldsymbol{L}}_{i,i-1}\right). \tag{2.28}$$

Since $\boldsymbol{\upsilon}_i = [\boldsymbol{a}_i]^{T\,(i)}\boldsymbol{\upsilon}_i$, $\hat{\boldsymbol{P}}_i = [\boldsymbol{a}_i]^{T\,(i)}\hat{\boldsymbol{P}}_i$ and $\boldsymbol{N}_i = [\boldsymbol{a}_i]^{T\,(i)}\boldsymbol{N}_i$, the equations of motion in the local frame $[\boldsymbol{a}_i]$ are defined as

$${}^{(i)}\dot{\hat{\boldsymbol{L}}}_{i,i-1} + {}^{(i)}\tilde{\boldsymbol{\omega}}_{i,i-1}{}^{(i)}\hat{\boldsymbol{L}}_{i,i-1} + \left({}^{(i)}\tilde{\boldsymbol{\upsilon}}_i\right)^T {}^{(i)}\hat{\boldsymbol{P}}_i = {}^{(i)}\boldsymbol{N}_i. \tag{2.29}$$

By expressing the equations in matrix form, the equations of motion become

$$\dot{\hat{\boldsymbol{L}}} + \boldsymbol{\Omega}\hat{\boldsymbol{L}} + \boldsymbol{V}\hat{\boldsymbol{P}} = \boldsymbol{N}, \tag{2.30}$$

where

$$\boldsymbol{\Omega} = diag\left(\boldsymbol{0}, \left({}^{(1)}\tilde{\boldsymbol{\omega}}_{1,0}\right)^T, \left({}^{(2)}\tilde{\boldsymbol{\omega}}_{2,0}\right)^T, \ldots, \left({}^{(n)}\tilde{\boldsymbol{\omega}}_{n,0}\right)^T\right),$$

$$\boldsymbol{V} = diag\left(\boldsymbol{0}, \left({}^{(1)}\tilde{\boldsymbol{\upsilon}}_1\right)^T, \left({}^{(2)}\tilde{\boldsymbol{\upsilon}}_2\right)^T, \ldots, \left({}^{(n)}\tilde{\boldsymbol{\upsilon}}_n\right)^T\right),$$

$$\hat{\boldsymbol{L}} = \boldsymbol{K}\boldsymbol{Z},$$

$$\boldsymbol{K} = \boldsymbol{H}^T \left(\hat{\boldsymbol{L}}^T \boldsymbol{M} \hat{\boldsymbol{L}} + \boldsymbol{J} \right) \boldsymbol{H},$$

$$\hat{\boldsymbol{L}} = \boldsymbol{L} + \boldsymbol{\ell},$$

$$\boldsymbol{M} = \begin{bmatrix} \boldsymbol{0} & & & \\ & m_1 \boldsymbol{I} & & \boldsymbol{0} \\ & & \ddots & \\ & \boldsymbol{0} & & \ddots \\ & & & & m_n \boldsymbol{I} \end{bmatrix} \in R^{3(n+1)\times 3(n+1)},$$

$$\boldsymbol{J} = \begin{bmatrix} \boldsymbol{0} & & & \\ & {}^{(1)}\boldsymbol{J}_1 & & \boldsymbol{0} \\ & & \ddots & \\ & \boldsymbol{0} & & \ddots \\ & & & & {}^{(n)}\boldsymbol{J}_n \end{bmatrix} \in R^{3(n+1)\times 3(n+1)},$$

$$\boldsymbol{\ell} = \begin{bmatrix} \boldsymbol{0} & & & \\ & {}^{(1)}\tilde{\boldsymbol{R}}_1 & & \boldsymbol{0} \\ & & \ddots & \\ & \boldsymbol{0} & & \ddots \\ & & & & {}^{(n)}\tilde{\boldsymbol{R}}_n \end{bmatrix} \in R^{3(n+1)\times 3(n+1)},$$

$$\mathscr{L} = \begin{bmatrix} \boldsymbol{0} & & & & \\ \boldsymbol{A}_{1,0} & \boldsymbol{0} & & & \\ \boldsymbol{A}_{2,0} & \boldsymbol{A}_{2,1}{}^{(1)}\tilde{r}_1 & \boldsymbol{0} & \boldsymbol{0} & \\ \vdots & & & \ddots & \\ \boldsymbol{A}_{n,0} & \boldsymbol{A}_{n,1}{}^{(1)}\tilde{r}_1 & \dots & \boldsymbol{A}_{n,n-1}{}^{(n-1)}\tilde{\boldsymbol{r}}_{n-1} & \boldsymbol{0} \end{bmatrix} \in R^{3(n+1)\times 3(n+1)},$$

$$\boldsymbol{v} = \mathscr{L}\boldsymbol{H}\boldsymbol{Z} = \left[0, \left({}^{(1)}\boldsymbol{v}_1 \right)^T, \left({}^{(2)}\boldsymbol{v}_2 \right)^T, \dots, \left({}^{(n)}\boldsymbol{v}_n \right)^T \right]^T,$$

$$\hat{\boldsymbol{P}} = \boldsymbol{H}^T \boldsymbol{M} \hat{\boldsymbol{L}} \boldsymbol{H} \boldsymbol{Z} = \left[\boldsymbol{0}, \left({}^{(1)}\hat{\boldsymbol{P}}_1 \right)^T, \left({}^{(2)}\hat{\boldsymbol{P}}_2 \right)^T, \dots, \left({}^{(n)}\hat{\boldsymbol{P}}_n \right)^T \right]^T.$$

The notation ${}^{(j)}\boldsymbol{J}_j$ denotes the moment of inertia with respect to the mass center of link j, and equals to $< \left({}^{(j)}\boldsymbol{\rho}_j\right)^T {}^{(j)}\boldsymbol{\rho}_j >_j$.

The components of generalized forces $\boldsymbol{N}$ are shown as follows

$$\boldsymbol{N} = \boldsymbol{H}^T \left(\hat{\boldsymbol{L}}^T \boldsymbol{F}_1 + \boldsymbol{F}_2\right) + \boldsymbol{F}_3, \tag{2.31}$$

where

$\boldsymbol{F}_1 = \left[0, < {}^{(1)}\boldsymbol{f}_1 >_1^T, < {}^{(2)}\boldsymbol{f}_2^{(1)} >_2^T, \ldots, < {}^{(n)}\boldsymbol{f}_n >_n^T\right]^T$,

$\boldsymbol{F}_2 = \left[\ 0 \quad , < {}^{(1)}\tilde{\boldsymbol{\rho}}_1^T {}^{(1)}\boldsymbol{f}_1 >_1^T \quad , < {}^{(2)}\tilde{\boldsymbol{\rho}}_2^T {}^{(2)}\boldsymbol{f}_2 >_2^T \quad , \ldots \quad , < {}^{(n)}\tilde{\boldsymbol{\rho}}_n^T {}^{(n)}\boldsymbol{f}_n >_n^T \ \right]^T$,

$\boldsymbol{F}_3$ is the vector of external forces.

The obtained equations of motion can be rewritten as

$$\boldsymbol{K}\dot{\boldsymbol{Z}} + \dot{\boldsymbol{K}}\boldsymbol{Z} + \boldsymbol{\Omega}\hat{\boldsymbol{L}} + \boldsymbol{V}\hat{\boldsymbol{P}} = \boldsymbol{H}^T \left(\hat{\boldsymbol{L}}^T \boldsymbol{F}_1 + \boldsymbol{F}_2\right) + \boldsymbol{F}_3. \tag{2.32}$$

The matrix $\boldsymbol{K}$ and the vector $\dot{\boldsymbol{K}}\boldsymbol{Z} + \boldsymbol{\Omega}\hat{\boldsymbol{L}} + \boldsymbol{V}\hat{\boldsymbol{P}}$ correspond to $\boldsymbol{M}$ and $\boldsymbol{h}$ in (2.1) and the terms $\boldsymbol{F}_3$ and $\boldsymbol{H}^T \left(\hat{\boldsymbol{L}}^T \boldsymbol{F}_1 + \boldsymbol{F}_2\right)$ correspond to $\boldsymbol{\tau}$ and $\boldsymbol{J}^T\boldsymbol{F} - \boldsymbol{\tau}_g(\boldsymbol{q})$ in (2.1).

For a robot, the origin of the local frame $[\boldsymbol{a}_1]$ is always set to be located on the robot base. When the robot base is fixed, $[\boldsymbol{a}_1]$ is stationary and the degrees of freedom of the robot decrease. The vectors $\boldsymbol{x}$ and $\boldsymbol{Z}$ are reduced to $\boldsymbol{x}^T = [(\boldsymbol{\theta}_{2,1})^T \ \ldots \ (\boldsymbol{\theta}_{n,n-1})^T]$ and $\boldsymbol{Z}^T = [\left({}^{(2)}\boldsymbol{\omega}_{2,1}\right)^T \ \ldots \ \left({}^{(n)}\boldsymbol{\omega}_{n,n-1}\right)^T]$. If there exist more structural constraints on the robot, the number of degrees of freedom is reduced to a smaller one.

With the obtained equations of motion, the ones for all the robots in the remaining chapters can be easily calculated, such as the two-link manipulator in Section 2.3 and the four-link legged robot in Section 4.3. The equations of motion for the mobile manipulator in Section 3.4 can also be obtained in a similar way.

2.3 Model of a Two-link Manipulator with Heavy Object

A two-link manipulator with a heavy object attached to the end-effector is considered, and the heavy object is regarded as a mass point, as shown in Fig. 2.3. The base is fixed at the origin of x-y coordinate system. The first and second links are called link 1 and link 2 respectively. The joint between y-axis and link 1 is called joint 1, and the joint between link 1 and link 2 is called joint 2. The joint angle and input torque at joint i are expressed as θ_i and τ_i respectively. The mass, length and moment of inertia of link i are denoted as m_i, l_i and I_i $(i = 1, 2)$. The length between joint i and the mass center of link i is expressed as l_{gi}. The mass of the object is called m_w. The generalized coordinates and generalized forces are chosen as $\boldsymbol{q} = [\theta_1, \theta_2]^T$

and $\boldsymbol{\tau} = [\tau_1, \tau_2]^T$. The position of the end-effector is denoted as $\boldsymbol{p}_e = [x_e, y_e]^T$.

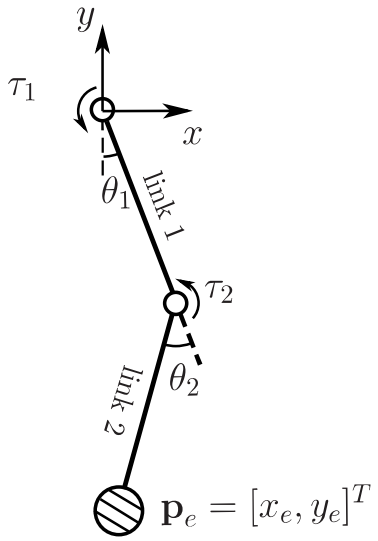

Figure 2.3: Model of two-link manipulator

The end-effector velocity $\dot{\boldsymbol{p}}_e$ can be expressed by using the generalized coordinates $\boldsymbol{q}$:

$$\dot{\boldsymbol{p}}_e = \boldsymbol{J}(\boldsymbol{q})\dot{\boldsymbol{q}}, \tag{2.33}$$

where the Jacobian matrix is

$$\boldsymbol{J} = \begin{bmatrix} l_1\cos\theta_1 + l_2\cos(\theta_1+\theta_2) & l_2\cos(\theta_1+\theta_2) \\ l_1\sin\theta_1 + l_2\sin(\theta_1+\theta_2) & l_2\sin(\theta_1+\theta_2) \end{bmatrix}. \tag{2.34}$$

The equations of motion for the manipulator can be represented as:

$$\boldsymbol{M}(\boldsymbol{q})\ddot{\boldsymbol{q}} + \boldsymbol{h}(\boldsymbol{q},\dot{\boldsymbol{q}}) + \boldsymbol{\tau}_g(\boldsymbol{q}) = \boldsymbol{\tau}. \tag{2.35}$$

The inertia matrix $\boldsymbol{M}$ can be written as

$$\boldsymbol{M} = \boldsymbol{M}_a + m_w \boldsymbol{J}^T \boldsymbol{J}. \tag{2.36}$$

The inertia matrix of the manipulator $\boldsymbol{M}_a$ is

$$\boldsymbol{M}_a = \begin{bmatrix} M_1 & M_2 \\ M_2 & M_3 \end{bmatrix}, \tag{2.37}$$

where $M_1 = m_1 l_{g1}^2 + m_2(l_1^2 + l_{g2}^2 + 2l_1 l_{g2}\cos\theta_2) + I_1 + I_2$, $M_2 = m_2(l_{g2}^2 + l_1 l_{g2}\cos\theta_2) + I_2$ and $M_3 = m_2 l_{g2}^2 + I_2$. The kinetic energy E is denoted by using $\boldsymbol{M}$ as

$$E = \frac{1}{2}\dot{\boldsymbol{q}}^T \boldsymbol{M}(\boldsymbol{q})\dot{\boldsymbol{q}}, \tag{2.38}$$

and $\boldsymbol{h}$ can be expressed as $\boldsymbol{h} = \dot{\boldsymbol{M}}\dot{\boldsymbol{q}} - (\partial E/\partial \boldsymbol{q})^T$. The gravitational field points toward the y-axis negative direction, and the gravity term $\boldsymbol{\tau}_g$ is calculated as

$$\begin{aligned}\boldsymbol{\tau}_g =&[(m_1 l_{g1} + m_2 l_1 + m_w l_1)g\sin\theta_1 + (m_2 l_{g2} + m_w l_2) \\ & g\sin(\theta_1+\theta_2),\ (m_2 l_{g2} + m_w l_2)g\sin(\theta_1+\theta_2)]^T\ ,\end{aligned} \tag{2.39}$$

where $g = 9.8[m/s^2]$.

A two-link robot manipulator has two singular configurations when θ_2 equals to 0 or π. The determinant of the Jacobian matrix $\boldsymbol{J}$ becomes zero at the singular configurations. In this dissertation, the singular configuration in Fig. 2.4(a) is called C_0 , and the one in Fig. 2.4(b) is called C_π.

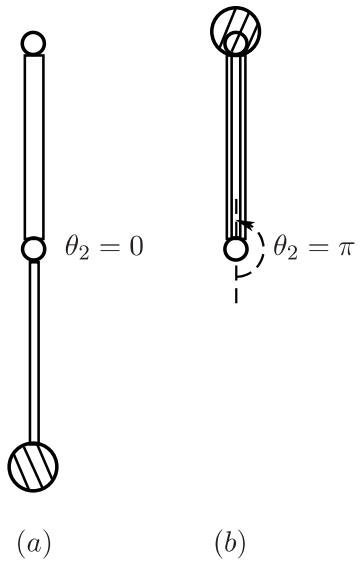

Figure 2.4: Singular configurations of a two-link manipulator: (a)C_0 : $\theta_2 = 0$. (b)C_π : $\theta_2 = \pi$

2.4 Features of Singular Configurations in the Literature

Singular configurations of a two-link robot manipulator have the following features:

a) Large loads can be sustained by small joint torques near singular configurations.

b) Joint torques can generate the kinetic energy efficiently near singular configurations.

Since the features a) and b) have been theoretically demonstrated in [16], brief descriptions are given as below.

Feature a) comes from the relationship between joint torques and the force at the end-effector as (1.3). According to (2.33), small changes in joint angles $\delta \boldsymbol{q}$ cause changes in end-effector $\delta \boldsymbol{p}_e$ as $\delta \boldsymbol{p}_e = \boldsymbol{J}(\boldsymbol{q})\delta \boldsymbol{q}$. When the robot is in C_0 as shown in Fig. 2.4 (a) with $\boldsymbol{q} = \boldsymbol{0}$, the Jacobian matrix $\boldsymbol{J}(\boldsymbol{q})$ becomes

$$\boldsymbol{J}(0) = \begin{bmatrix} l_1 + l_2 & l_2 \\ 0 & 0 \end{bmatrix}. \tag{2.40}$$

The end-effector loses a degree of freedom in the y-axis, and the vertical velocity of end-effector $\dot{y}_e$ equals zero no matter how large joint velocities are given. In statics, (1.3) shows that if a vertical force $\boldsymbol{F} = [\ 0 \quad F_y\ ]^T$ acts on the end-effector in C_0, the necessary joint torques to sustain the force are also equal to zero. In other words, an infinitesimal torque $\boldsymbol{\tau}$ can cause a finite force $\boldsymbol{F}$ in the y-axis near C_0.

The feature b) is derived from the analysis of the inertia matrix $\boldsymbol{M}$ in (2.36) under an assumption that the object is much heavier than the manipulator ($m_w \gg m_1, m_2$). The inertia matrix $\boldsymbol{M}$ can be represented as

$$\boldsymbol{M} = \lambda_1 \boldsymbol{e}_{\lambda_1} \boldsymbol{e}_{\lambda_1}^T + \lambda_2 \boldsymbol{e}_{\lambda_2} \boldsymbol{e}_{\lambda_2}^T, \tag{2.41}$$

where λ_1 and λ_2 denote the two eigenvalues of $\boldsymbol{M}$ ($\lambda_1 \leq \lambda_2$), and $\boldsymbol{e}_{\lambda_1}$ and $\boldsymbol{e}_{\lambda_2}$ are the corresponding eigenvectors. When the robot is in a configuration far away from a singular one, the inertia matrix almost equals to $\boldsymbol{M} \approx m_w \boldsymbol{J}^T \boldsymbol{J}$, and the eigenvalues λ_1 and λ_2 can be expressed as

$$\lambda_1 = O(m_w)\ , \lambda_2 = O(m_w), \tag{2.42}$$

where $O(*)$ is the big O notation. When the robot is in C_0 or C_π, the eigenvalues become

$$\lambda_1 = O(1)\ , \lambda_2 = O(m_w). \tag{2.43}$$

When the robot is in C_0, $\boldsymbol{e}_{\lambda_1} \approx \boldsymbol{c}_0 / \|\boldsymbol{c}_0\|$, where $\boldsymbol{c}_0 = [l_2, -(l_1 + l_2)]^T$. When the robot is in C_π, $\boldsymbol{e}_{\lambda_1} \approx \boldsymbol{c}_\pi / \|\boldsymbol{c}_\pi\|$, where $\boldsymbol{c}_\pi = [l_2, l_1 - l_2]^T$.

By supposing that the robot moves from rest in a horizontal plane, the equation (2.35) can be rewritten as

$$\ddot{\boldsymbol{q}} = \boldsymbol{M}^{-1} \boldsymbol{\tau}, \tag{2.44}$$

where $\boldsymbol{h} = \mathbf{0}$ and $\boldsymbol{\tau}_g = \mathbf{0}$. The work done by joint torques over a small time interval δt can be expressed by

$$\begin{aligned} W_J &\approx \frac{\delta t^2}{2} \boldsymbol{\tau}^T \boldsymbol{M}^{-1} \boldsymbol{\tau} \\ &= \frac{\delta t^2}{2} \boldsymbol{\tau}^T \left(\frac{1}{\lambda_1} \boldsymbol{e}_{\lambda_1} \boldsymbol{e}_{\lambda_1}^T + \frac{1}{\lambda_2} \boldsymbol{e}_{\lambda_2} \boldsymbol{e}_{\lambda_2}^T \right) \boldsymbol{\tau}. \end{aligned} \tag{2.45}$$

The joint torques are supposed to be bounded as $\|\boldsymbol{\tau}\| = O(1)$. When the robot configuration is far away from the singular configurations, the work remains $W_J = O(\frac{1}{m_w})\delta t^2$ from (2.42) and (2.45), no matter how the joint torques are chosen. When the manipulator is in a singular configuration and the joint torques satisfy $\boldsymbol{\tau} \parallel \boldsymbol{e}_{\lambda_1}$, the work done by these joint torques becomes $W_J = O(1)\delta t^2$ from (2.43) and (2.45). The value is much larger than the one in other configurations, and leads to feature b). For more details of the feature b), please see the literature [16].

2.5 Novel Features of Singular Configurations

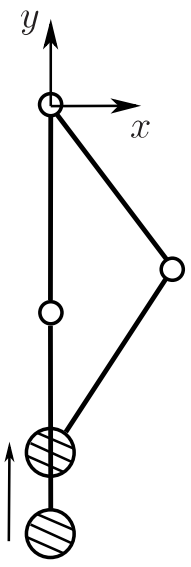

Figure 2.5: Lifting up motion of a two-link manipulator

This dissertation points out two other features of the singular configurations:

c) The energy is stored in the manipulator and causes large acceleration near singular configurations.

d) The torque-dependent acceleration of the object has its largest value when the robot configuration is close to, but not exactly, a singular configuration.

These features will show the usefulness for accelerating a heavy object attached to the end-effector.

In [16], it has been shown that singular configurations of a two-link manipulator is advantageous in lifting up a heavy object along y-axis as shown in Fig. 2.5. At the start time of the lifting motion, the configuration of the manipulator is C_0, and the joint motion along $\boldsymbol{e}_{\lambda_1}$ does not change x_e. The lifting motion along y-axis can utilize the above-mentioned feature b) and the feature c), in order to reduce the joint torques necessary for the motion. And also, another feature d) can be observed in the motion along y-axis.

This section will analyze the acceleration of the end-effector to reveal the features c) and d) by using a simplified model. In order to obtain analytical solution to the acceleration, the following assumptions are made:

1. The mass of the object is much larger than the mass and inertia of the manipulator.

2. The heavy object moves in y-axis, that is,

$$x_e = 0. \tag{2.46}$$

3. The input torques $\boldsymbol{\tau}$ are bounded and $O(1)$.

4. The length of link 1 equals to the one of link 2, that is,

$$l_1 = l_2 = l. \tag{2.47}$$

From (2.46) and (2.47), the joint angles must satisfy

$$\theta_2 = -2\theta_1, \dot{\theta}_2 = -2\dot{\theta}_1. \tag{2.48}$$

Therefore, the degrees of freedom of the manipulator are reduced from two to one as θ_1.

The acceleration of the end-effector is obtained as

$$\boldsymbol{a} = \ddot{\boldsymbol{p}}_e = \boldsymbol{J}(\boldsymbol{q})\ddot{\boldsymbol{q}} + \dot{\boldsymbol{J}}(\boldsymbol{q}, \dot{\boldsymbol{q}})\dot{\boldsymbol{q}} \tag{2.49}$$

By substituting (2.35) into (2.49), the acceleration $\boldsymbol{a}$ can be divided into three terms as

$$\boldsymbol{a} = \boldsymbol{a}_t + \boldsymbol{a}_g + \boldsymbol{a}_v \tag{2.50}$$

where

$$\boldsymbol{a}_t = \boldsymbol{J}\boldsymbol{M}^{-1}\boldsymbol{\tau} \,, \tag{2.51}$$
$$\boldsymbol{a}_g = -\boldsymbol{J}\boldsymbol{M}^{-1}\boldsymbol{\tau}_g \,, \tag{2.52}$$
$$\boldsymbol{a}_v = -\boldsymbol{J}\boldsymbol{M}^{-1}\boldsymbol{h} + \dot{\boldsymbol{J}}(\boldsymbol{q},\dot{\boldsymbol{q}})\dot{\boldsymbol{q}} \,. \tag{2.53}$$

The accelerations $\boldsymbol{a}_t$, $\boldsymbol{a}_g$ and $\boldsymbol{a}_v$ represent the components of $\boldsymbol{a}$ dependent on joint torques, gravity and joint velocities respectively. From the assumption 2, only the vertical components of $\boldsymbol{a}_t$, $\boldsymbol{a}_g$ and $\boldsymbol{a}_v$, that is, a_{ty}, a_{gy} and a_{vy}, will be analyzed. Without loss of generality, the range of θ_1 can be set to be $0 \leq \theta_1 \leq \pi$ for the analysis. In addition, it can be easily checked that the following equations hold:

$$\begin{aligned} &a_{ty}(\theta_1) = -a_{ty}(\pi - \theta_1) \,, a_{gy}(\theta_1) = a_{gy}(\pi - \theta_1) \,, \\ &a_{vy}(\theta_1) = -a_{vy}(\pi - \theta_1) \,. \end{aligned} \tag{2.54}$$

From (2.54), it is enough to analyze the acceleration when $0 \leq \theta_1 \leq \frac{\pi}{2}$. It should be noted that C_0 and C_π correspond to $\theta_1 = 0$ and $\frac{\pi}{2}$ respectively.

From the assumption 1, the physical parameters other than m_w are $O(1)$ and $m_w \gg O(1)$. The accelerations of a_{ty}, a_{gy} and a_{vy} depend on m_w, the physical parameters of $O(1)$, the kinetic energy E (or $\dot{\theta}_1$) and the angle θ_1. In the following subsections, their approximate solutions will be obtained as functions of θ_1 by neglecting small terms, under the condition that E of $O(1)$ is given.

2.5.1 Torque-dependent acceleration

The torque-dependent acceleration a_{ty} can be approximately obtained from (2.47), (2.48) and (2.51) as

$$\begin{aligned} a_{ty} \approx & \frac{l\sqrt{1-c^2}}{4m_w^2 l^4 c^2(1-c^2) + K_1 m_w l^2} \{-(2c^2 l^2 m_w + K_2 + (2c^2-1)m_2 l l_{g2})\tau_1 \\ & - (4c^2 l^2 m_w + K_1 + 4c^2 m_2 l l_{g2})\tau_2\} \,, \end{aligned} \tag{2.55}$$

where $c = \cos(\theta_1)$, $K_1 = m_1 l_{g1}^2 + m_2(l - l_{g2})^2 + I_1 + I_2$ and $K_2 = I_2 + m_2 l_{g2}^2$.

Table 2.1: Physical paramaters for acceleration analysis

$m_1 = 1[kg]$	$m_2 = 1[kg]$	$m_w = 30[kg]$
$l_1 = 0.3[m]$	$l_2 = 0.3[m]$	$l_{g1} = 0.15[m]$
$l_{g2} = 0.15[m]$	$I_1 = 0.1[\mathrm{kgm}^2]$	$I_2 = 0.1[\mathrm{kgm}^2]$

From assumption 1, the angles $\theta_1 = O(\frac{1}{\sqrt{m_w}})$ and $\theta_1 = \frac{\pi}{2} - O(\frac{1}{\sqrt{m_w}})$ correspond to the robot configurations extremely close to C_0 and C_π respectively. When $\theta_1 \in [0, \frac{\pi}{2} - O(\frac{1}{\sqrt{m_w}})]$, the terms $2c^2l^2m_w$ and $4c^2l^2m_w$ are much larger than the ones $K_2 + (2c^2 - 1)m_2ll_{g2} = O(1)$ and $K_1 + 4c^2m_2ll_{g2} = O(1)$. Therefore, (2.55) can be approximated as

$$a_{ty} \approx \frac{-2ls(1-s^2)}{4m_wl^2s^2(1-s^2) + K_1}\{-\tau_1 + 2\tau_2\}\ , \tag{2.56}$$

where $s = \sin(\theta_1)$.

The variation of a_{ty} from (2.56) will be investigated by supposing that τ_1 and τ_2 are constants. For $s = 0$, the configuration of the manipulator is C_0, and the value of a_{ty} equals zero. The absolute value of a_{ty}, $|a_{ty}|$, has a maximum value of $O(\frac{1}{\sqrt{m_w}})$ at $s = s^*$, where $s^* = \frac{1}{2l}\sqrt{\frac{K_1}{m_w}} \ll 1$. The configuration that corresponds to s^* is very close to C_0 from the assumption 1. The absolute value of a_{ty} monotonically decreases to $O(\frac{1}{m_w})$ as s increases from s^*. Therefore, the acceleration a_{ty} varies intensely near C_0, and can be much larger than the one far away from C_0. The variation of a_{ty} leads to feature d):

d) The torque-dependent acceleration of the object has its largest value when the robot configuration is close to, but not exactly, a singular configuration.

Moreover, from (2.56), joint torques must satisfy the following relation to generate the maximum values of $a_{ty}(s^*)$:

$$\frac{\tau_2}{\tau_1} = \frac{2}{-1} \text{ for } s^*. \tag{2.57}$$

The joint torques that satisfy $|\boldsymbol{\tau}| = 15$ and (2.57) are chosen, and the profiles of the actual value of a_{ty} from (2.51) and the approximate value of a_{ty} from (2.56) are drawn as shown in Fig. 2.6. In this section, the physical parameters in Table 2.1 are used.

Remark 1: The behavior of a_{ty} observed in this subsection remains unchanged even when $l_1 \neq l_2$. The maximum value of $|a_{ty}|$ is also $O(\frac{1}{\sqrt{m_w}})$ at $s = s^* = \frac{1}{l_1+l_2}\sqrt{\frac{K_1'}{m_w}}$, where

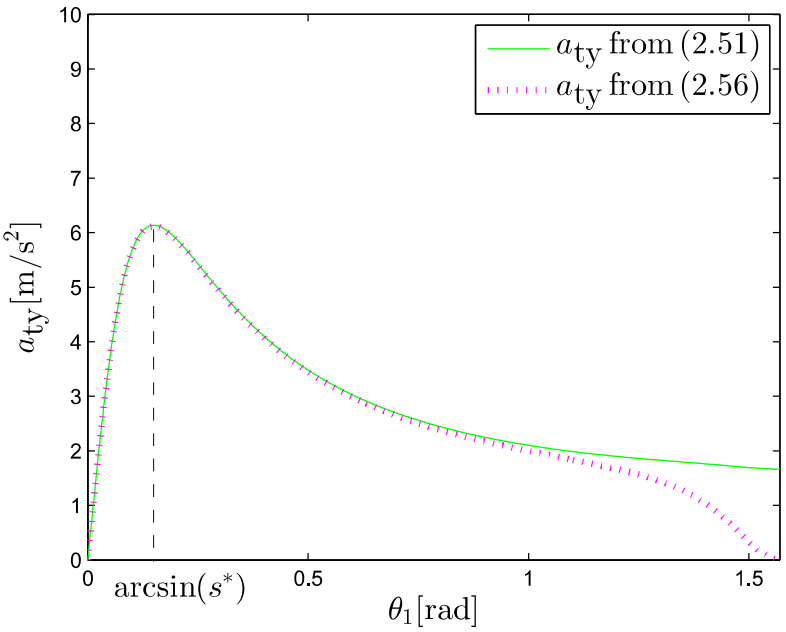

Figure 2.6: Variation of a_{ty} with respect to θ_1

$K_1' = k^2 m_1 l_{g1}^2 + m_2(kl_1 - l_{g2})^2 + k^2 I_1 + I_2 = O(1)$ and $k = l_2/l_1$. The required joint torques to generate large acceleration near the singular configurations are chosen as follows:

$$\frac{\tau_2}{\tau_1} = \frac{l_1 + l_2}{-l_2} \text{ for } s^* , \tag{2.58}$$

The ratio of τ_1 to τ_2 for C_0 equals to the one obtained in [16, 74], and both the feature b) and the feature d) can be utilized simultaneously.

Remark 2: The torque-dependent acceleration in (2.51) has been analyzed in terms of the dynamic manipulability so far [64]. The drastic variation of a_{ty} near C_0 corresponds to the drastic change in the shape of the dynamic manipulability ellipsoid, as shown in Appendix 2.A.

2.5.2 Gravity-dependent acceleration

From (2.46), (2.47) and (2.48), $\boldsymbol{\tau}_g$ is rewritten as

$$\boldsymbol{\tau}_g = [(m_1 l_{g1} + m_2(l - l_{g2}))sg, -(m_2 l_{g2} + m_w l)sg]. \tag{2.59}$$

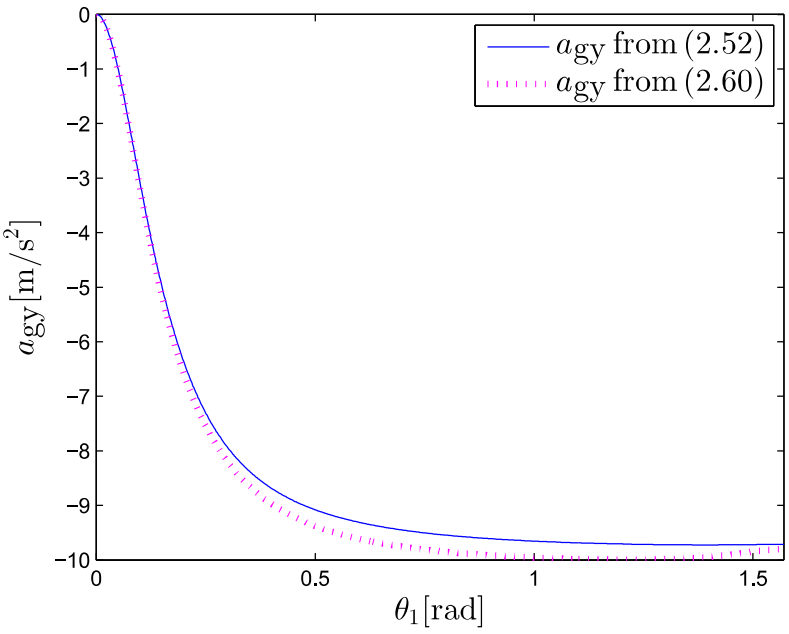

Figure 2.7: Variation of a_{gy} with respect to θ_1

Substituting it into (2.52), a_{gy} can be approximately computed for $\theta_1 \in [0, \frac{\pi}{2}]$ as

$$a_{gy} \approx \frac{-s^2 g}{4m_w l^2 s^2(1-s^2)+K_1}\{4m_w l^2(1-s^2)+2l(1-s^2)(m_1 l_{g1}+m_2(l+3l_{g2}))+K_1\}\ . \tag{2.60}$$

In statics, $\boldsymbol{\tau}_g$ approximately equals to the joint torques necessary to sustain the load $m_w g$. When the manipulator is in C_0, $\boldsymbol{\tau}_g$ equals zero from (2.59), which corresponds to the feature a). The absolute value of a_{gy}, $|a_{gy}|$, intensely increases from 0 to g as s increases from 0. In C_0, the gravity has no effect on the acceleration of the end-effector.

The profiles of the actual value of a_{gy} from (2.52) and the approximate value of a_{gy} from (2.60) are drawn as shown in Fig. 2.7.

2.5.3 Velocity-dependent acceleration

From (2.46), (2.47) and (2.48), $\boldsymbol{h}$ can be rewritten as

$$\boldsymbol{h} = [0, -2\tilde{k}_2 s\sqrt{1-s^2}\dot{\theta}_1^2]^T, \tag{2.61}$$

where $\tilde{k}_2 = m_2 l l_{g2} + m_w l_1^2 = O(m_w)$. It is assumed that the kinetic energy is constant and $O(1)$. The same amount of energy causes different accelerations as the robot configuration varies. The energy can be rewritten from (2.38) as

$$E = \frac{1}{2}(K_1 + 2(2s^2 - 1)\tilde{k}_2)\dot{\theta}_1^2 \ , \tag{2.62}$$

Substituting (2.61) into (2.53), a_{vy} is approximately obtained for $\theta_1 \in [0, \frac{\pi}{2}]$ as

$$\begin{aligned} a_{vy} &\approx \frac{2K_1 l\sqrt{1-s^2}\dot{\theta}_1^2}{4m_w l^2 s^2(1-s^2) + K_1} \\ &\approx \frac{4K_1 l\sqrt{1-s^2}E}{(4m_w l^2 s^2(1-s^2) + K_1)(K_1 + 4s^2\tilde{k}_2)} \ . \end{aligned} \tag{2.63}$$

From (2.62), the joint velocity $\dot{\theta}_1$ equals to $O(1)$ at $s = 0$, and rapidly decreases to $O(\frac{1}{\sqrt{m_w}})$ as s increases. The velocity-dependent acceleration a_{vy} intensely decreases from $O(1)$ to $O(\frac{1}{m_w})$ as s increases from 0. The variation of a_{vy} leads to feature c), that is,

c) The energy is stored in the manipulator and causes large acceleration near singular configurations.

When the manipulator is in C_0, if the vector of joint velocities is parallel to the one of joint torques in (2.57), the velocity of the end-effector is zero. Kinetic energy of the whole system is stored as rotational one of the manipulator, and the joint velocities is relatively large from (2.62). Thus, a_{vy} becomes very large from (2.63). That is the reason why large acceleration can be caused in C_0.

The profiles of the actual value of a_{vy} from (2.53) and the approximate value of a_{vy} from (2.63) are drawn as shown in Fig. 2.8 with $E = 0.4$.

Remark 3: Even when $l_1 \neq l_2$, large acceleration can also be caused by the kinetic energy in C_0. The vector of joint velocities should be parallel to the one of joint torques in (2.58) to cause the largest acceleration.

2.5.4 Total acceleration

In summary, the variations of a_{gy}, a_{vy} and a_{ty} correspond to features a), c) and d) of singular configurations respectively. The theoretical results illustrate that the kinetic energy E of $O(1)$ can cause an acceleration of $O(1)$ in C_0, and the bounded joint torques $\boldsymbol{\tau}$ of $O(1)$ can cause an acceleration of $O(1/\sqrt{m_w})$ for $s = s^*$, that is, for the configuration close to C_0. When the object is lifted up, a_{ty} and a_{vy} can be manipulated by $\boldsymbol{\tau}$ directly or indirectly, and can

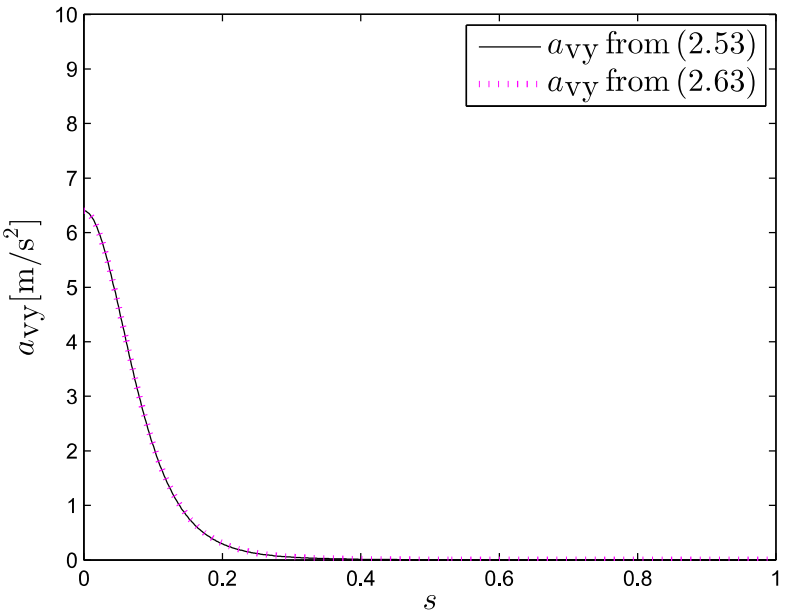

Figure 2.8: Variation of a_{vy} with respect to θ_1

make a_y greatly large near C_0. The acceleration a_{gy} only depends on the configuration of the manipulator and opposes the upward movement of the object. However, it equals zero in C_0, and does not spoil the large accelerations a_{ty} and a_{vy}. When the robot gets far away from C_0, a_{ty} and a_{vy} rapidly decrease to $O(1/m_w)$, and the downward acceleration of a_{gy} increases to g. Consequently, it is very difficult to generate a large upward acceleration with small joint torques in the configurations far away from C_0, but it is much easier near C_0.

From (2.50), (2.51), (2.52) and (2.53), the profiles of the actual values of a_{ty}, a_{gy}, a_{vy} and their resultant acceleration a_y are drawn in Fig. 2.9. The total acceleration a_y can be large due to a_{ty} and a_{vy} near C_0, that is, $\theta_1 = 0$, as mentioned above.

Remark 4: When the motion of the end-effector $\boldsymbol{p}_e$ is restricted on the y-axis, $\ddot{\theta}_1$ and $\ddot{\theta}_2$ should satisfy the condition that $\ddot{\theta}_2 = -2\ddot{\theta}_1$. If the end-effector can be accelerated along the x-axis without the condition, the accelerations of a_{tx}, a_{gx} and a_{vx} can be approximately calculated on the y-axis by a similar analysis. Refer to Appendix 2.B for details.

2.6 Conclusion

This chapter listed the features of singular configurations, examined the acceleration of the end-effector of a two-link manipulator and revealed dynamic features of singular configura-

tions by theoretical analysis. In the remaining chapters, some typical robot motions will be cited to show the dynamic advantage of the features.

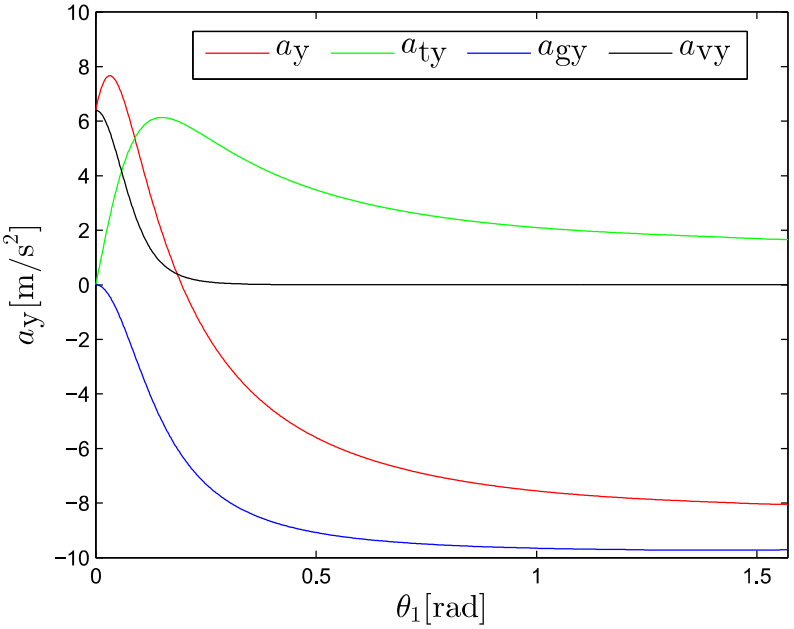

Figure 2.9: Total acceleration $\boldsymbol{a}_y$ with respect to θ_1

Appendix 2.A Dynamic Manipulability

The acceleration $\boldsymbol{a}_t$ corresponds to the dynamic manipulability ellipsoid with $\dot{\boldsymbol{q}} = 0$ and no gravity effect. The ellipsoid is defined by

$$\boldsymbol{a}_t^T (\boldsymbol{M}\boldsymbol{J}^{-1})^T \boldsymbol{M}\boldsymbol{J}^{-1} \boldsymbol{a}_t = \boldsymbol{\tau}^T \boldsymbol{\tau} \leq 1. \tag{2.64}$$

The ellipsoid directly illustrates the relation between bounded joint torques and maximum end-effector acceleration in each direction. Fig. 2.10 shows the dynamic manipulability ellipsoids with different postures by using the physical parameters in Table 2.1.

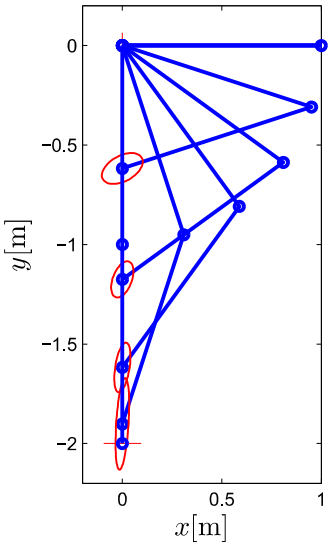

Figure 2.10: Dynamic manipulability ellipsoid

It is noticed that the shape of the ellipsoid changes rapidly when the robot approaches its singular configurations. The maximum possible acceleration in y-axis firstly increases as the arm extends, and reaches the peak when the arm is almost extended. From then on, it intensely decreases to 0 with the arm extended fully. The similar phenomenon related to the maximum acceleration in x-axis also can be found near the singular configuration when the arm is folded.

Appendix 2.B Horizontal Acceleration Analysis

If $\ddot{\theta}_2 \neq -2\ddot{\theta}_1$, the horizontal component of $\boldsymbol{a}$ does not identically equal zero. Under the same assumptions as in Section 2.5, the horizontal components of $\boldsymbol{a}_t$, $\boldsymbol{a}_g$ and $\boldsymbol{a}_v$, that is, a_{tx}, a_{gx} and

a_{vx}, will be investigated.

Torque-dependent Acceleration

When $\theta_1 \in [0, \frac{\pi}{2}]$, the horizontal term a_{tx} of $\boldsymbol{a}_t$ can be approximately obtained from (2.47), (2.48) and (2.51) as

$$a_{tx} \approx \frac{l\sqrt{1-s^2}}{4m_w^2 l^4 s^2(1-s^2)+K_1 m_w l^2}\{(2s^2 l^2 m_w + K_2 + (2s^2-1)m_2 l l_{g2})\tau_1 + K_3\tau_2\}, \tag{2.65}$$

where $K_2 = I_2 + m_2 l_{g2}^2 = O(1)$ and $K_3 = m_1 l_{g1}^2 + m_2(l^2 - l_{g2}^2) + I_1 - I_2 = O(1)$. When $\theta_1 \in [O(\frac{1}{\sqrt{m_w}}), \frac{\pi}{2}]$, the term $2s^2 l^2 m_w$ is much larger than the ones $K_2 + (2s^2-1)m_2 l l_{g2} = O(1)$ and $K_3 = O(1)$. Therefore, (2.65) can be approximated as

$$a_{tx} \approx \frac{2lc(1-c^2)\tau_1}{4m_w l^2 c^2(1-c^2)+K_1}. \tag{2.66}$$

The absolute value of a_{tx}, $|a_{tx}|$, also has a peak value at $c = c^*$, where $c^* = \frac{1}{2l}\sqrt{\frac{K_1}{m_w}} \ll 1$. According to (2.66), joint torques must satisfy the following relation to generate the maximum values of $a_{tx}(c^*)$:

$$\frac{\tau_2}{\tau_1} = \frac{0}{1} \text{ for } c^*. \tag{2.67}$$

The joint torques that satisfy $\|\boldsymbol{\tau}\| = 15$ and (2.67) are chosen, and the profiles of the actual value of a_{tx} from (2.51) and the approximate value of a_{tx} from (2.66) are drawn in Fig. 2.11 with the physical parameters in Table 2.1. The drastic variation of a_{tx} near C_π corresponds to the drastic change in the shape of the dynamic manipulability ellipsoid.

Gravity-dependent acceleration

Substituting (2.59) into (2.52), a_{gx} can be approximately computed for $\theta_1 \in [0, \frac{\pi}{2}]$ as

$$a_{gx} \approx \frac{-\sqrt{1-s^2}sg\{2ls^2(m_1 l_{g1} + m_2(l - l_{g2})) - K_3\}}{4m_w l^2 s^2(1-s^2)+K_1}. \tag{2.68}$$

The acceleration a_{gx} has one local maximum and one local minimum of $O(\frac{1}{\sqrt{m_w}})$ near the singular configurations.

The profiles of the actual value of a_{gx} from (2.52) and the approximate value of a_{gx} from (2.68) are drawn as shown in Fig. 2.12.

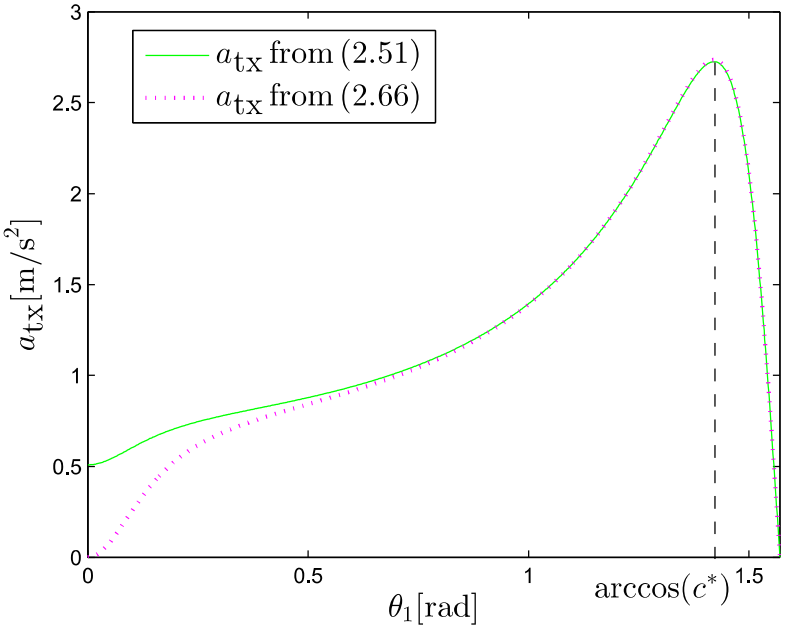

Figure 2.11: Variation of a_{tx} with respect to θ_1

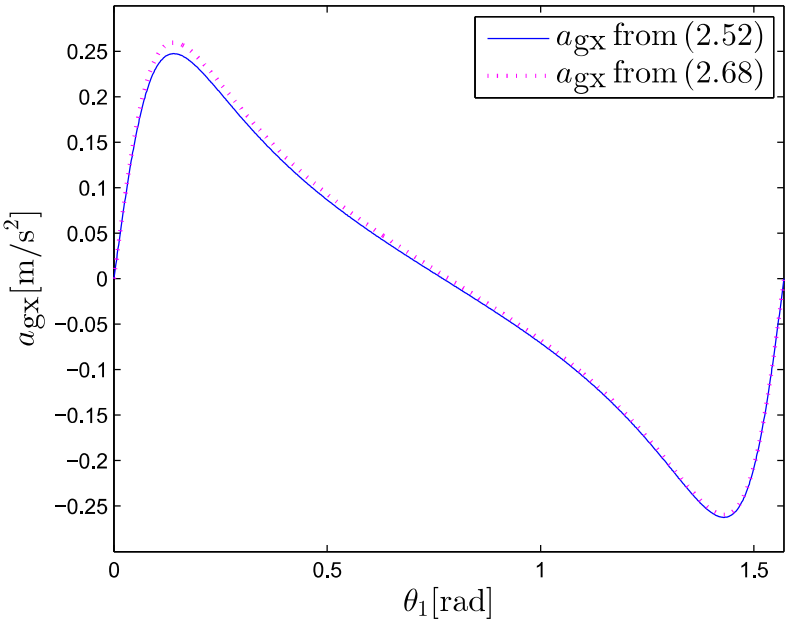

Figure 2.12: Variation of a_{gx} with respect to θ_1

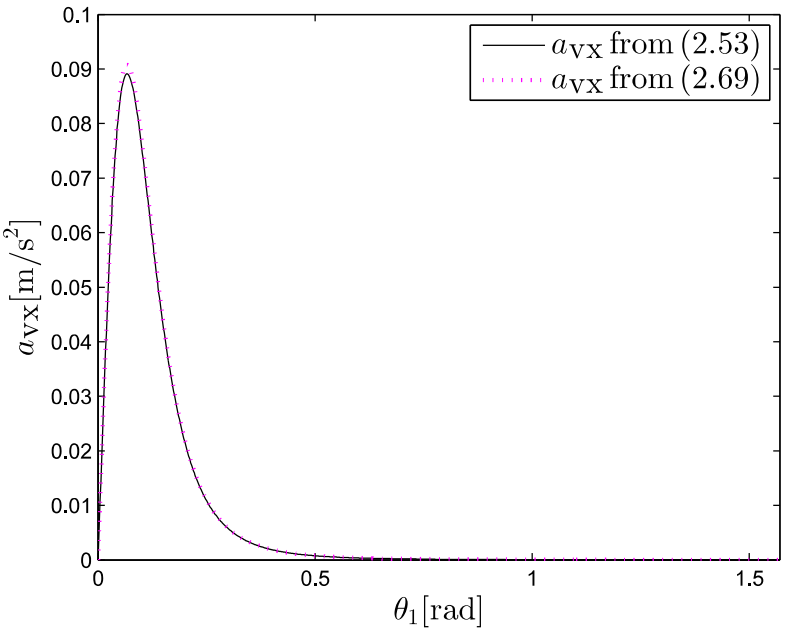

Figure 2.13: Variation of a_{vx} with respect to θ_1

Velocity-dependent acceleration

Substituting (2.61) into (2.53), a_{vx} is approximately obtained for $\theta_1 \in [0, \frac{\pi}{2}]$ as

$$a_{vx} \approx -\frac{2K_3 ls(1-s^2)\dot{\theta}_1^2}{4m_w l^2 s^2(1-s^2)+K_1}, \tag{2.69}$$

which has a peak value of $O(\frac{1}{\sqrt{m_w}})$ at $s = \frac{1}{2l}\sqrt{\frac{K_1}{2m_w}}$.

The profiles of the actual value of a_{vx} from (2.53) and the approximate value of a_{vx} from (2.69) are drawn in Fig. 2.13.

It should be noted that, when $l_1 \neq l_2$, the approximate solution of a_{vx} is quite different from (2.69). A large a_{vx} of $(l_1 - l_2)O(1)$ is caused from the energy of $O(1)$ in the singular configuration C_π.

Total acceleration

From (2.50), (2.51), (2.52) and (2.53), the profiles of the actual values of a_{tx}, a_{gx}, a_{vx} and their resultant acceleration a_x are drawn in Fig. 2.14 with the same physical parameters used for drawing Fig. 2.9. Comparing Figs. 2.9 and 2.14, it is found that when the robot moves along y-axis, the maximum value of a_{vx} are much smaller than the one of a_{vy} if the kinetic energy E is given. When $\|\boldsymbol{\tau}\| = O(1)$, the maximum achievable value of a_{tx} near C_π is also smaller than

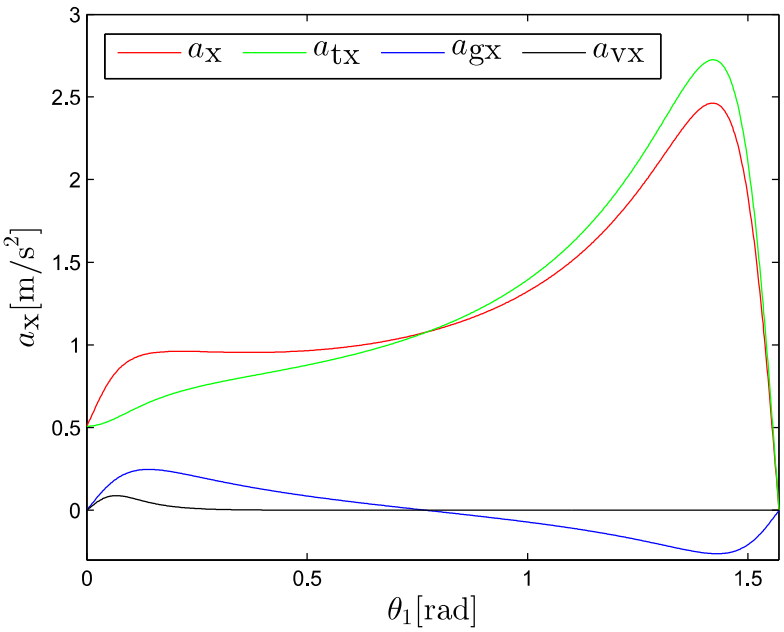

Figure 2.14: Total acceleration a_x with respect to θ_1

the one of a_{ty} near C_0. The peak value of $|a_{gx}|$ is also small by comparing to the one of $|a_{gy}|$.

Chapter 3

Lifting and Dragging Motions of Robot Manipulators

3.1 Introduction

This chapter attempts to find whether the features of singular configurations in Chapter 2 can be utilized in the lifting motions of a two-link robot manipulator with fixed base and in dragging motion of a two-link mobile manipulator with unfixed base. The lifting motions of a two-link robot manipulator includes two illustrative ones, a lifting motion in Section 3.2 and a weight lifting motion in Section 3.3. In the lifting motion, a heavy object is lifted up a certain height. In the weight lifting motion, a heavy object is lifted up from the lowest position to the highest one. The model of the robot manipulator is the same as the one introduced in Section 2.3. In the dragging motion of a mobile manipulator that will be shown in Section 3.4, a heavy object is dragged a certain distance in a horizontal plane. The mobile manipulator is composed of a wheeled base and a two-link robot manipulator. In order to know what motion can generate a large force with relatively small input torques to pull the heavy object, this chapter searches for the optimal motions of the robot manipulators, where the integral of squared input torques is minimized. Since an actual robot usually has the upper limits of torques, the minimization of torques could make the task be more easily realized. For the mobile manipulator powered by the batteries, the energy consumption necessary for the task achievement can also be reduced, and the number of achievable tasks can be increased before running out of batteries.

In Section 3.4.4, the dynamics of the mobile manipulator in dragging a heavy object will be theoretically analyzed by using a simplified model. The subsection will show through a novel theoretical analysis that the features of the singular configuration can also be utilized

in the dragging motion. The energy can be generated more efficiently from the joint torques near the singular configuration than from the torques at the wheels. The pulling force caused from the energy near the singular configuration is much larger than the force provided directly from the joint torques, that is, the feature c) has a bigger influence on the motion of dragging a heavy object by a mobile manipulator than the feature d).

3.2 Lifting Motion of a Two-link Robot Manipulator

3.2.1 Problem formulation

The heavy object is pulled a desired height from the singular configuration in a similar way as in [16]. In this section, the horizontal movement of the end-effector is not completely restricted. The boundaries on $(\dot{x}_e, \dot{y}_e)$ at the start time, $t = 0$, and the end time, $t = T$, are given as follows:

$$\begin{aligned} (x_e,\ y_e)|_{t=0} &= (0, -l_1 - l_2),\ (\dot{x}_e,\ \dot{y}_e)|_{t=0} = (0,0), \\ (x_e,\ y_e)|_{t=T} &= (0, y_T),\ (\dot{x}_e,\ \dot{y}_e)|_{t=T} = (0,0) \end{aligned} \tag{3.1}$$

where y_T is the vertical position of the object at the end time T. According to the above equations, the joint angles at the start time and end time can be easily calculated.

A motion planning problem of achieving the lifting motion and minimizing the consumed joint torques is considered. The cost function for optimization are chosen as follows:

$$J_C(\xi) = \int_0^T \|\boldsymbol{\tau}\|^2 dt = \int_0^T (\tau_1^2 + \tau_2^2) dt\,, \tag{3.2}$$

where ξ represents the parameters for optimization, and is chosen as $\xi = \{\tau_1(t),\ \tau_2(t),\ T\}$. B-splines are used to express the joint torques, and the independent parameters of the B-splines will be optimized. See Appendix 3.A.1 for more details of B-splines.

3.2.2 Numerical results

The motions obtained by numerical optimization will be shown. The physical parameters of the two-link manipulator are chosen as shown in Table 3.1. The initial and final heights of the object are $y_0 = -0.65$[m] and $y_T = -0.45$[m]. MATLAB function fmincon was used to find the optimal parameters. To verify that the feature c) is very useful in the motion of passing through C_0 with larger energy, the numerical optimization was performed in two cases, Case 1 and Case 2. In Case 2, there is a condition on θ_2 as $\theta_2 \leq 0$. Under the condition, the manipulator starts directly from C_0 and cannot pass through C_0.

Table 3.1: Physical parameters of the two-link robot manipulator

l_1	0.3 [m]	l_2	0.35 [m]
l_{g1}	0.138 [m]	l_{g2}	0.179 [m]
I_1	0.121 [kgm^2]	I_2	0.118 [kgm^2]
m_1	0.8 [kg]	m_2	0.52 [kg]
m_w	2.5 [kg]		

Case 1

The red line in Fig. 3.1 represents the trajectory of the object. After the object is lifted up a little from the singular configuration C_0, the object falls down and the manipulator passes through C_0 again. The time histories of joint torques and vertical acceleration of the object are shown in Figs. 3.2 and 3.3 respectively. The dashed red line expresses the moment when the manipulator passes through C_0, and the corresponding time is 0.597[s]. The optimized duration time is $T = 0.905$[s], and the value of J_C for the obtained motion is 2.29[N^{2}m^{2}s].

All the features of singular configurations, a) to d), are used in the lifting motion. From Figs. 3.1, 3.2 and 3.3, the object is lifted up twice around $t = 0.2$[s] and $t = 0.6$[s]. The initial and final configurations are denoted as IC and FC respectively. The configuration of the manipulator changes in the pattern: IC(C_0) $\rightarrow C_0 \rightarrow$ FC. It is clear that a large acceleration is caused from features b) and c) for the second lift. The energy is stored during the first lift, and increased much by using the feature b) while approaching C_0 again. The increased energy causes the large acceleration a_{vy} from the feature c) as shown in Fig. 3.3. Due to the feature a), the negative acceleration from the gravity, a_{gy}, is small and does not spoil the large acceleration. Feature d) is also utilized to generate a large torque-dependent acceleration, a_{ty}, just after passing through C_0. The joint torques satisfy (2.58) around $t = 0.597$[s] as shown in Fig. 3.2. Although a_{ty} is negative before passing through C_0, the joint torques before C_0 are utilized to increase the energy and to obtain much larger a_{vy} after C_0. As the results of the accelerations, the object is strongly pulled up with relatively small joint torques.

Case 2

The red line in Fig. 3.4 represents the trajectory of the object. The configuration of the manipulator changes in the pattern: IC(C_0) $\rightarrow$ FC . The time histories of joint torques and vertical acceleration are shown in Figs. 3.5 and 3.6 respectively. For the obtained motion, $J_C = 4.62$[N^{2}m^{2}s] and $T = 0.522$[s]. The cost J_C is almost twice as much as the one in Case 1.

Although all the features can be utilized even in Case 2, the energy stored in the first lift and in approaching C_0 again for Case 1 makes the feature c) more remarkable. The more kinetic energy is generated near singular configurations, the larger acceleration can be caused from it as observed in from Figs. 3.3 and 3.6.

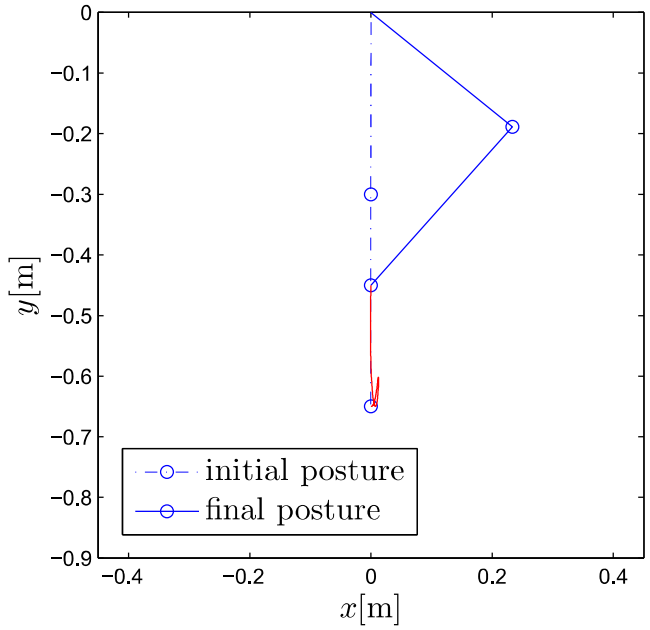

Figure 3.1: Initial and final postures of the robot for the optimized lifting motion (Case 1)

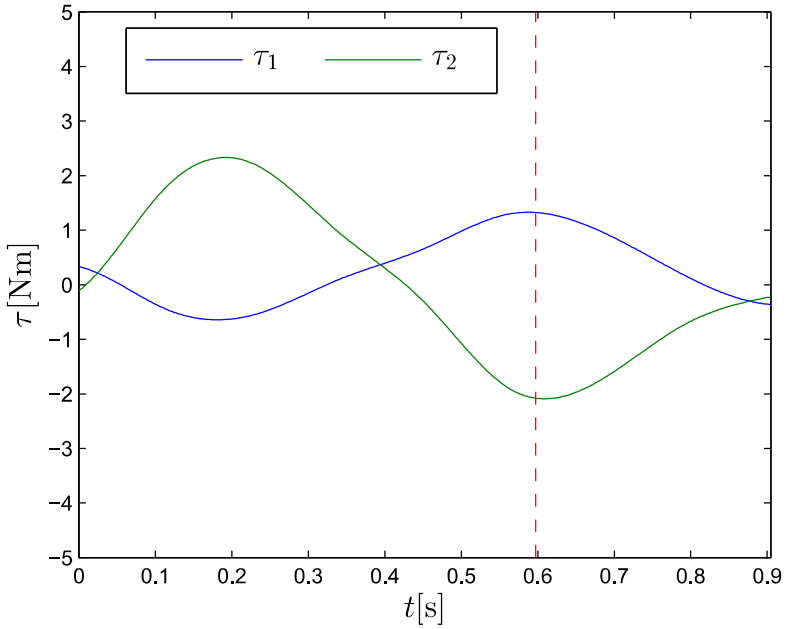

Figure 3.2: Time histories of joint torques (Case 1)

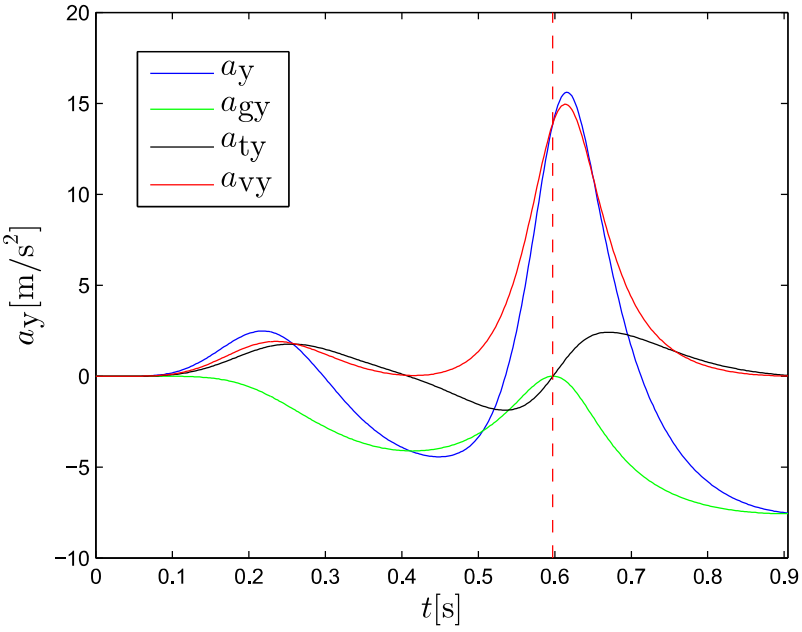

Figure 3.3: Time history of vertical acceleration of the heavy object (Case 1)

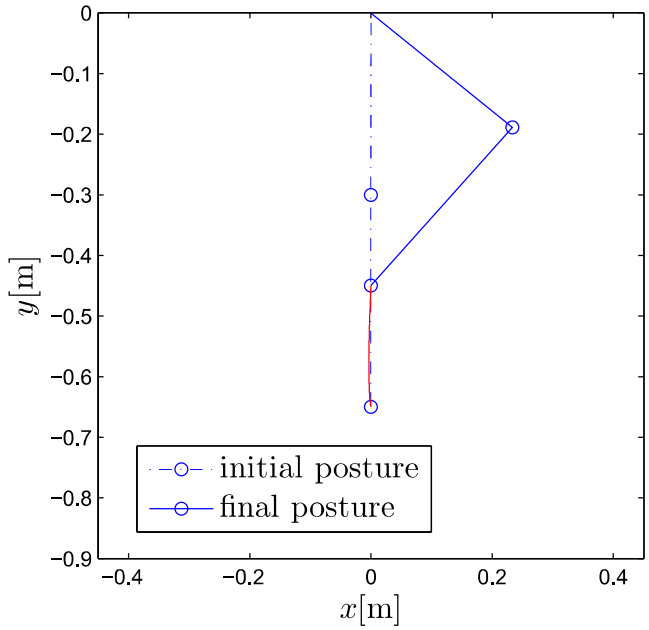

Figure 3.4: Initial and final postures of the robot for the optimized lifting motion (Case 2)

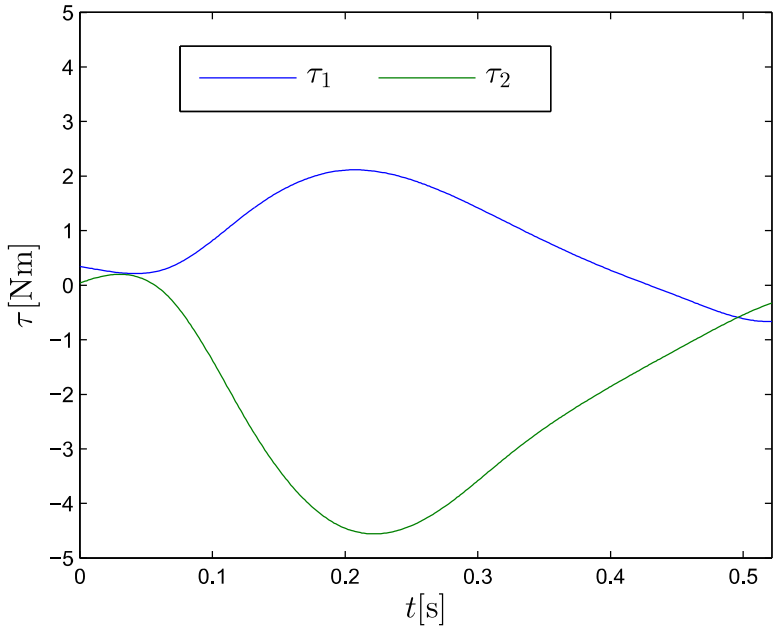

Figure 3.5: Time histories of joint torques (Case 2)

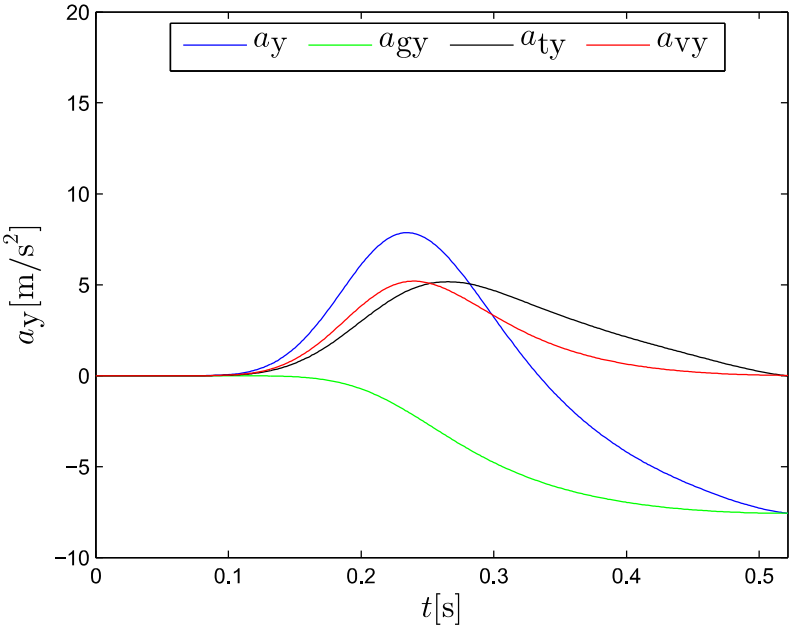

Figure 3.6: Time history of vertical acceleration of the heavy object (Case 2)

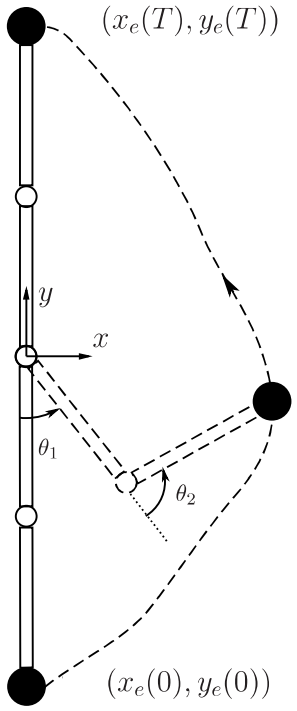

Figure 3.7: Task representation of weight lifting

3.3 Weight Lifting of a Two-link Robot Manipulator

Weight lifting of a two-link robot manipulator can be considered as a special case of the above lifting motion. In (3.1), the final height of the object is set to be $y_T = l_1 + l_2$, which means that the heavy object is moved from the lowest position to the highest one as shown in Fig. 3.7. The cost functions J_C and the parameters for optimization ξ are chosen as the same as the ones in the above section.

The solution obtained by numerical optimization will be shown. The physical parameters are used as the same as the ones in the above section, except that the mass of the object is set to be 3.1[kg]. MATLAB function fmincon is also used to find the optimal parameters.

The obtained motion shows that the robot passes through the singular configurations twice in Fig. 3.8. The green dashed line in Fig. 3.8 represents the configuration of the manipulator as in C_π. The configuration of the manipulator changes in the pattern: IC(C_0) $\rightarrow$ C_0 $\rightarrow$ C_π $\rightarrow$ FC(C_0). All the features of singular configuration are used in the obtained weight lifting motion. The motion of passing through C_0 is similar to the one in Case 1 of Section 3.2, and the motion of passing through C_π is also useful for generating large acceleration. At the end time, it is should be noted that the final posture is in C_0, and the required joint torques to sustain the object equal zero due to the feature a).

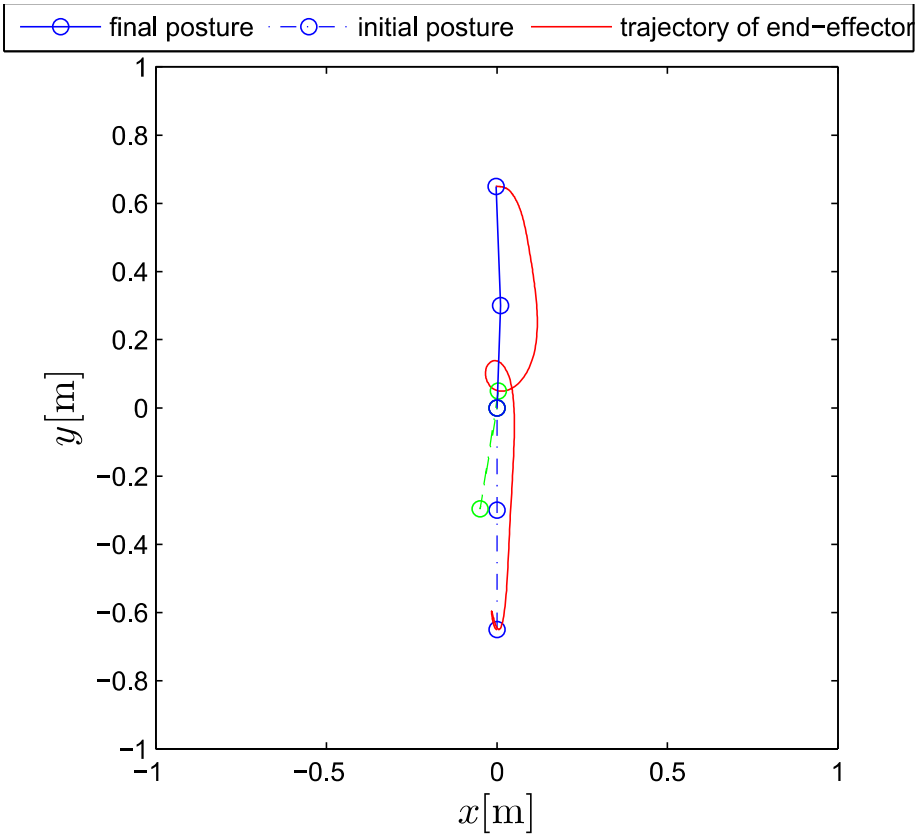

Figure 3.8: Optimized weight lifting

3.4 Pulling Motion of a Mobile Manipulator

This section investigates what motion of a mobile manipulator generates a large pulling force efficiently and attempts to unveil the dynamics of the motion. For dragging a heavy object, it is necessary to generate a large pulling force that is larger than the maximum static friction force applied to the object on the ground. In this section, an optimal motion planning problem will be solved to obtain the motion that generates the large pulling force with small joint torques.

3.4.1 Mobile manipulator

The mobile manipulator is composed of a wheeled base and a two-link robot manipulator. The base has two differentially driven wheels and support casters to keep the roll and pitch angles of the base zero. The hand of the two-link robot manipulator is supposed to grasp a heavy object. For simplicity, the following assumptions are made:

1. The wheeled base and the object move on a horizontal plane.

2. The orientation of the wheeled base is kept constant, that is, the two wheels rotate at the same velocity and the base moves along a straight line.

3. The connection between the object and the robot manipulator hand is modeled as a joint that freely rotates, and the joint is located at the mass center of the object.

4. The wheels of the base do not slip on the ground.

5. There are no frictions at the two joints of the robot manipulator.

From the assumptions 2 and 3, the rotations of the wheeled base and the object do not appear in the equations of motion. The base and the object can be modeled as mass points. Figs. 3.9 and 3.10 show a schematic model of a mobile manipulator with a heavy object and the experimental prototype. The masses of the base and object are denoted as m_b and m_o. From the assumption 2, it is supposed that the base moves along x-axis, without loss of generality. The location of the base is expressed as x_b. The position of the end-effector is denoted as $\boldsymbol{p}_e = [x_e, y_e]^T$. The rotation angle of the two wheels and the sum of driving torques applied to them are represented as θ_0 and τ_0. The inertia of each wheel around the rotation axis is expressed as I_w. The links and joints of the robot manipulator are called as, Link 1, Link 2, Joint 1 and Joint 2. The mass and length of Link i are denoted as m_i and l_i respectively ($i = 1, 2$). The moment of inertia of Link i and the distance from Joint i to the mass center of Link i are expressed by I_i and l_{gi}. The joint angles and torques with respect to Joint i are represented as θ_i and τ_i respectively. From the assumption 4, the velocity of contact point of the wheel with the ground must be zero, that is, $\dot{x}_b - R\dot{\theta}_0 = 0$ where R is the wheel radius. The generalized coordinates and the generalized forces for the mobile manipulator are expressed in vector forms as $\boldsymbol{q} = [x_b, \theta_1, \theta_2]^T$ and $\boldsymbol{\tau} = [\tau_0, \tau_1, \tau_2]^T$.

The velocity of the object is expressed by using generalized coordinates $\boldsymbol{q}$ as follows:

$$\dot{\boldsymbol{p}}_e = \boldsymbol{J}_e(\boldsymbol{q})\dot{\boldsymbol{q}}. \tag{3.3}$$

The Jacobian matrix $\boldsymbol{J}_e$ can be written as

$$\boldsymbol{J}_e(\boldsymbol{q}) = \begin{bmatrix} 1 & -l_1 \mathrm{s}\theta_1 - l_2 \mathrm{s}(\theta_1 + \theta_2) & -l_2 \mathrm{s}(\theta_1 + \theta_2) \\ 0 & l_1 \mathrm{c}\theta_1 + l_2 \mathrm{c}(\theta_1 + \theta_2) & l_2 \mathrm{c}(\theta_1 + \theta_2) \end{bmatrix}, \tag{3.4}$$

where c$*$ and s$*$ mean $\cos(*)$ and $\sin(*)$. The equations of motion for the mobile manipulator can be represented in the following form:

$$\boldsymbol{M}(\boldsymbol{q})\ddot{\boldsymbol{q}} + \boldsymbol{h}(\boldsymbol{q}, \dot{\boldsymbol{q}}) = \boldsymbol{D}(\boldsymbol{\tau} - \boldsymbol{\tau}_f) + \boldsymbol{J}_e^T \boldsymbol{F}_e, \tag{3.5}$$

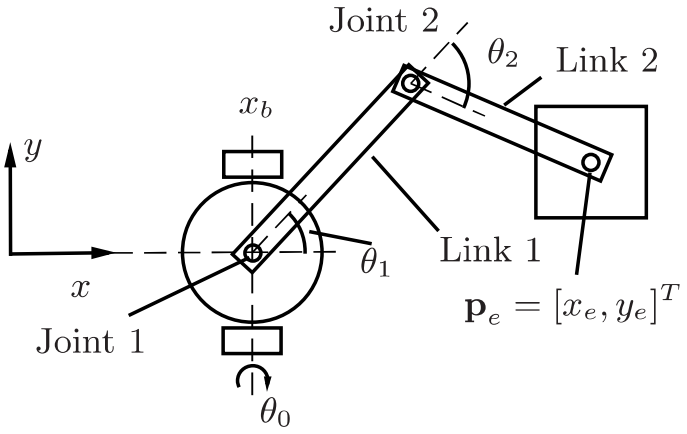

Figure 3.9: Schematic model of a two-link mobile manipulator with a heavy object

where $\boldsymbol{D} = \mathrm{diag}\{1/R, 1, 1\}$. The kinetic energy of the system is expressed by using $\boldsymbol{M}(\boldsymbol{q})$ as

$$E = (1/2)\dot{\boldsymbol{q}}^T \boldsymbol{M}(\boldsymbol{q})\dot{\boldsymbol{q}}. \tag{3.6}$$

Then, the term $\boldsymbol{h}(\boldsymbol{q}, \dot{\boldsymbol{q}})$ is expressed as $\boldsymbol{h} = \dot{\boldsymbol{M}}(\boldsymbol{q})\dot{\boldsymbol{q}} - (\partial E/\partial \boldsymbol{q})^T$. The friction force between the object and the ground is denoted as $\boldsymbol{F}_e$ in (3.5). When the object is at rest, the static friction force $\boldsymbol{F}_s$ is applied to the object, that is, $\boldsymbol{F}_e = \boldsymbol{F}_s$. It is supposed to satisfy $\|\boldsymbol{F}_s\| \leq \mu_s m_o \|\boldsymbol{g}\|$ where μ_s is the static friction coefficient and $\boldsymbol{g}$ is the gravitational acceleration vector. When the object slides on the ground, $\boldsymbol{F}_e = \boldsymbol{F}_k$ where $\boldsymbol{F}_k$ is the kinetic friction force defined as

$$\boldsymbol{F}_k = (-a\dot{\boldsymbol{p}}_e - b\,\mathrm{sgn}(\dot{\boldsymbol{p}}_e))m_o\|\boldsymbol{g}\|. \tag{3.7}$$

The friction torques at the wheels and the joints are denoted as $\boldsymbol{\tau}_f = [\tau_{f0}, \tau_{f1}, \tau_{f2}]^T$ in (3.5). From the assumption 5, $\tau_{fi} = 0$ $(i = 1, 2)$ and τ_{f0} is represented as

$$\tau_{f0} = c\dot{\theta}_0. \tag{3.8}$$

The equations of motion only for the object can be represented as

$$m_o\ddot{\boldsymbol{p}}_e = \boldsymbol{F}_a + \boldsymbol{F}_e, \tag{3.9}$$

where the force at the object from the robot manipulator is expressed as $\boldsymbol{F}_a = [F_{ax}, F_{ay}]^T$.

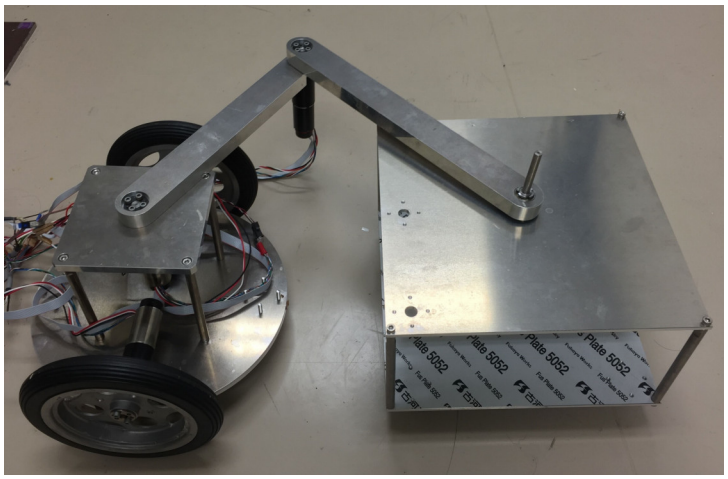

Figure 3.10: Experimental prototype

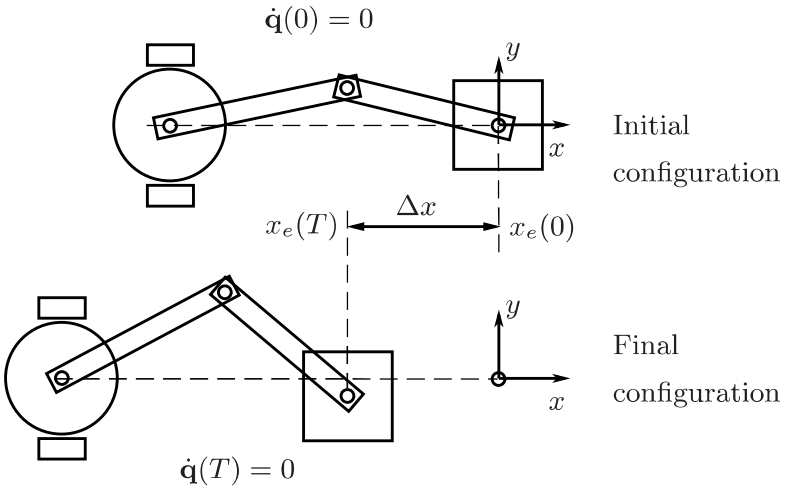

Figure 3.11: Task of dragging a heavy object

3.4.2 Problem formulation

This subsection deals with the problem of dragging a heavy object a certain distance along x-axis by the mobile manipulator as shown in Fig. 3.11. The remainder of this section focuses on the case where the masses of the base and the object are much larger than the mass and inertia of the robot manipulator.

To save the energy consumption of the mobile manipulator, the torques necessary to drag the heavy object should be reduced. The motion planning problem where the torques at the wheels and the joints are minimized is considered under the following boundary conditions at the start time, $t = 0$, and the end time, $t = T$:

$$\dot{\boldsymbol{q}}(0) = \dot{\boldsymbol{q}}(T) = \boldsymbol{0},\ x_e(0) = y_e(0) = 0,\ x_e(T) = \Delta x, \tag{3.10}$$

where Δx is a specified displacement of the object along the x-axis. From (3.10), the initial posture of the manipulator $\boldsymbol{q}(0)$ is obtained if $\theta_1(0)$ is given.

The following cost function is chosen as criterion for optimization

$$J_C(\xi) = \int_0^T \|\boldsymbol{\tau}\|^2 dt = \int_0^T (\tau_0^2 + \tau_1^2 + \tau_2^2) dt, \tag{3.11}$$

where ξ represents the parameters for optimization and is chosen as $\xi = \{\theta_1(0),\ \tau_0(t),\ \tau_1(t),\ \tau_2(t)\}$ $(0 \le t \le T)$. The initial posture can be chosen as $\theta_1(0) \ge 0$ due to the symmetry of the problem with respect to the x-axis. The torques at the wheels and the robot manipulator joints, $\tau_0(t)$, $\tau_1(t)$ and $\tau_2(t)$, are approximately represented by using cubic B-spline functions. Then, the parameters for optimization are reduced to

$$\phi = \{\theta_1(0), \{p_{i,j}\}\}\ \ (i = 0,1,2,\ j = 1,\cdots,m), \tag{3.12}$$

where $\{p_{i,j}\}$ are the control points of B-spline function for $\tau_i(t)$, and m is the number of control points for each B-spline function.

3.4.3 Numerical results

The optimal motion of the mobile manipulator was searched for by numerical optimization. The Matlab function, fmincon, was used to find the optimal values of ϕ and J_C. The parameters in Table 3.3 are used as the physical ones of the mobile manipulator. The other physical parameters are set to be $T = 2$[s], $\Delta x = -0.5$[m], $a = 0.2$[s/m], $b = 0.2$, $\mu_s = 0.4$ and $c = 0.3$[Nms/rad].

In the task in Section 3.4.2, the force to pull the object is caused by the driving torque at the

wheels, the joint torques of the robot manipulator and the inertial effects in the motion of the mobile manipulator. In order to examine how the joint torques and the inertial effects of the robot manipulator motion affect the cost J_C, the numerical optimization was performed in two cases, Case A and Case B. In Case A, all the parameters of ϕ are optimized by the numerical optimization. In Case B, there exist some constraints that $\theta_1(0) = 0$ and $\tau_1(t) = \tau_2(t) = 0$, that is, the robot manipulator is fully extended parallel to x-axis during the task and the object is to be moved only by the wheel torque $\tau_0(t)$. Therefore, the parameters for optimization in Case B are reduced to $\phi = \{p_{0,j}\}$.

Table 3.2: Physical parameters of the two-link mobile manipulator

l_1	0.3 [m]	l_2	0.35 [m]
l_{g1}	0.138 [m]	l_{g2}	0.179 [m]
I_1	0.121 [kgm^2]	I_2	0.118 [kgm^2]
m_1	0.8 [kg]	m_2	0.52 [kg]
m_b	3.4 [kg]	m_o	5 [kg]

Case A

The motion obtained by numerical optimization is shown in Fig. 3.12, where the postures of the robot are drawn at every $T/5$[s]. The time histories of input torques and joint velocities of the robot manipulator are shown in Figs. 3.13 and 3.14 respectively. The red dashed lines in these figures represent the moment $t = 1.192$[s], when the robot manipulator is at the exact singular configuration. Fig. 3.15 shows the time histories of kinetic energies of the mobile base, the two-link robot manipulator and the object. The value of J_C for the obtained motion is 8.6[N^{2}m^{2}s].

The features b), c) and d) are utilized in Case A. From Figs. 3.14 and 3.15, the joint velocities and the kinetic energy of the robot manipulator reach their peak values around $t = 1.21$[s]. The object starts to move a little before that time due to the force F_{ax} shown in Fig. 3.16, which corresponds to the feature c). After the robot manipulator passes through the singular configuration, the kinetic energy of the robot manipulator decreases while the one of the object increases intensely, which means that energy flows from the robot manipulator into the object as shown in Fig. 3.15. Moreover, the total energy also increases quickly when the robot manipulator gets close to the singular configuration due to the feature b). Joint torques also cause a large force just after passing through the singular configuration due to the feature d).

Case B

The motion obtained by numerical optimization is shown in Fig. 3.17, where the postures

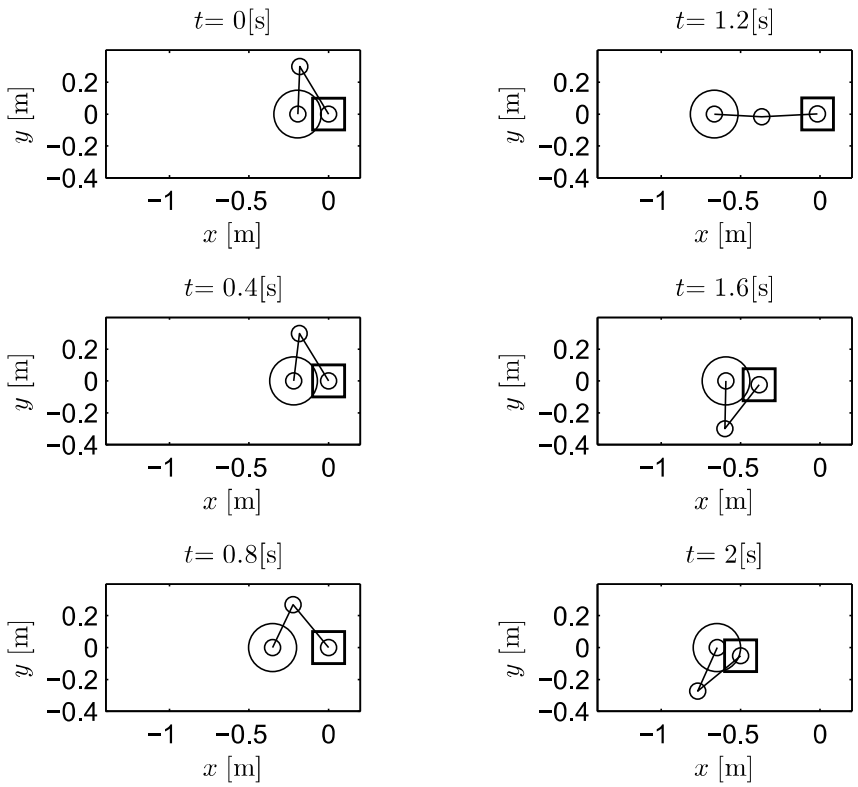

Figure 3.12: Optimized motion of the mobile manipulator(Case A)

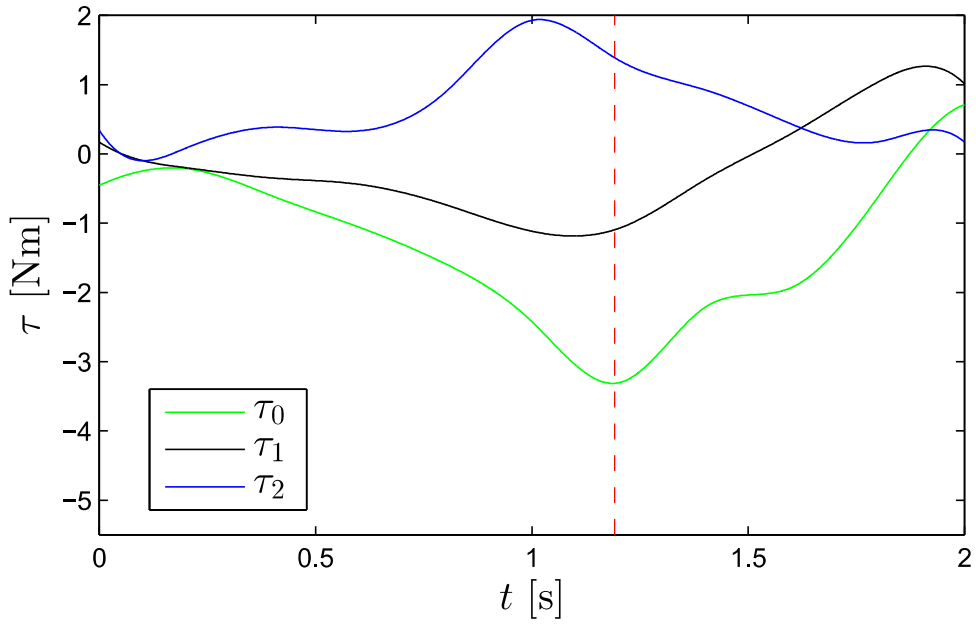

Figure 3.13: Time histories of input torques(Case A)

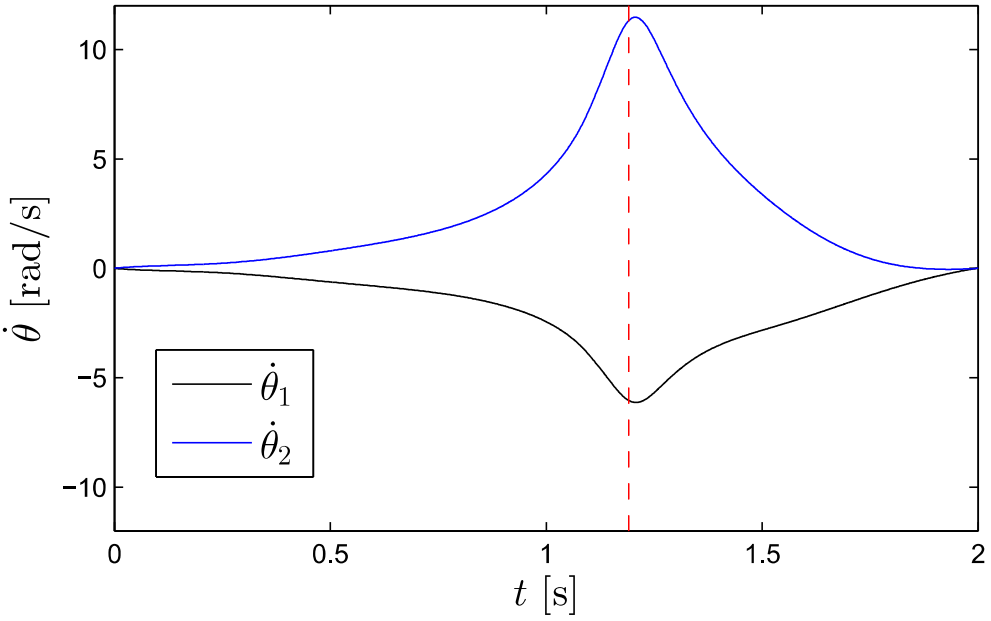

Figure 3.14: Time histories of joint angular velocities(Case A)

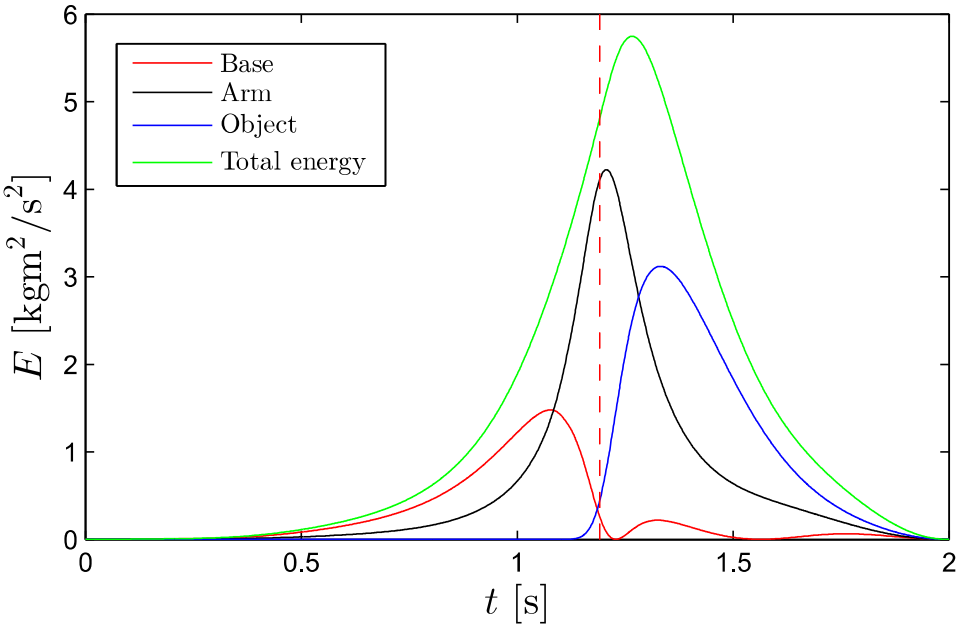

Figure 3.15: Time histories of kinetic energies(Case A)

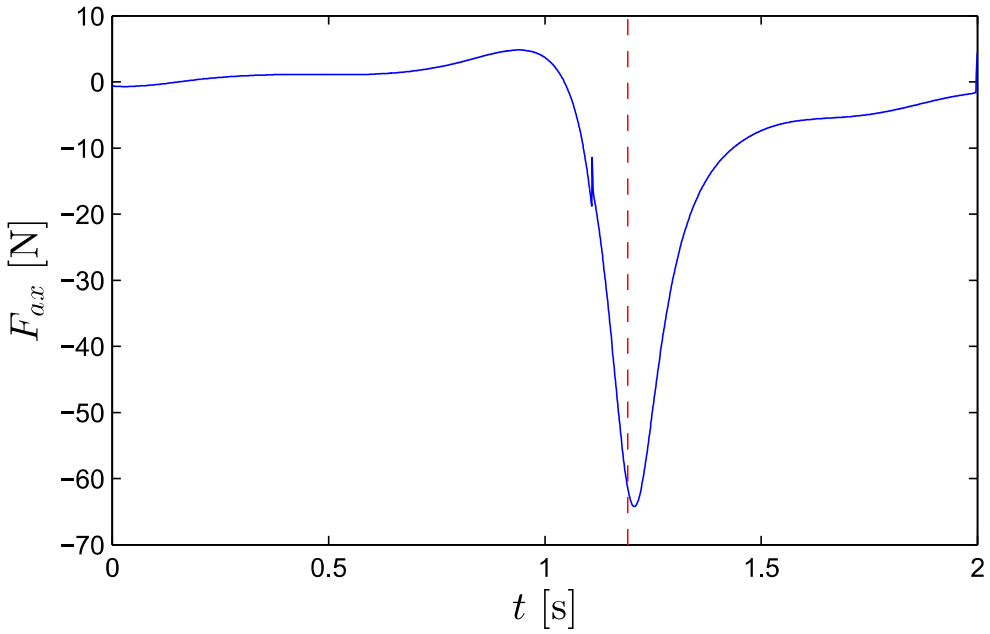

Figure 3.16: Time history of the force acting on the object from the mobile manipulator(Case A)

of the robot are drawn at every $T/5$[s]. The time history of the wheel torque τ_0 is shown in Fig. 3.18. The mobile manipulator and the object are at rest until the static friction force reaches its maximum value around the time $t = 0.7$[s], due to the increase of τ_0. The red dashed line expresses the moment when the object starts to move. The wheel torque does not generate the kinetic energy till that time, while the total energy has been stored before the object starts to move in Case A. The value of J_C for the obtained motion is $14.52[\mathrm{N^2m^2s}]$. None of the features b), c) and d) is utilized in Case B, since $\tau_1(t) = \tau_2(t) = 0$ and $\dot{\theta}_1(t) = \dot{\theta}_2(t) = 0$. Because $\theta_1(t) = \theta_2(t) = 0$, the arm keeps its configuration as the singular one. The force acted on the heavy object can be directly caused by the wheel torque, and the robot configuration is kept without any joint torques, which corresponds to the feature a).

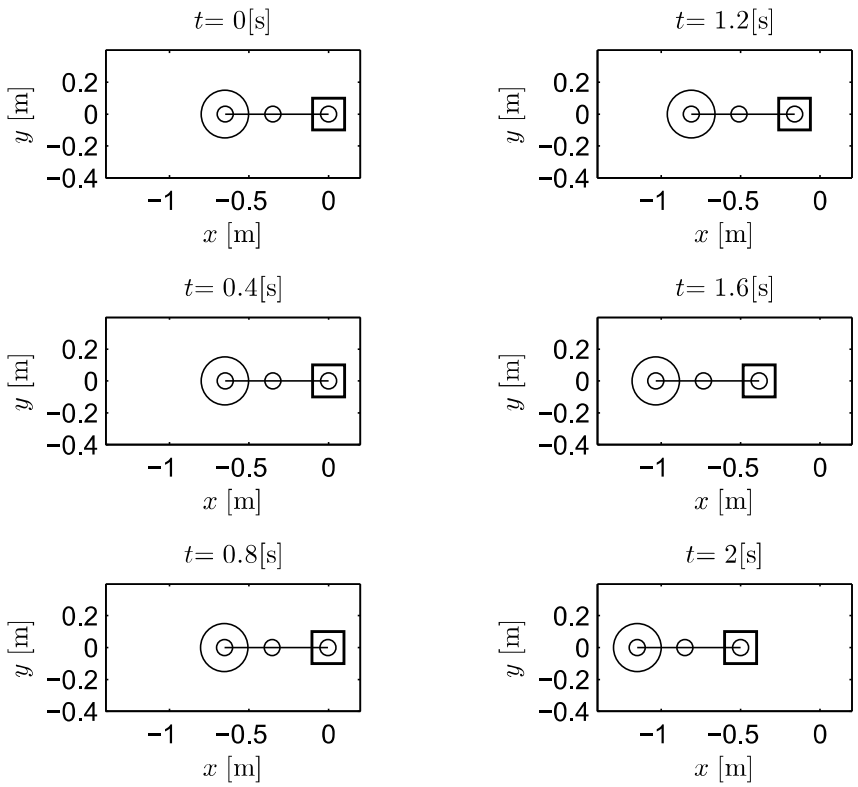

Figure 3.17: Optimized motion of the mobile manipulator(Case B)

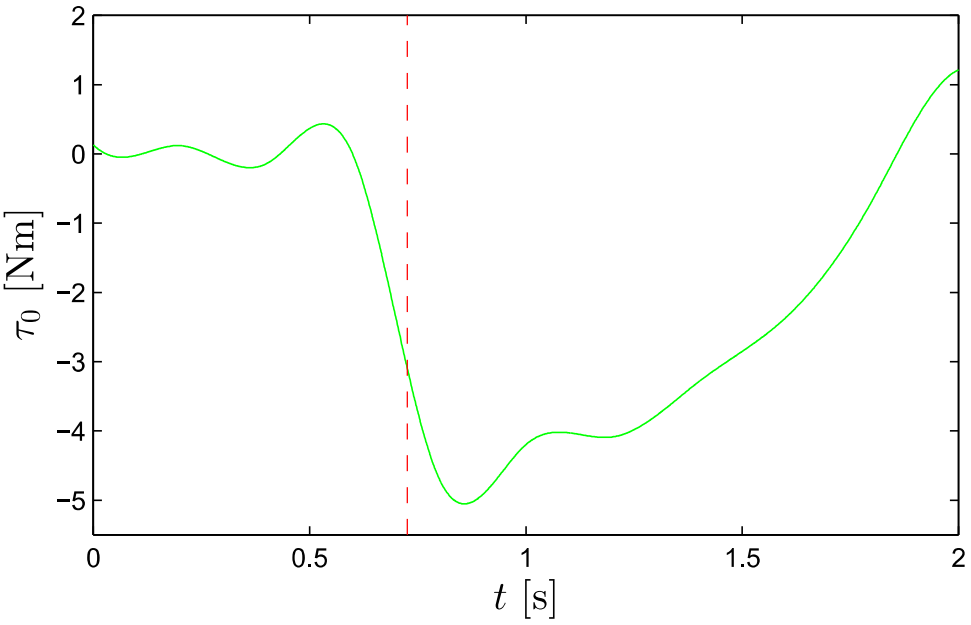

Figure 3.18: Time history of input torque τ_0 (Case B)

3.4.4 Pulling force with a simplified model

The numerical results in Section 3.4.3 show that the force F_{ax} and the total energy E reach their peak values when the robot manipulator is near the singular configuration. To explain the results from a theoretical point of view, this subsection analyzes the dynamics of the mobile manipulator by simplifying the model in Section 3.4.2, under the following assumptions as shown in Fig. 3.19:

6. The length of Link 1 is equal to the one of Link 2, that is,

$$l_1 = l_2 = l \ . \tag{3.13}$$

7. The coefficient of static friction μ_s is large enough to prevent the object from being dragged, that is,

$$\boldsymbol{p}_e(t) \equiv 0 \ . \tag{3.14}$$

8. The mass of the base is much larger than the mass and inertia of the robot manipulator.

9. The input torques $\boldsymbol{\tau}$ are bounded and $O(1)$, and the friction torque τ_{f0} is set to be zero.

From (3.13) and (3.14), it can be easily obtained that

$$\theta_2 = -2\theta_1, \ x_b = -2l\mathrm{c}\theta_1 \ . \tag{3.15}$$

Therefore, the degrees of freedom of the mobile manipulator are reduced from three to one. The angle θ_1 at Joint 1 is chosen as the generalized coordinate for the simplified model. From (3.9) and (3.14), it can also be obtained that

$$\boldsymbol{F}_a = -\boldsymbol{F}_e \ . \tag{3.16}$$

Substituting (3.15) and (3.16) into (3.5), the equations of motion are rewritten as

$$\begin{bmatrix} \ddot{\theta}_1 \\ F_{ax} \\ F_{ay} \end{bmatrix} = \boldsymbol{A}^{-1} \left\{ \begin{bmatrix} \tau_0/R \\ \tau_1 \\ \tau_2 \end{bmatrix} - \hat{\boldsymbol{h}} \right\} , \tag{3.17}$$

$$\boldsymbol{A} = \begin{bmatrix} \alpha_1 \mathrm{s}\theta_1 & 1 & 0 \\ \alpha_2(\mathrm{s}\theta_1)^2 + \beta_2 & 0 & 2l\mathrm{c}\theta_1 \\ \beta_3 & l\mathrm{s}\theta_1 & l\mathrm{c}\theta_1 \end{bmatrix} , \tag{3.18}$$

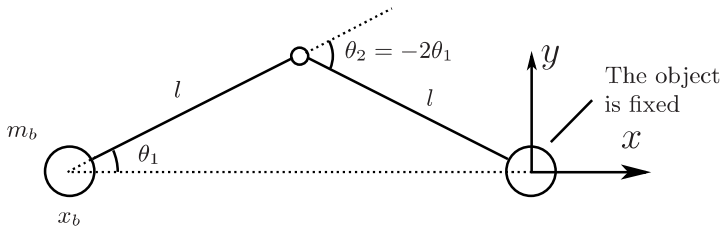

Figure 3.19: Simplified model of the mobile manipulator

$$\hat{\boldsymbol{h}} = [\alpha_1 \mathrm{c}\theta_1 \dot{\theta}_1^2, \alpha_2 \mathrm{s}\theta_1 \mathrm{c}\theta_1 \dot{\theta}_1^2, 0]^T \ , \tag{3.19}$$

where $\alpha_1 = 2\hat{m}_b l + m_1(2l - l_{g1}) + m_2(l - l_{g2})$, $\alpha_2 = 2l(-m_1 l_{g1} - m_2(l - l_{g2}))$, $\beta_2 = I_1 - I_2 + m_1 l_{g1}^2 + m_2(l^2 - l_{g2}^2)$, $\beta_3 = -I_2 + m_2 l_{g2}(l - l_{g2})$ and $\hat{m}_b = m_b + 2I_w/R^2$. From the assumption 8, it should be noted that $\alpha_1 = O(\hat{m}_b) \gg |\alpha_2|, |\beta_2|, |\beta_3|$. The total energy E is also expressed by using only θ_1 and $\dot{\theta}_1$. Substituting (3.15) into (3.6), E is rewritten as

$$E = K(s)\dot{\theta}_1^2/2 \ , \tag{3.20}$$

where $K(s) = (2\alpha_1 l + \alpha_2)s^2 + \beta_2 - 2\beta_3$ and the variable s is defined as $s = \mathrm{s}\theta_1$.

This subsection focuses on a similar dynamic behavior to the one in Case A. The robot manipulator passes through the singular posture (b) from posture (a) to posture (c) as shown in Fig. 3.20, where $t_a < t_b < t_c$. The variations of E and F_{ax} will be investigated under the following assumption:

10. $\dot{\theta}_1 \leq 0$ and $-\pi/2 \leq \theta_1 \leq \pi/2$.

The first row of (3.17) can be rewritten by using E as follows:

$$\dot{E} = (2ls\dot{\theta}_1)(\tau_0/R) + \dot{\theta}_1(\tau_1 - 2\tau_2) = e_1(s)\sqrt{E}(\tau_0/R) + e_2(s)\sqrt{E}(\tau_1 - 2\tau_2) \ , \tag{3.21}$$

where

$$e_1(s) = -2ls\sqrt{2/K(s)} \ , e_2(s) = -\sqrt{2/K(s)} \ . \tag{3.22}$$

The energy supply rates from the wheel torque τ_0 and the joint torques (τ_1, τ_2) are determined by the functions $e_1(s)$ and $e_2(s)$. Noting that $K(0) = \beta_2 - 2\beta_3 = O(1)$ and $K(1) = K(-1) \approx 2\alpha_1 l \approx 4\hat{m}_b l^2 = O(\hat{m}_b)$, the behavior of the functions can be easily analyzed. The function $e_1(s)$ is odd, and $|e_1(s)|$ monotonically increases from $|e_1(0)| = 0$ to $|e_1(1)| = |e_1(-1)|$

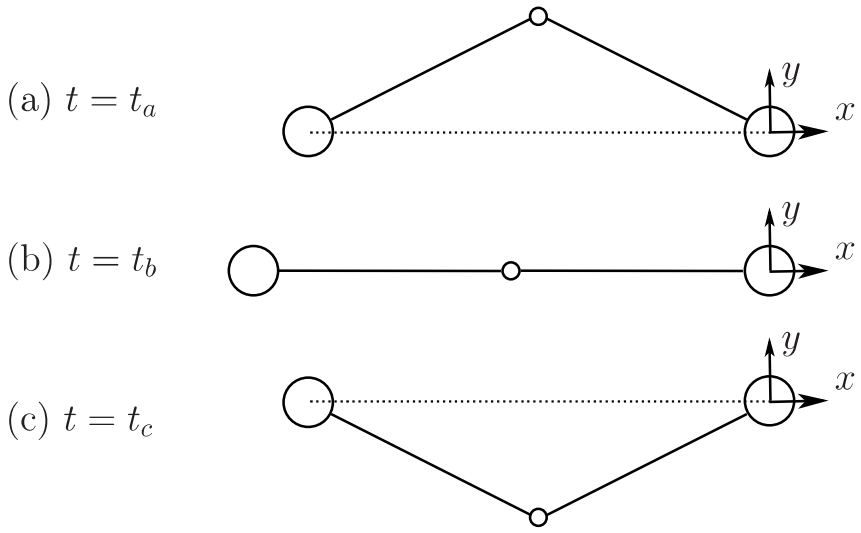

Figure 3.20: Postures (a), (b) and (c) of the simplified model

$= O(1/\sqrt{\hat{m}_b})$ as s approaches ± 1. On the other hand, $e_2(s)$ is even, and has a large peak at $s = 0$, that is, at the singular configuration. The absolute value at the peak is $|e_2(0)| = \sqrt{2/K(0)} = O(1)$, and $|e_2(s)|$ monotonically decreases to $|e_2(1)| = |e_2(-1)| = O(1/\sqrt{\hat{m}_b})$ as s approaches ± 1 from 0.

The profile of $\dot{E}$ as the function of s is drawn in Fig. 3.21, where the physical parameters of the simplified model are given in Table 3.3. According to the pulling motion shown in Fig. 3.20, the joint torques and kinetic energy are set to be $\tau_0 = -1$[Nm], $\tau_1 = -1$[Nm], $\tau_2 = 2$[Nm] and $E = 1$[kgm^2/s^2]. In order to maximize $|\tau_1 - 2\tau_2|/\sqrt{\tau_1^2 + \tau_2^2}$, τ_1 and τ_2 should satisfy $\tau_2 = -2\tau_1$. From Fig. 3.21, it should be noted that a large energy supply $\dot{E}$ can be caused by $(\tau_1 - 2\tau_2)$ near $s = 0$.

Table 3.3: Physical parameters of the simplified model

l	0.3 [m]	m_b	10 [kg]
l_{g1}	0.15 [m]	l_{g2}	0.15 [m]
I_1	0.01 [kgm^2]	I_2	0.01 [kgm^2]
m_1	1 [kg]	m_2	1 [kg]
R	0.15 [m]		

The second row of (3.17) can be rewritten by using (3.20) as

$$F_{ax} = f_1(s)(\tau_0/R) + f_2(s)(\tau_1 - 2\tau_2) + f_3(s)E \ , \tag{3.23}$$

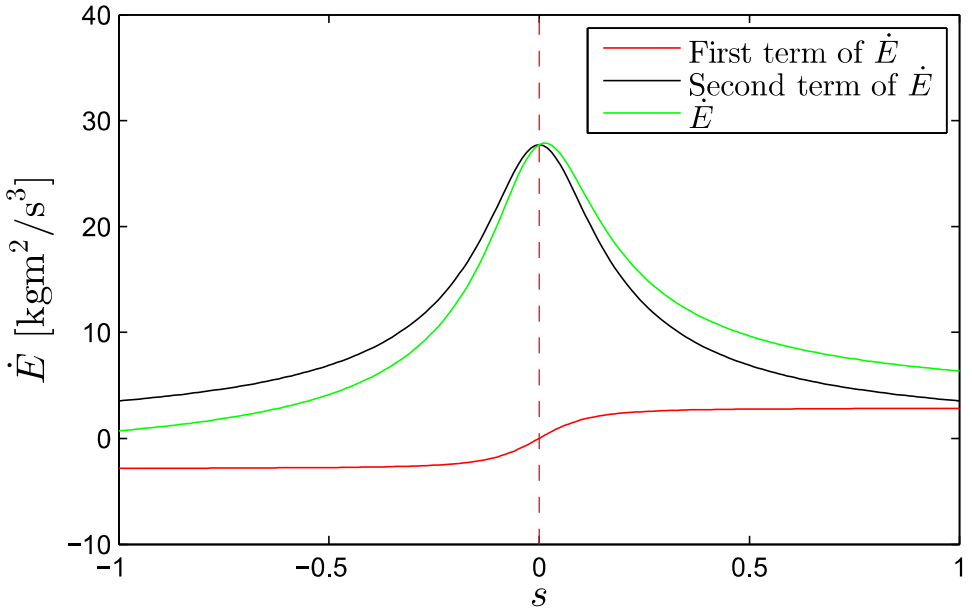

Figure 3.21: Variation of energy supply $\dot{E}$ with respect to s

where

$$f_1(s) = (\alpha_2 s^2 + \beta_2 - 2\beta_3)/K(s),\ f_2(s) = -\alpha_1 s/K(s),$$

$$f_3(s) = -2\alpha_1(\beta_2 - 2\beta_3)\sqrt{1-s^2}/(K(s))^2\ . \tag{3.24}$$

The torques τ_0 and $(\tau_1 - 2\tau_2)$ are transmitted directly to the object as the first and second terms of the right-hand side of (3.23). The third term expresses the force caused by the inertial effects of the motion, and the magnitude of the term depends on the energy E. The behavior of the functions, $f_1(s)$, $f_2(s)$ and $f_3(s)$, can also be easily analyzed. The function $f_1(s)$ is even, and its maximum value is 1 at $s = 0$. The value of $f_1(s)$ monotonically decreases to $f_1(1) = f_1(-1) = O(1/\hat{m}_b)$ as s approaches ± 1 from 0. The function $f_2(s)$ is odd, and $f_2(0) = 0$. The absolute value of $f_2(s)$ has a peak at $s = \pm s^*$ where $s^* = \sqrt{(\beta_2 - 2\beta_3)/(2\alpha_1 l + \alpha_2)}$. The peak value is $f_2(s^*) = -f_2(-s^*) = O(\sqrt{\hat{m}_b})$. It should be noted that $s^* = O(1/\sqrt{\hat{m}_b}) \ll 1$. Although $|f_2(s)|$ is zero at the exact singular posture ($s = 0$), it intensely increases from zero and has the peak value at a posture close to the singular configuration ($s = s^*$). As s approaches ± 1 from $\pm s^*$, $|f_2(s)|$ monotonically decreases to $|f_2(1)| = |f_2(-1)| = O(1)$. The function $f_3(s)$ is even, and its peak value is $|f_3(0)| = 2\alpha_1/(\beta_2 - \beta_3) = O(\hat{m}_b)$. The absolute value $|f_3(s)|$ monotonically decreases to $|f_3(1)| = |f_3(-1)| = 0$ as s approaches ± 1.

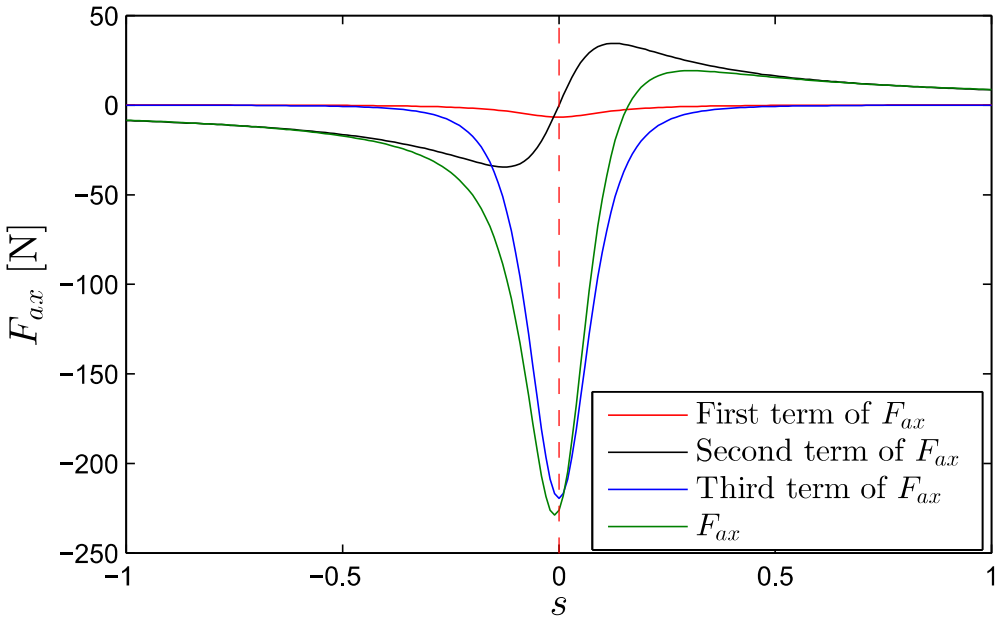

Figure 3.22: Variation of pulling force F_{ax} with respect to s

The profile of F_{ax} as the function of s is drawn in Fig. 3.22, where the same values for the physical parameters and the torques are used as in Fig. 3.21. From Fig. 3.22, it should be noted that a large pulling force $|F_{ax}|$ can be given from the energy E near $s = 0$.

From the above analysis, in the motion shown in Fig. 3.20, a large pulling force can be generated from relatively small amount of input torques. As the robot manipulator is extended from posture (a) to (b), the energy E can be efficiently generated by the second term of the right-hand side of (3.21), as shown in Fig. 3.21. The generated energy causes a large force $|F_{ax}|$ from the third term of the right-hand side of (3.23) near posture (b). As the posture turns from (b) to (c), $|F_{ax}|$ decreases intensely as shown in Fig. 3.22.

Similar behavior of E and F_{ax} can be found in Figs. 3.15 and 3.16 for Case A. The energy E increases intensely as the robot manipulator is getting close to the singular posture. The decrease in E after passing the singular posture would be caused by the friction between the object and the ground, because the object starts to move in Case A unlike in the above analysis. The behavior of F_{ax} in Fig. 3.16 corresponds to the one in Fig. 3.22, because s decreases as time advances in Case A. The difference between the amounts of F_{ax} in Figs. 3.16 and 3.22 could be caused from the differences of the physical parameters and the assumptions 6 and 7.

In Case B, the object is pulled only by the first term of the right-hand side of (3.23) at $s = 0$, and the joint torques (τ_1, τ_2) are not used. Although τ_1 and τ_2 are consumed to generate the energy E in Case A, the value of J_C for Case A is less than the one for Case B. It would

be because the pulling force obtained from the energy E is much larger than the one from τ_0 as shown in Fig. 3.22 near $s = 0$. The joint torques (τ_1, τ_2) necessary to generate E are also reduced in Case A by using the second term of (3.21).

3.4.5 Discussion

In [16, 74], a two-link robot manipulator starts its motion from the singular configuration similarly to Case B in Section 3.2. The pulling force caused by the feature c) is limited, because the energy of the robot manipulator that is used for the feature c) is generated only in a short time from the start. Similarly to Case A in Section 3.2, a mobile manipulator can also pull the object through the singular configuration in a horizontal plane. The mobile base can firstly move away from the object while the object stays at rest, and then the robot manipulator can start to pull the object after getting close to the singular configuration. The movement of the base and the joint rotations of the robot manipulator can increase the total energy at the singularity corresponding to the feature b). The larger energy near singular configuration for a mobile manipulator generates a large force as shown in Fig. 3.22, which corresponds to the feature c). The joint torques can also generate a large force after passing through the singular configuration due to the feature d). The numerical result in Case A is consistent with this theoretical result. A large amount of energy is stored before reaching the neighborhood of singular configuration as shown in Fig. 3.15, and a large force is simultaneously generated as shown in Fig. 3.16.

In the analysis in Section 3.4.4 where $l_1 = l_2$, the joint torques τ_1 and τ_2 should satisfy $\tau_2 = -2\tau_1$ in order to increase the energy supply rate $\dot{E}$ and generate a large force from the supplied E. Although the base can be moved and the object is fixed for the analysis in this chapter unlike in [16, 74] and in Chapter 2, a similar result about the ratio of τ_1 to τ_2 was obtained. Furthermore, the joint torques with respect to the robot manipulator are more suitable for generating energy near the singular configuration than the driving torque at the wheels. The analysis result about the force corresponds to the one related to end-effector acceleration in Chapter 2.

3.5 Conclusion

This chapter firstly exhibited some lifting motions of a two-link robot manipulator with fixed base. The features of singular configurations have shown the usefulness for minimizing the necessary joint torques. For the robots that can pass through the singular configurations, the feature c) can be utilized more efficiently. When the object needs to be lifted up in a weight

lifting motion, the robot passes through its singular configurations twice to accelerate the object.

In Section 3.4, it has been shown that the singular configuration of a mobile manipulator with unfixed base is advantageous in reducing the torques necessary for dragging a heavy object, which corresponds to the features b), c) and d). From the numerical and theoretical results, the energy of the mobile manipulator is supplied efficiently from the input torques near singular configuration, and the supplied energy causes a large force to pull the object.

Appendix 3.A Parameterization Methods for Optimization

In robotics, numerical optimization and optimal control algorithms have become more and more powerful in recent years [4, 76–79]. Generally, a cost function needs to be minimized over the system variables in an optimization problem. Direct methods for trajectory optimization are widely used for planning locally optimal trajectories of robotic systems. For instance, the trajectories of angles can be firstly parameterized by several kinds of functions. If the parameters for the joint angles are given once, the trajectories of joint torques can be obtained according to the equations of motion. The obtained system variables (including joint angles, joint velocities, joint torques etc.) lead to a certain value of the cost function. Thus, the optimal trajectory of the robot can be obtained by searching for the parameters that minimize the cost function. The joint torques or end-effector position can also be parameterized in a similar way as the joint angles. The parameterization methods used in this dissertation will be introduced.

3.A.1 Approximation by cubic B-spline functions

The B-splines of order k are piecewise C^{k-2} continuous polynomials of degree $k-1$. The joint torque τ_i can be expressed by using cubic B-spline with $k=4$:

$$\tau_i(t,P_i) = \sum_{j=1}^{m} B_{i,j,k} p_{i,j}, \tag{3.25}$$

where $B_{i,j,k}$ represents the basis function, and $P_i = \{p_{i,1}, \cdots, p_{i,m}\}$ expresses the control points. The basis function of order k is given by using a recursion formula:

$$B_{i,j,k}(t) = \frac{t-t_j}{t_{j+k-1}-t_j} B_{i,j,k-1}(t) + \frac{t_{j+k}-t}{t_{j+k}-t_{j+1}} B_{i,j+1,k-1}(t), \tag{3.26}$$

where $j = 1, \cdots, m$, $k \geq 2$, $t_1 \leq t_2 \leq \cdots \leq t_{m+k}$ and

$$B_{i,j,1}(t) = \begin{cases} 1 & \text{if } t_j \leq t < t_{j+1} \\ 0 & \text{otherwise} \end{cases}. \tag{3.27}$$

With the above approximation, the parameters to express the joint torques become $\{p_{i,j}\}$ $(i = 0,1,2,\ j = 1,\cdots,m)$. The joint angle can be represented by B-spline as the same as the joint torque.

3.A.2 Approximation by piecewise fifth order spline functions

The duration time of the robot is denoted as T, and the time interval $[0\ T]$ can be divide by n. The trajectory of joint angle θ in each time interval $[t_i\ t_{i+1}]$ ($i = 0, \ldots, n-1$ and $t_j = jT/n$ for $j = 0, \ldots, n$) is expressed by a fifth order polynomial function of time, φ_i, as follows:

$$\varphi_i(t) = a_i + b_i t + c_i t^2 + d_i t^3 + e_i t^4 + f_i t^5, \tag{3.28}$$

where a_i, b_i, c_i, d_i, e_i and f_i are scalar parameters. To make the input torque τ continuous, the functions $\varphi_i(t)$ that satisfy $\varphi_i(t_{i+1}) = \varphi_i(t_{i+1})$, $\dot{\varphi}_i(t_{i+1}) = \dot{\varphi}_i(t_{i+1})$ and $\ddot{\varphi}_i(t_{i+1}) = \ddot{\varphi}_i(t_{i+1})$ are chosen for $i = 0, \cdots, n-2$. When the polynomials satisfy those conditions, independent parameters to express θ are reduced to $\{a_0, \ldots, a_{n+1}, e_0, f_0, \ldots, e_{n-1}, f_{n-1}\}$.

Chapter 4

Jumping and Landing Motions of Legged Robots

4.1 Introduction

For a vertical jumping motion of legged robot, the features of singular configurations might be useful before or/and after taking-off. Similarly, the dynamic advantages of singular configurations might be exploited for the landing motion of a legged robot, and the impact when the foot contacts with the ground needs to be taken into consideration. The initial configuration near singular configurations may be expected to be advantageous in absorbing the kinetic energy with small joint torques to stop the landing motion. In order to clarify the advantages, the dynamics around the impact near singular configurations has to be examined.

This chapter deals with the jumping and landing motions of legged robots. In Section 4.2, the vertical jumping motion that minimizes the necessary joint torques for a two-link legged robot will be obtained, and the usefulness of the features of singular configurations in the stance phase will be verified. Section 4.3 extends the verification to the jumping motions for a four-link legged robot in stance phase and in aerial phase. The interaction force between the foot and the ground is calculated from the continuous model in a similar way as in [31] for the numerical optimization.

In Section 4.4, not only reduction of impact force but also minimization of joint torques for a landing motion of a four-link legged robot are considered. To the best of our knowledge, the problem of optimizing them simultaneously during landing has not been dealt with in the literature. The landing motion that minimizes the peak value of the impact force and the necessary joint torques is obtained by numerical optimization. The cost function is composed of the weighted sum of the one for the impact force and the one for the joint torques. Using

the joint model proposed in [32], it is assumed that the joint torques are represented by the parameters in the stiffness and damping coefficients. Numerical optimization results show that, as the weight of the cost function for the joint torques increases, the optimal configuration of the robot at the impact time becomes close to the singular configuration. To verify and understand the results, a theoretical analysis of the dynamics around the impact is performed with a simple model of the legged robot where the discontinuous model of impact is used. The theoretical analysis provides new insight into landing motion; when the impact configuration is close to, but not exactly, the singular configuration, the joint velocity immediately after the impact has the maximum value, and the kinetic energy of the robot can be absorbed by small joint torques.

4.2 Jumping Motion of a Two-link Legged Robot

4.2.1 Problem formulation

Optimal jumping motions of a two-link legged robot will be obtained, and the motion by the take-off time when the foot leaves the ground will be considered. The model of the robot is shown in Fig. 4.1. The robot is composed of two links, link 1, link 2 and a heavy body. The mass, length and moment of inertia of link i are denoted as m_i, l_i and I_i $(i = 1,2)$. The angles and joint torques at joint i are expressed as θ_i and τ_i $(i = 1,2)$. The mass of the body and the distance from joint i to the center of mass for link i are denoted as m_b and l_{gi}. The mass center of the body is considered to be located at joint 1 and its position is called (x_b, y_b).

The robot is supposed to jump from rest until the desired vertical velocity of the mass center is achieved and the vertical ground reaction force becomes zero. Several constraint conditions are considered as follows:

i The horizontal position of the mass center of the robot should be just above the foot (the end point of link 2) at the start time.

ii The angular velocities at all joints are set to be zero at the start time.

iii The vertical velocity of the body $\dot{y}_b(T)$ at the take-off time is set to be $v > 0$.

iV At the take-off time, the vertical ground reaction force $F_{gy}(T)$ equals zero.

The same cost function as in (3.2) is also used except that ξ includes initial angle θ_1, which can expresses the initial posture of the robot from assumption i.

The legged robot pushes the ground with the foot, and is pushed back by the ground reaction force. When the foot contacts with the ground, the ground reaction force $\boldsymbol{F}_g$ is considered

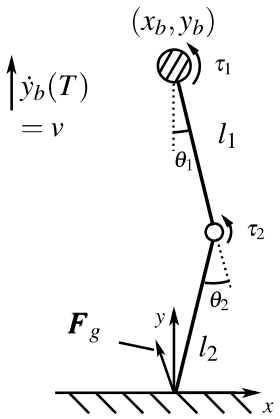

Figure 4.1: The model of two-link legged robot

as a constraint one, and can be directly derived from the equations of motion. In a similar way for the acceleration a_y in Section 2.5, its vertical component F_{gy} can be divided into three terms, torque-dependent force F_{gyt}, gravity-dependent force F_{gyg} and velocity-dependent force F_{gyv}, respectively. Roughly speaking, F_{gyt}, F_{gyg} and F_{gyv} correspond to a_{ty}, a_{gy} and a_{vy} respectively, and their variations with respect to the configurations are also similar to the ones for the accelerations.

4.2.2 Numerical simulation

The physical parameters of the two-link legged robot are given in Table 4.1. The desired upward velocity v is set to be 2[m/s]. MATLAB function fmincon is used to obtain the optimal parameters. To verify that the features a) and d) are very useful in the jumping motion of approaching the singular configuration, the numerical optimization was performed in two cases, Case A and Case B. In Case B, there is a condition on y_b at the take-off time, $y_b(T) \leq 0.5$[m]. Under the condition, the robot configuration is always far from the singular one in Case B.

Table 4.1: Physical parameters of the two-link legged robot

l_1	0.3 [m]	l_2	0.3 [m]
l_{g1}	0.15 [m]	l_{g2}	0.15 [m]
I_1	1×10^{-3} [kgm^2]	I_2	1×10^{-3} [kgm^2]
m_1	0.1 [kg]	m_2	0.1 [kg]
m_b	10 [kg]		

Case A

Fig. 4.2 shows the initial and final postures of the robot. The final posture is very close to

the singular configuration that the leg is stretched out. The time histories of joint torques are shown in Fig. 4.3. Fig. 4.4 shows the time histories of the vertical ground reaction force, F_{gy}, and three components of the force, F_{gyt}, F_{gyg} and F_{gyv}. Around the end time, the joint torques intensely increase, while the vertical ground reaction force reaches its peak value just before taking off. From then on, the force intensely decreases to zero. For the obtained jumping motion, $J_C = 76.2[\mathrm{N^2m^2s}]$. The duration time is obtained as $T = 0.098[\mathrm{s}]$.

Case B

Fig. 4.5 shows the initial and final postures of the robot. The time histories of joint torques are shown in Fig. 4.6. Fig. 4.7 shows the time histories of the vertical ground reaction force, F_{gy}, and three components of the force, F_{gyt}, F_{gyg} and F_{gyv}. For the obtained jumping motion, $J_C = 302.5[\mathrm{N^2m^2s}]$. The duration time is obtained as $T = 0.114[\mathrm{s}]$.

At the time interval $t \in [0, 0.09][\mathrm{s}]$, the joint torques in Case B are much larger than the ones in Case A. The peak value of vertical ground reaction force F_{gy} is much smaller than the one in Case A. The force F_{gyt} approximates F_{gy}, while the forces F_{gyg} and F_{gyv} can be ignored.

The features a) and d) of singular configurations are used in Case A. When $y_b = 0.6[\mathrm{m}]$, the robot is in a singular configuration where the links are aligned in a straight line. From Fig. 4.2, the initial posture is not far from it, and the body moves upward as the joints rotates rapidly. When the desired upward velocity v is given, the necessary joint velocities at the take-off time will become infinitely large if the robot is in the singular configuration. Thus, the final posture can be very close to, but not exactly, the singular configuration that the leg is stretched out as shown in Fig. 4.2. As observed in Figs. 4.3 and 4.6, the joint torques to overcome the gravity around the start time in Case A are much smaller than the ones in Case B due to the feature a). Around the end time, the joint torques intensely increase in Case A. From Figs. 4.4 and 4.7, the peak value of the ground reaction force in Case A is much larger than the one in Case B due to the feature d), even though the corresponding joint torques in Case A are smaller than in Case B. It should be noted that the joint torques around the end time in Case A satisfy (2.58) to use the feature d). The value of J_C in Case B is much larger than the one in Case A.

The numerical simulation results show that the singular configuration is advantageous in reducing joint torques in vertical jumping motion of a two-link legged robot. It will be shown later that the merit of singular configurations is also applicable to a four-link legged robot.

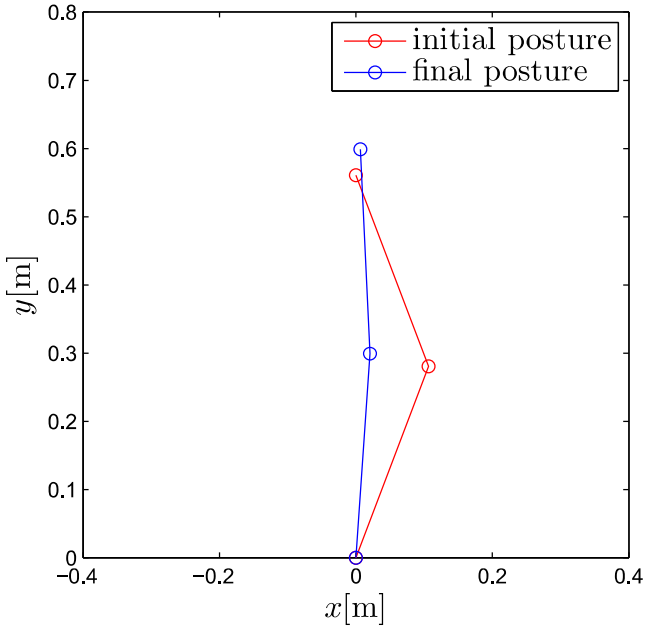

Figure 4.2: The initial and take-off postures of the robot for the optimized jumping motion(Case A)

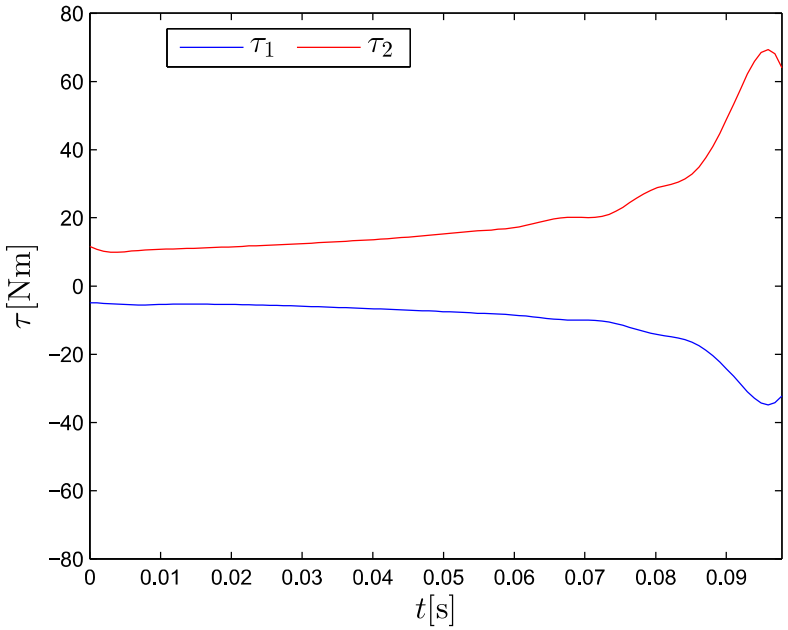

Figure 4.3: Time histories of joint torques(Case A)

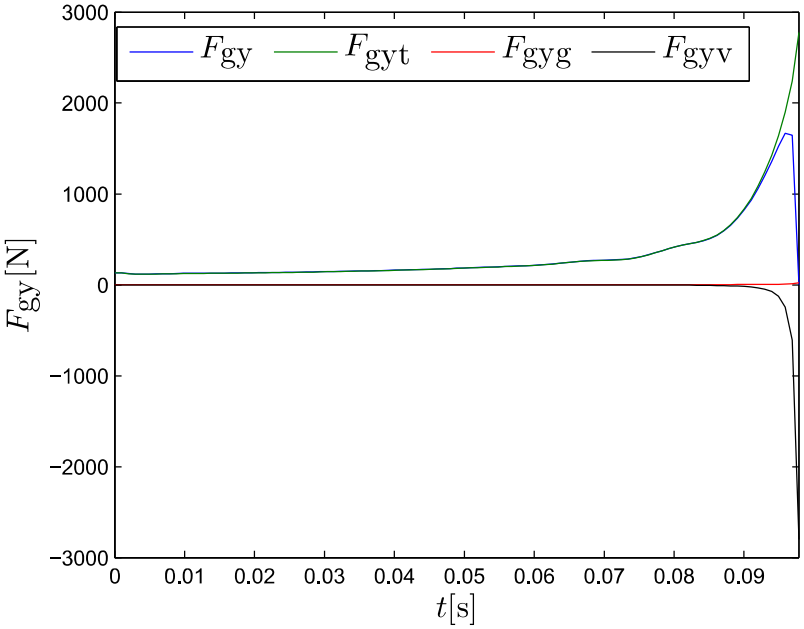

Figure 4.4: Time histories of vertical ground reaction forces(Case A)

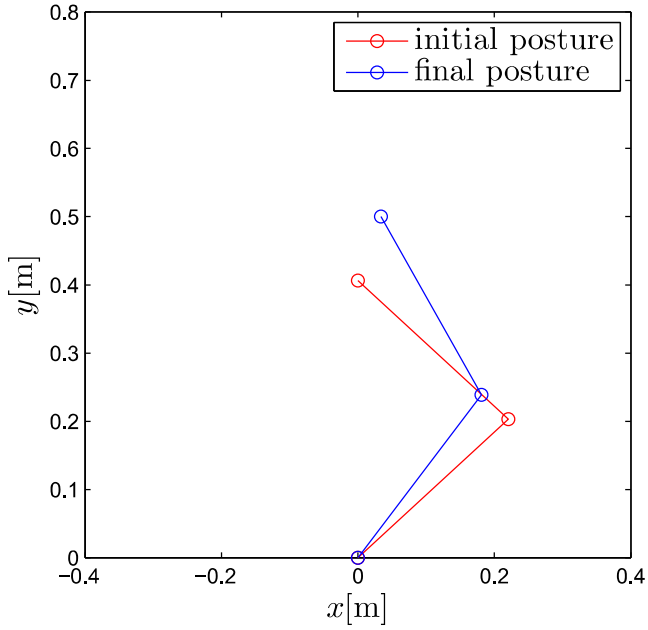

Figure 4.5: The initial and take-off postures of the robot for the optimized jumping motion(Case B)

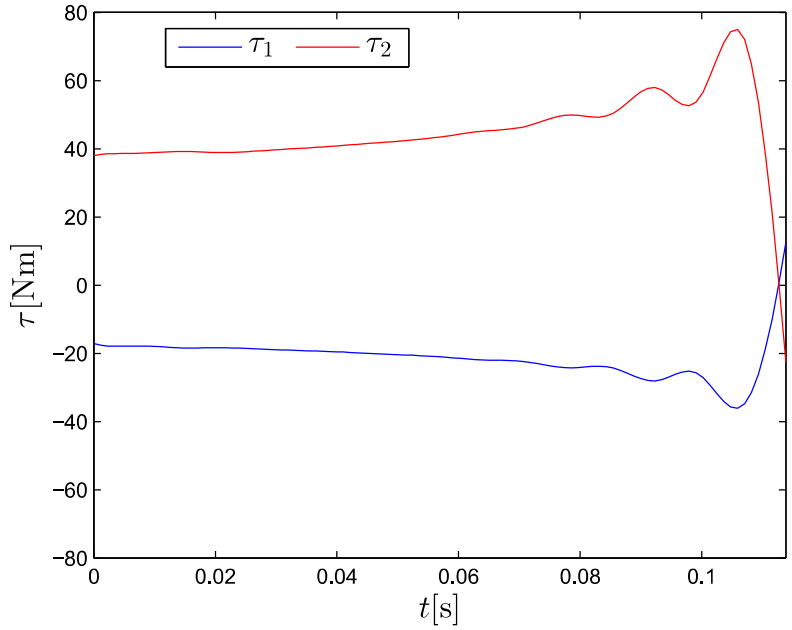

Figure 4.6: Time histories of joint torques(Case B)

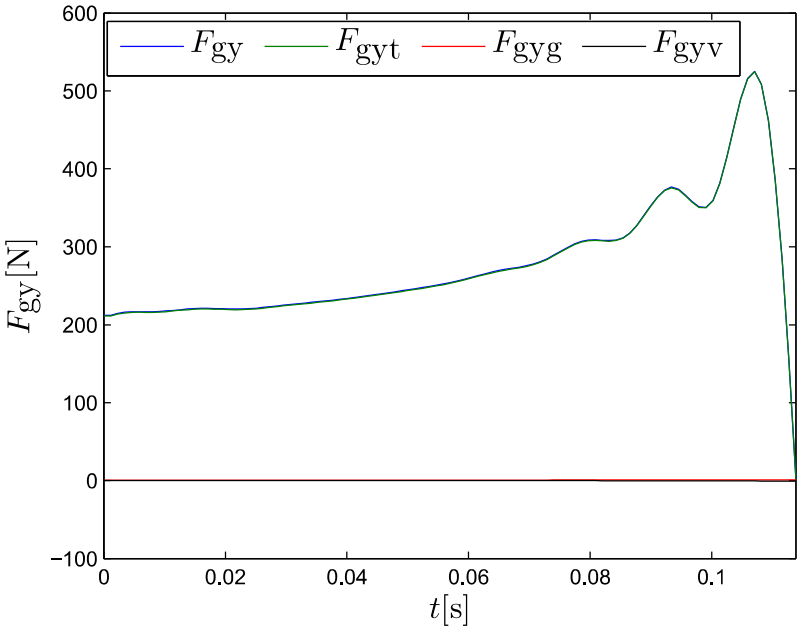

Figure 4.7: Time histories of vertical ground reaction forces(Case B)

4.3 Jumping Motion of a Four-link Legged Robot

The model of a four-link legged robot composed of one leg and a heavy body can be considered as a simplified one of human beings. By supposing that the foot is very light and the shape of the heavy body is ignored, the four-link model can be reduced to a two-link one. To obtain a natural jumping motion like human beings, it is required to consider the rotation and the non-vertical movement of the body, and simultaneously deal with both the motion in stance phase and the motion in aerial phase where the foot is in the air after take-off.

In this section, vertical jumping motions of a one-legged planar robot (Fig. 4.8) will be considered. The robot consists of four links, foot, lower limb, upper limb and body, and they are called Link 1, Link 2, Link 3 and Link 4 respectively. The mass, length and moment of inertia of Link i are denoted as m_i, l_i and I_i $(i = 1,2,3,4)$. A virtual joint which is located at the toe is called toe joint. When the leg is in stance phase, it is in contact with the ground through the toe or/and the heel. As shown in Fig. 4.8, the toe joint is called Joint 1, and the joint between Link i and $i+1$ is called Joint i $(i = 2,3,4)$. The distance from Joint i to the center of mass for Link i is expressed by l_{gi}. A coordinate frame, (x, y), is chosen so that y-axis is along the vertical line and x-axis is on the horizontal ground. The positions of the toe, heel and mass center of the robot are denoted as (x_1, y_1), (x_2, y_2) and (x_G, y_G), respectively. The angle and torque at Joint i are represented as θ_i and τ_i respectively, and they are positive in the counter-clockwise direction $(i = 1,2,3,4)$. It is assumed that the toe joint freely rotates and the torque at the joint, τ_1, is zero. The generalized coordinates and the generalized forces for the legged robot are expressed in vector forms as $\boldsymbol{q} = [x_1, y_1, \theta_1, \theta_2, \theta_3, \theta_4]^T$ and $\boldsymbol{\tau} = [0,0,0,\tau_2,\tau_3,\tau_4]^T$. The angular momentum of the total system around the mass center is denoted as P_G.

4.3.1 Contact model between foot and ground

When the foot collides with the ground, an impact force acts at the contact point. For avoiding too large impacts and increasing the stability of movement, shock-absorbing mechanisms are often equipped under the feet of biped robots [31, 80, 81]. In this section, it is assumed that the foot is equipped with a shock-absorbing pad. The interaction force between the foot and the ground is assumed to be obtained from a linear spring and damper model in the vertical direction and a linear damper model in the horizontal direction as shown in Fig. 4.9. It is also assumed that only the toe (Joint 1) and the heel (Joint 2) could be the contact points. The thickness of the pad is denoted as y_{pad}.

The interaction forces at the heel and the toe in the vertical direction are given by the

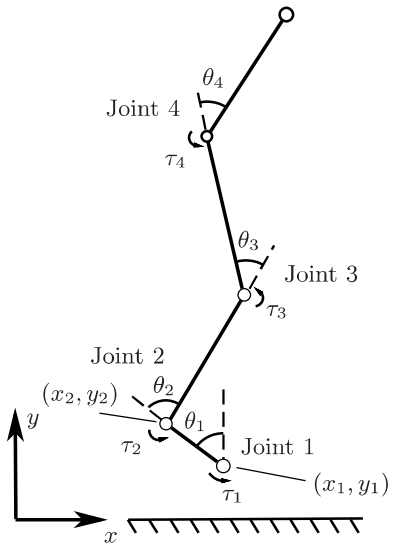

Figure 4.8: Four-link legged robot

following equation:

$$f_{yi} = \begin{cases} -k_y(y_i - y_{pad}) - d_y\dot{y}_i & \text{for } y_i < y_{pad} \\ 0 & \text{for } y_i \geq y_{pad} \end{cases}, \tag{4.1}$$

where k_y is a stiffness coefficient, d_y is a damping coefficient, and $i = 1$ and 2 for the toe and the heel respectively. Since the ground reaction force is never negative, the force f_{yi} is set to be zero if f_{yi} in (4.1) is negative. On the other hand, the interaction force in the horizontal direction can be expressed by

$$f_{xi} = \begin{cases} -d_x\dot{x}_i & \text{for } f_{yi} > 0 \\ 0 & \text{for } f_{yi} = 0 \end{cases}, \tag{4.2}$$

where d_x is a damping coefficient. Those interaction forces are written in a vector form as

$$\boldsymbol{F} = [f_{x1}, f_{y1}, f_{x2}, f_{y2}]^T. \tag{4.3}$$

4.3.2 Equations of motion

The equations of motion for the four-link legged robot can be described by

$$\boldsymbol{M}(\boldsymbol{q})\ddot{\boldsymbol{q}} + \boldsymbol{h}(\boldsymbol{q}, \dot{\boldsymbol{q}}) + \boldsymbol{\tau}_g = \boldsymbol{\tau} + \boldsymbol{J}^T\boldsymbol{F}, \tag{4.4}$$

where $\boldsymbol{M}(\boldsymbol{q})$ is the inertia matrix, $\boldsymbol{h}(\boldsymbol{q}, \dot{\boldsymbol{q}})$ is the vector with respect to the Coriolis and centrifugal effects, and $\boldsymbol{\tau}_g$ is the gravitational term. The matrix $\boldsymbol{J}$ is the Jacobian matrix with respect to the positions of the toe and the heel.

According to (4.1) and (4.2), there exist four possible contact states between the foot and the ground as shown in Fig. 4.10. All the contact states are considered in the motion planning presented in the following subsection.

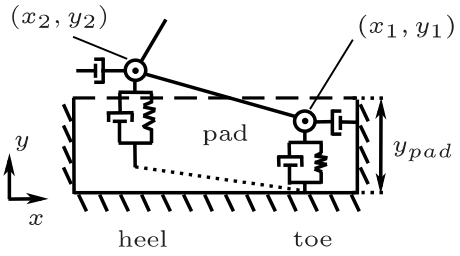

Figure 4.9: Contact model

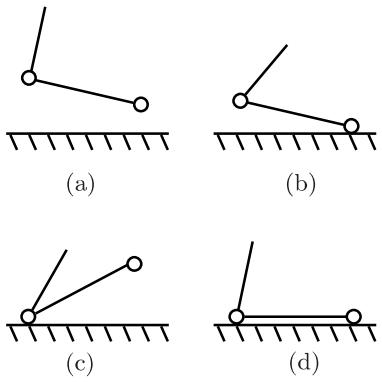

Figure 4.10: Contact states: (a) no contact, (b) contact at toe, (c) contact at heel, (d) contact at toe and heel

4.3.3 Problem formulation

This section focuses on the motion planning problem for minimizing the joint torques during jumping, on the condition that a fixed amount of translational kinetic energy is supplied to the robot by the take-off time when the foot leaves the ground. The robot is supposed to jump from rest and reach the maximum height in the air with the joints fully extended. To specify a desired jumping motion, several constraint conditions are considered as follows:

1. The horizontal position of the mass center of the robot should be above the foot at the start time.

2. The angular velocities at all joints are set to be zero at the start time, $t = T_1$, and at the end time, $t = T_3$. The angles at Joint 2, 3 and 4 are zero at $t = T_3$.

3. $\dot{x}_G(t)$, $\dot{y}_G(t)$ and P_G at the take-off time, $t = T_2$, are set to be 0[m/s], v_{T_2}[m/s] and 0[kgm^2/s], respectively.

4. The contact state turns from (ii) to (i) at the take-off time.

5. The configuration of the robot at the take-off time can be considered as the initial configuration in aerial phase.

The constraint conditions, 1 to 4, can be written as

1. $x_2(T_1) \leq x_G(T_1) \leq x_1(T_1)$.

2. $\dot{\boldsymbol{q}}(T_1) = 0$, $\dot{\theta}_i(T_3) = 0$, $\theta_i(T_3) = 0$ $(i = 2,3,4)$.

3. $(\dot{x}_G(T_2), \dot{y}_G(T_2)) = (0, v_{T_2})$, $P_G(T_2) = 0$.

4. $y_1(T_2) = y_{pad}$.

The condition 5 will be explained later.

The duration time $T_2 - T_1$ in stance phase is fixed, and the end time T_3 is chosen such that the vertical velocity of the robot is zero at $t = T_3$, that is, $T_3 = T_2 + v_{T_2}/g$ where g is the gravitational acceleration.

The following cost function is chosen as the criterion for optimization:

$$\begin{aligned} &J_C(\xi_1, \xi_2) = J_{C1}(\xi_1) + J_{C2}(\xi_2), \\ &J_{Ci}(\xi_i) = \int_{T_i}^{T_{i+1}} ((\tau_2)^2 + (\tau_3)^2 + (\tau_4)^2) dt \quad (i = 1,2), \end{aligned} \tag{4.5}$$

where (ξ_1, ξ_2) represents the parameters for optimization. The cost functions in stance phase, $t \in [T_1\ T_2]$, and in aerial phase, $t \in [T_2\ T_3]$, are denoted as $J_{C1}(\xi_1)$ and $J_{C2}(\xi_2)$, respectively. ξ_1 are chosen as $\xi_1 = (\theta_1(T_1), \theta_2(t), \theta_3(t), \theta_4(t))$ for $t \in [T_1\ T_2]$. ξ_2 are chosen as $\xi_1 = (\theta_2(t), \theta_3(t), \theta_4(t))$ for $t \in [T_2\ T_3]$. The joint angles in ξ_1 are represented by fifth order spline functions with $n = 1$ as in Appendix 3.A.2, and the ones in ξ_2 are expressed by B-spline functions in a similar way as in Appendix 3.A.1. Then, the optimal motion planning problem reduces to a parameter optimization problem, and the parameters that minimize the total cost $J_C(\xi_1, \xi_2)$ will be searched for.

The angles, angular velocities and angular accelerations, $\theta_i(t)$, $\dot{\theta}_i(t)$ and $\ddot{\theta}_i(t)$ should be continuous at the take-off time ($i = 2,3,4$). The condition 5 means that ξ_1 and ξ_2 are not independent, and it can be written as

5. $\lim_{t\to T_2+0} \theta_i = \lim_{t\to T_2-0} \theta_i$, $\lim_{t\to T_2+0} \dot{\theta}_i = \lim_{t\to T_2-0} \dot{\theta}_i$, $\lim_{t\to T_2+0} \ddot{\theta}_i = \lim_{t\to T_2-0} \ddot{\theta}_i$.

The optimal jumping motion will be obtained later by searching for the optimal values of the parameters. For the obtained motion, the take-off posture is close to a singular configuration, and the height of the mass center $y_G(T_2)$ is close to its maximum value. The influence of the take-off posture on the cost function and the jumping motion will also be investigated. The optimal motions for different take-off postures are obtained by putting one more constraint condition on $y_G(T_2)$ as

6. $y_G(T_2) = y_{GT_2}$.

Denoting $y_G(T_2)$ for the optimal motion as y_G^*, the value of y_{GT_2} is varied near y_G^* .

4.3.4 Numerical results

The physical parameters of the four-link legged robot are given in Table 4.2. The vertical velocity of the mass center at the take-off time is set to be $v_{T_2} = 1.5$[m/s]. The number of control points in aerial phase, the start time, the take-off time, and the end time are set to be $m = 10$, $T_1 = 0$[s], $T_2 = 0.1$[s] and $T_3 = 0.253$[s] respectively. The thickness and parameters of the pad are chosen as $y_{pad} = 0.01$[m], $k_y = 8.0 \times 10^5$[N/m], $d_y = 600$[Ns/m] and $d_x = 500$[Ns/m], respectively.

To find the optimal value of J_C, the MATLAB function fmincon was used. The value of ξ_1 that minimizes only J_{C1} will be firstly searched for, and the value of ξ_2 that minimizes J_{C2} satisfying the condition 5 will be found. The obtained parameters (ξ_1, ξ_2) are treated as initial values for the optimization of J_C. The optimal jumping motion was obtained where $y_G^* = 0.691$[m]. When $y_G(T_2) = 0.702$[m], all the links of the robot are aligned vertically, and the robot is at the exact singular configuration where all the joints are extended fully. Since the joint angular velocities necessary for the desired velocity v_{T_2} are infinite at the configuration, the condition that $y_G(T_2) < 0.702$[m] is imposed. Then, the optimal jumping motions with different values of y_{GT_2} near y_G^* were obtained at every 0.005[m] interval from 0.65[m] to 0.7[m], and the obtained values of J_C, J_{C1} and J_{C2} are shown in Fig. 4.11. From this figure, it is found that J_{C1} for $y_{GT_2} = 0.69$[m] $\approx y_G^*$ is much smaller than for other y_{GT_2}s, and that J_{C2} near y_G^* is also much smaller than for y_{GT_2}s which are far from y_G^*. To investigate the differences between the motions at y_G^* and at other y_{GT_2}s, the case when $y_G(T_2) = 0.65$[m] is

considered. The cases when $y_G(T_2) = 0.691[\mathrm{m}]$ and $y_G(T_2) = 0.65[\mathrm{m}]$ are called as Case A and Case B, respectively.

Table 4.2: Physical parameters of the four-link legged robot

l_1	0.07 [m]	l_2	0.3 [m]	l_3	0.3 [m]	l_4	0.2 [m]
l_{g1}	0.035 [m]	l_{g2}	0.15 [m]	l_{g3}	0.15 [m]	l_{g4}	0.1 [m]
m_1	0.2 [kg]	m_2	1 [kg]	m_3	1 [kg]	m_4	10 [kg]
I_1	0.0009 [kgm^2]	I_2	0.005 [kgm^2]	I_3	0.005 [kgm^2]	I_4	0.02 [kgm^2]

Case A

The obtained value of J_C is $39.5[\mathrm{N^2m^2s}]$, $J_{C1} = 38.3[\mathrm{N^2m^2s}]$ and $J_{C2} = 1.2[\mathrm{N^2m^2s}]$. Fig. 4.12 shows three postures at the start, take-off and end time for the optimized jumping motion. The robot jumps from rest while the part composed of Link 2, Link 3 and Link 4 moves near the singular configuration. Fig. 4.13 shows the time histories of translational and rotational energies. The translational energy reaches the desired value at T_2 while the rotational energy is kept small. The time histories of joint torques are shown in Fig. 4.14. The joint torque τ_2 is much larger than τ_3 and τ_4 in stance phase.

Case B

The obtained value of J_C is $103.7[\mathrm{N^2m^2s}]$, $J_{C1} = 86.9[\mathrm{N^2m^2s}]$ and $J_{C2} = 16.8[\mathrm{N^2m^2s}]$. Fig. 4.15 shows the initial, take-off and final postures for the optimized jumping motion. The postures in stance phase are far away from the singular configuration. Fig. 4.16 shows the time histories of translational and rotational energies. By comparing Fig. 4.13 and Fig. 4.16, it is found that even though the same amount of translational energy has been generated in stance phase, the rotational energy in Case A is much smaller than the one in Case B. The time histories of joint torques are shown in Fig. 4.17.

4.3.5 Discussion

Since the model of a four-link legged robot is extremely complex, it is very difficult to theoretically explain the usefulness of the singular configuration in the jumping motion. However, from the numerical results, the difference between the value of cost function in Case A and the one in Case B implies that the features a) and d) of singular configurations are also useful for the jumping motion of a four-link legged robot. The feature a) could be utilized at Joint 3 and Joint 4 in Case A, because the initial posture of the robot in Case A is much closer to the singular configuration than in Case B. The necessary joint torques to sustain the heavy body

around the start time in Case A are smaller than in Case B, which can be found from Figs. 4.14 and 4.17. The feature d) could be used in Case A to efficiently generate large acceleration (or force) from joint torques.

When the robot is in the air, the movement of its mass center is only affected by gravity, and the angular momentum P_G is conserved. The constraint on P_G at the take-off time, $P_G(T_2) = 0$, means that the angular movement of the whole robot stops when all the joint velocities become zero in aerial phase. At the same time, the rotational energy generated in stance phase is absorbed by joint torques. In the simulations presented in Section 4.3.4, the rotations of joints are stopped in the air with the joints fully extended. Figs. 4.13 and 4.16 show that the rotational energy in Case A is much smaller than the one in Case B, which also reduces the energy consumption of Case A in aerial phase.

The duration time $T_2 - T_1$ in stance phase is fixed in Section 4.3 for simplicity. In order to check the sensitivity of the cost function J_C with respect to T_2, the numerical optimization, by taking T_2 as one of the optimization parameters when $y_G(T_2) = 0.691[\mathrm{m}]$ and $y_G(T_2) = 0.65[\mathrm{m}]$, was performed. For $y_G(T_2) = 0.691[\mathrm{m}]$ the obtained value of T_2 is $0.0983[\mathrm{s}]$ and the corresponding cost function J_C is $39.05[\mathrm{N^2m^2s}]$. For $y_G(T_2) = 0.65[\mathrm{m}]$ the obtained value of T_2 is $0.061[\mathrm{s}]$, and the corresponding cost function J_C is $82.02[\mathrm{N^2m^2s}]$. It is found that, whether the duration time is optimized or not, the optimal cost function when $y_G(T_2) = 0.691[\mathrm{m}]$ is much smaller than the one when $y_G(T_2) = 0.65[\mathrm{m}]$.

The vertical velocity of the mass center at the take-off time v_{T_2} is also fixed in Section 4.3. The maximum height of the mass center of the robot in aerial phase is determined according to v_{T_2}. If the take-off posture is close to the singular configuration, the necessary joint velocities and torques around the take-off time become much larger as v_{T_2} is set to be larger. This might result in the increments of total cost and rotational energy unnecessary in aerial phase. To investigate the optimal jumping motions for different values of v_{T_2}, numerical optimization for different v_{T_2}s in the range from 1.1[m/s] to 3.0[m/s] has been performed. When there is no constraint on $y_G(T_2)$ as the same as in Case A, $y_G^* \geq 0.681[\mathrm{m}]$ for the obtained jumping motions. That is to say, the take-off posture for the optimal jumping motion is still close to the singular configuration for v_{T_2}s in the range. However, since there exist a number of factors, such as the duration time $T_2 - T_1$ and the parameterization method of the joint angles, that can have a strong effect on the optimal jumping motion for larger v_{T_2}, further detailed analysis is required.

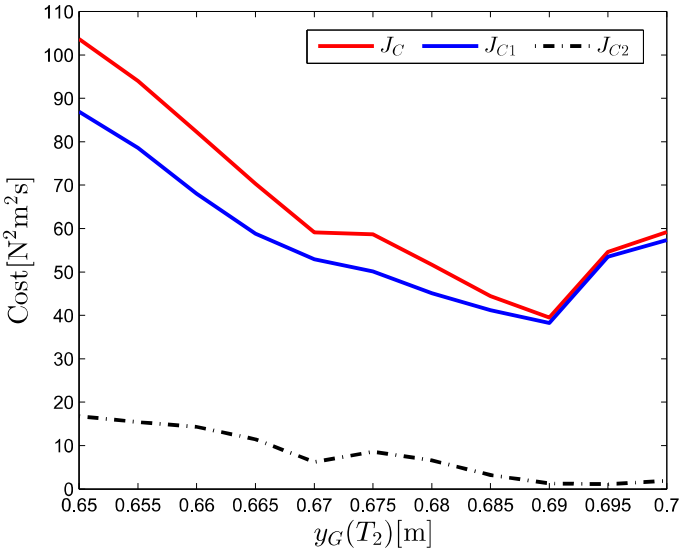

Figure 4.11: Cost functions with different $y_G(T_2)$

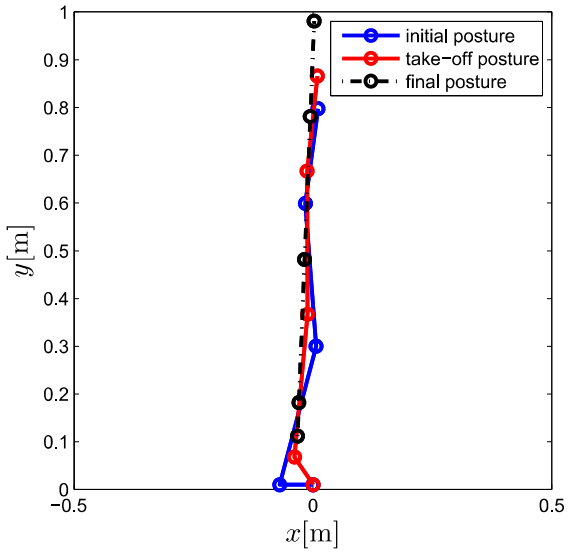

Figure 4.12: The initial, take-off and final postures of the robot for the optimized jumping motion (Case A)

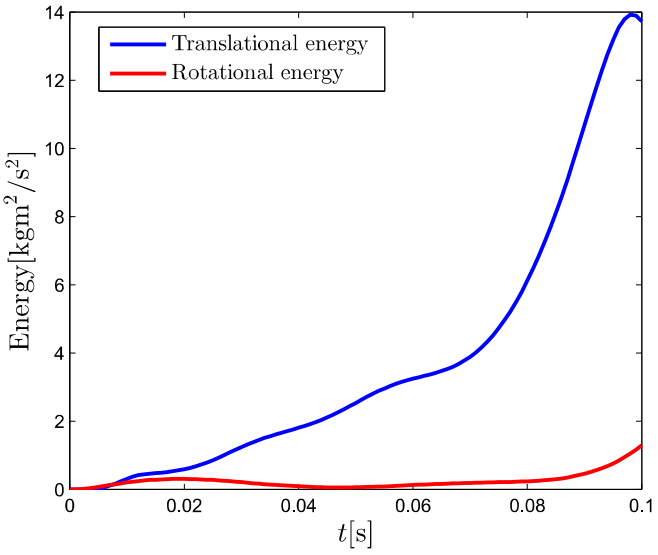

Figure 4.13: Time histories of translational and rotational energies in stance phase (Case A)

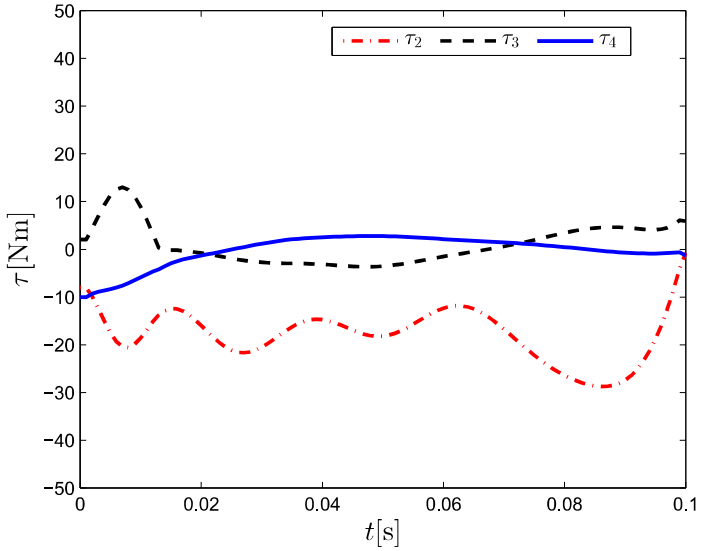

Figure 4.14: Time histories of joint torques in stance phase (Case A)

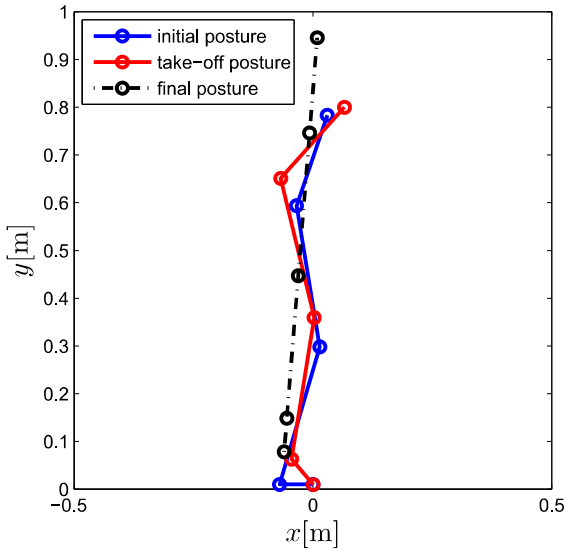

Figure 4.15: The initial, take-off and final postures of the robot for the optimized jumping motion (Case B)

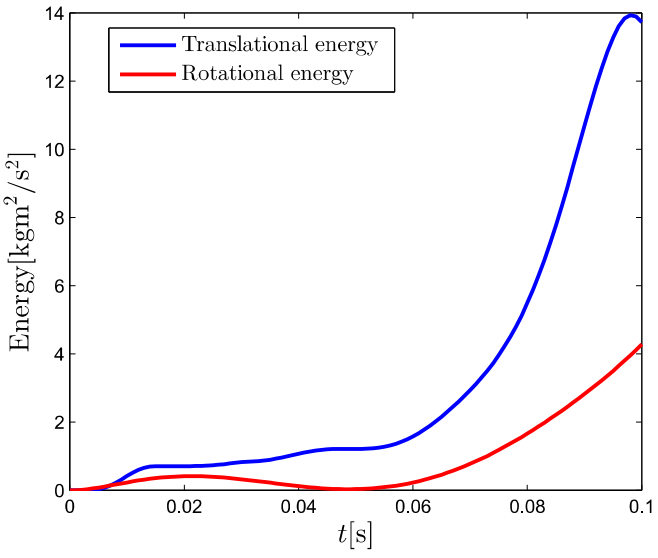

Figure 4.16: Time histories of translational and rotational energies in stance phase (Case B)

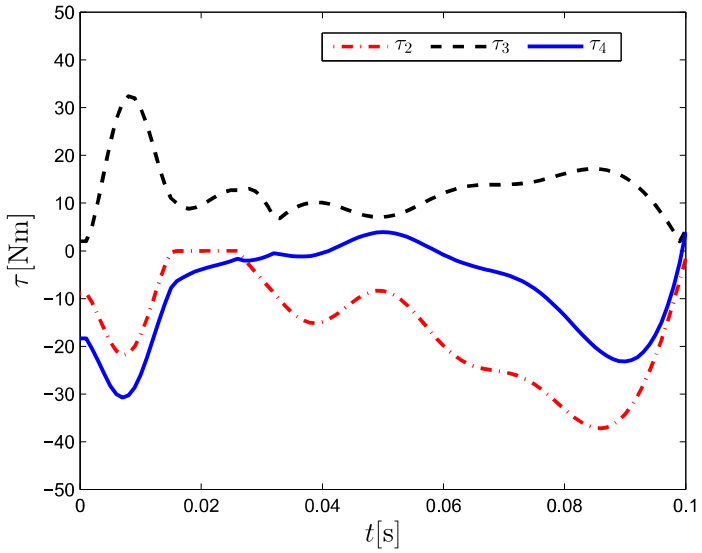

Figure 4.17: Time histories of joint torques in stance phase (Case B)

4.4 Landing Motion

4.4.1 Representation of joint torques with stiffness and damping of leg joints

The joint torques for human motions are often expressed by joint stiffness and damping. In [32], the coefficients of stiffness and damping for human hopping have been examined in detail and a nonlinear stiffness model has been proposed. Based on the results in [32], it is assumed that the joint torques are represented in the following form:

$$\tau_i = -K_i(\theta_i - \theta_{ie}) - D_i\dot{\theta}_i \quad (\text{for } i = 2,3,4), \tag{4.6}$$

where the coefficients of stiffness and damping are given as

$$K_i = K_{i1} + K_{i2}(\theta_i - \theta_{is}), \tag{4.7}$$

$$D_i = D_{i1}. \tag{4.8}$$

The angle θ_{is} is the angle of Joint i at the start time of the motion. Thus, the parameters K_{i1}, K_{i2}, D_{i1} and θ_{ie} determine the torque τ_i.

4.4.2 Problem formulation

The optimization problem of finding the landing motion that reduces the peak vertical ground reaction force and minimizes the joint torques during the landing motion simultaneously is formulated. The model of the four-link legged robot and the contact model between the foot and the ground are the same as the ones introduced in Section 4.3. The following cost function is chosen as criterion for optimization:

$$J_C(\phi) = c_1 W_1 + W_2, \tag{4.9}$$

where c_1 is the weight coefficient with respect to W_1. The functions W_1 and W_2 are defined as:

$$W_1 = \max_{t\in[0,T]}(f_{y1}(t) + f_{y2}(t)), \tag{4.10}$$

$$W_2 = \int_0^T ((\tau_2)^2 + (\tau_3)^2 + (\tau_4)^2)dt, \tag{4.11}$$

where W_1 represents the peak value of vertical ground reaction force. The time t is set to be zero at the instant when the first contact between the foot and the ground occurs, and T denotes the end time of the landing motion.

In (4.9), ϕ represents the parameters for optimization and is chosen as the initial posture $\boldsymbol{\theta}(0) = (\theta_1(0), \theta_2(0), \theta_3(0), \theta_4(0))$, the coefficients K_{i1}, K_{i2}, D_{i1}, θ_{ie} $(i = 2,3,4)$ and the duration time T:

$$\phi = \{\boldsymbol{\theta}(0), K_{i1}, K_{i2}, D_{i1}, \theta_{ie}, T\}. \tag{4.12}$$

For a landing motion of the legged robot, it is assumed that, just before the contact with the ground, all the joint angular velocities are zero and the downward velocity of the robot is v_t. The initial values of generalized velocities are summarized as

$$\dot{\boldsymbol{q}}(0) = [0, -v_t, 0, 0, 0, 0]^T. \tag{4.13}$$

The initial posture is assumed to satisfy $0 \leq \theta_1(0) < \pi/2$, that is, the first contact between the foot and the ground occurs in the state (b) shown in Fig. 4.10. After the first contact, the second and multiple contacts between the foot and the ground may happen in the state (b), (c) or (d).

At the end time of the motion, four constraints are added to the optimization problem as follows:

1. The horizontal position of the mass center of the robot should be above the foot at the

end time $t = T$, which can be expressed as follows:

$$x_2 \leq x_g(T) \leq x_1, \tag{4.14}$$

where x_g is the horizontal position of the mass center.

2. The robot should be stationary at $t = T$:

$$\dot{\boldsymbol{q}}(T) = 0. \tag{4.15}$$

3. The angle of the body from the vertical direction should be small at $t = T$ so that the final posture of the robot is close to the one in human landing motion:

$$|\theta_t(T)| \leq \pi/4, \tag{4.16}$$

where $\theta_t = \theta_1 + \theta_2 + \theta_3 + \theta_4$.

4. The landing motion should be finished in 1[s]:

$$T \leq 1. \tag{4.17}$$

4.4.3 Numerical results

By changing the value of c_1, the optimal solutions for the soft landing and the stiff one can be obtained. The solutions for different values of c_1 will be obtained by numerical optimization. To find the optimal values of J_C, the MATLAB function, fmincon, was used. The physical parameters of the robot and the shock-absorbing pad are chosen as the same as the ones used in the previous section, except that $m_4 = 5$[kg] and $k_y = 4.0 \times 10^5$[N/m]. The initial downward velocity of the robot v_t is set to be 1.5[m/s]. The numerical optimization was performed in two cases, Case 1 and Case 2, where the weight c_1 is set to be 0 and 1 respectively. In Case 1, since $c_1 = 0$, the cost function in (4.9) becomes $J_C = W_2$, while $J_C = W_1 + W_2$ in Case 2.

Case 1

The motion obtained by numerical simulation is shown in Fig. 4.18 where the postures of the robot are drawn at every $T/5$[s]. The time histories of joint angular velocities and joint torques are shown in Figs. 4.19 and 4.20 respectively. The work done by each joint is calculated from them as shown in Fig. 4.21. The values of W_1 and W_2 for the obtained motion are 1192.3[N] and 4.03[N^2m^2s]. The optimal duration time T is 0.538[s].

From Fig. 4.18, the initial posture of the robot is close to the singular configuration that the leg is stretched out. After the first contact between the foot and the ground, the absolute values of $\dot{\theta}_2$ and τ_2 increase intensely in Figs. 4.19 and 4.20, while the others are relatively small during landing. Thus, the absolute value of work done by τ_2 is much larger than by τ_3 and τ_4 as in Fig. 4.21. That is, a large part of the kinetic energy of robot is absorbed at Joint 2 to stop the landing motion.

Case 2

The motion obtained by numerical simulation is shown in Fig. 4.22 where the postures of the robot are drawn at every $T/5$[s]. Figs. 4.23, 4.24 and 4.25 show the time histories of joint angular velocities, joint torques and work done by joint torques respectively. The values of W_1 and W_2 for the obtained motion are 377.4[N] and 65.4[N^{2}m^{2}s]. The optimal duration time T is 0.496[s].

At the initial posture, Joint 2 is flexed more than in Case 1. The impact force and the value of W_1 are smaller than in Case 1, while the joint torque τ_2 absorbs less energy. The energy of the robot is also absorbed by the joint torques τ_3 and τ_4 as shown in Fig. 4.25.

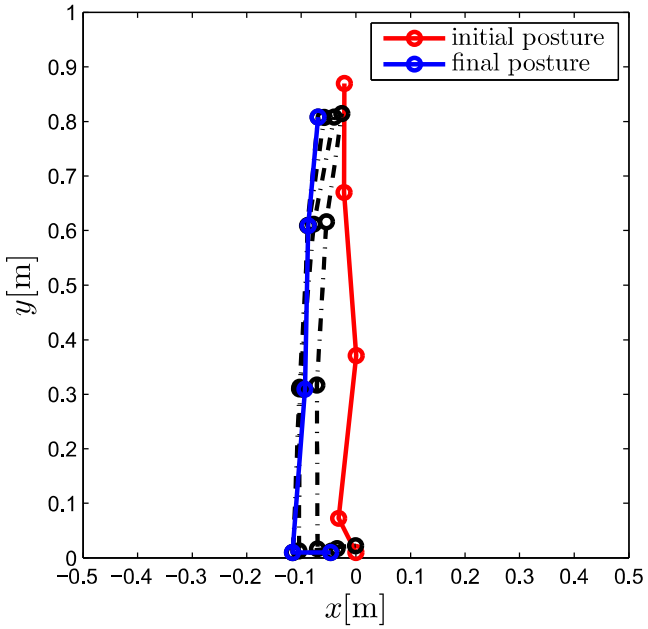

Figure 4.18: Optimal motion of a legged robot(Case 1)

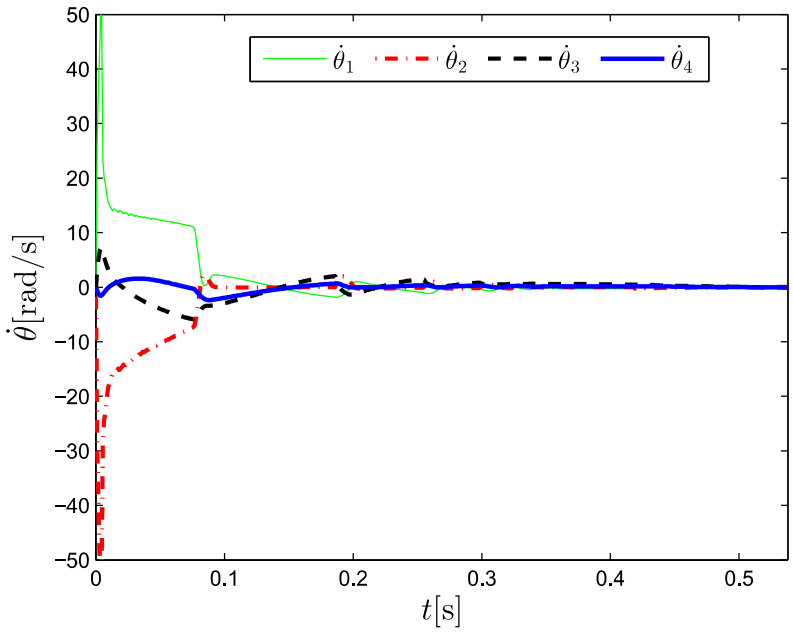

Figure 4.19: Time histories of joint angular velocities(Case 1)

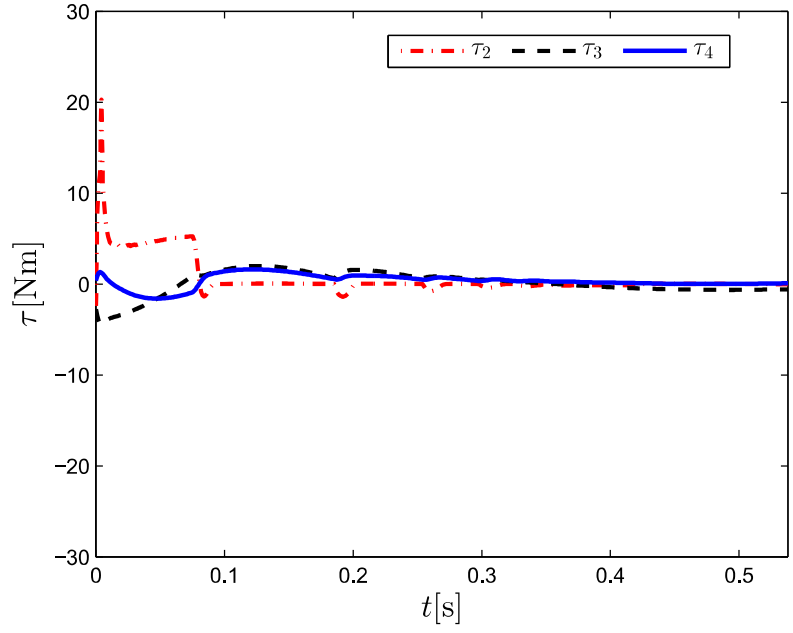

Figure 4.20: Time histories of joint torques(Case 1)

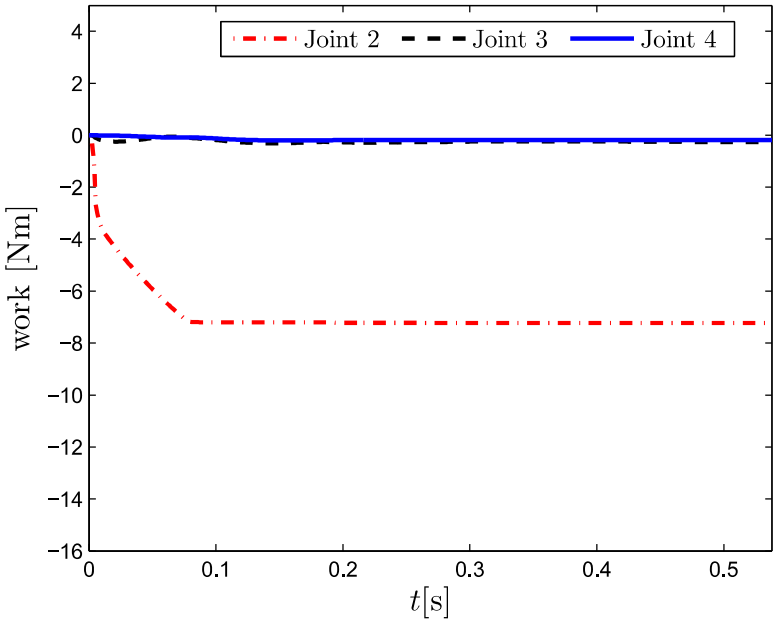

Figure 4.21: Time histories of the work done by joint torques(Case 1)

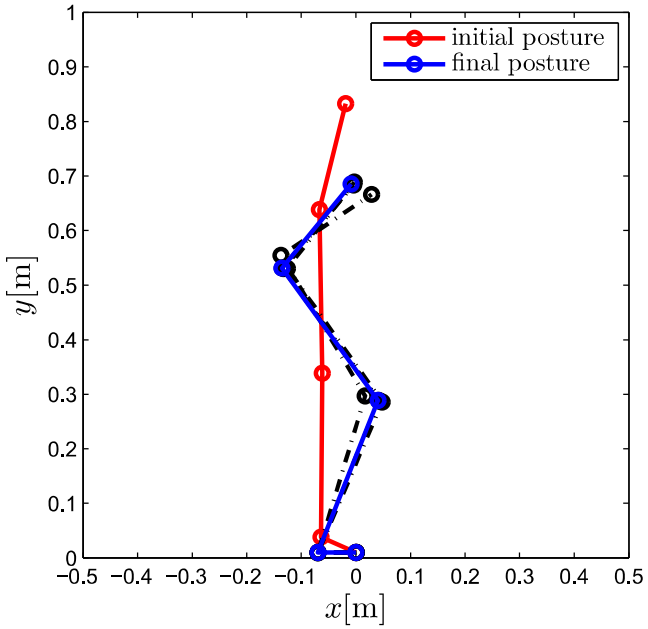

Figure 4.22: Optimal motion of a legged robot(Case 2)

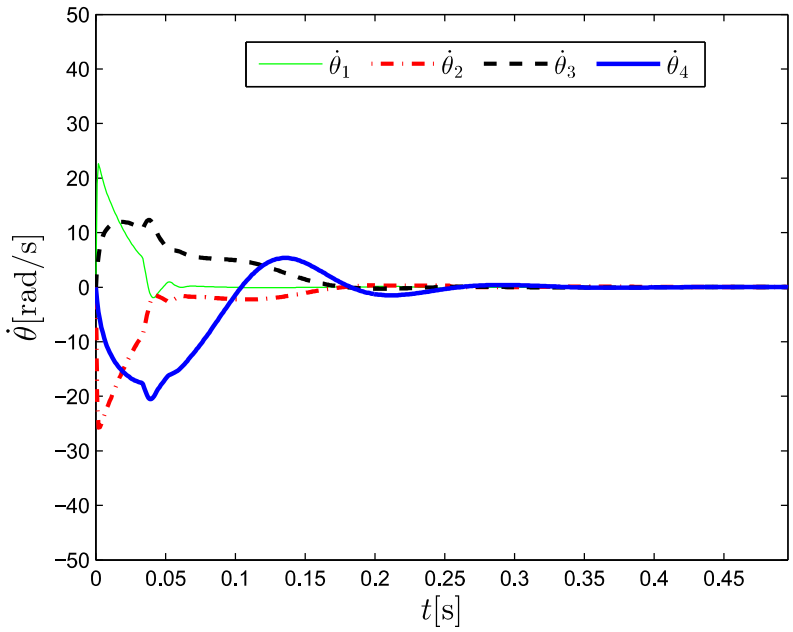

Figure 4.23: Time histories of joint angular velocities(Case 2)

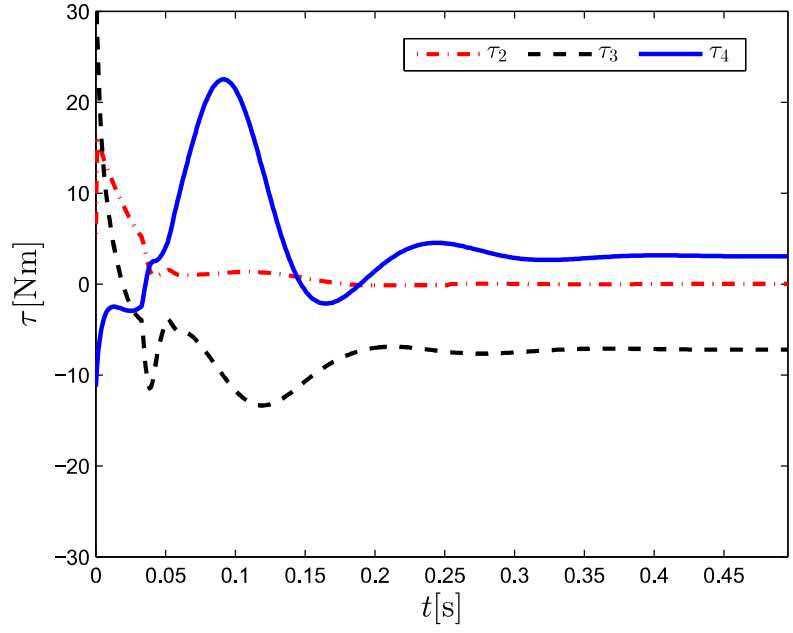

Figure 4.24: Time histories of joint torques(Case 2)

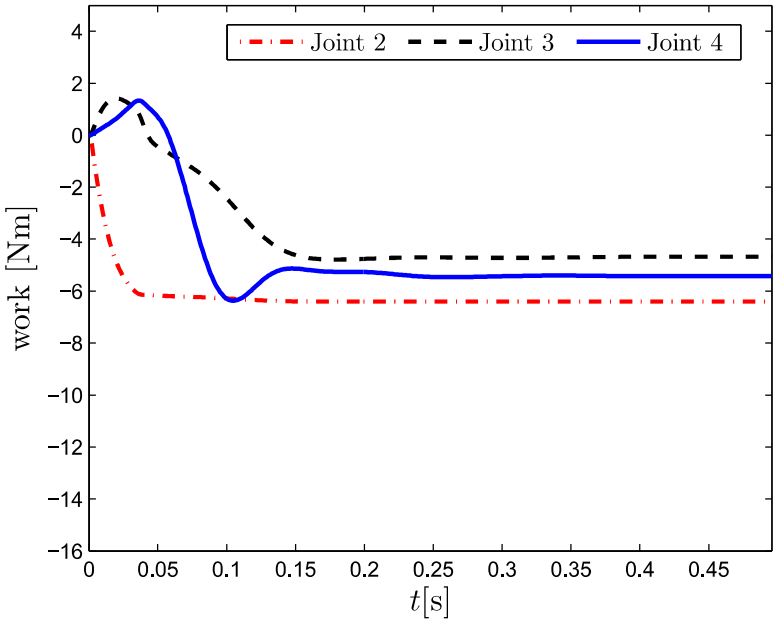

Figure 4.25: Time histories of the work done by joint torques(Case 2)

4.4.4 Impact dynamics with a simple model

The numerical results in Section 4.4.3 show that the initial posture where Joint 2 is more flexed reduces the impact force, while the one with smaller θ_2 makes the time integral of joint torques smaller. The impact force has been investigated so far based on the discontinuous impact model where the impact occurs in an infinitesimally small period, and it is well known that flexed postures are advantageous in reducing the impact force [26]. In this subsection, the dynamic behavior of the robot at the impact instance will be analyzed by using a simplified model of the legged robot. The analytical results will explain not only the impact force but also the joint angular velocity right after the impact. For a larger joint angular velocity, the joint torque necessary to absorb the kinetic energy of the robot is smaller.

A simple model of a legged robot is considered as shown in Fig. 4.26. The leg is composed of two links, link 1 and link 2, and the body is modeled as a heavy mass point attached at the top end of the leg. The mass and length of link i are denoted as m_{ai} and l_{ai} respectively($i = 1,2$), and the mass of the body is m_w. The moment of inertia and the distance from joint i to the center of mass for link i are expressed by I_{ai} and l_{gi}. The bottom end of the leg is supposed to be a contact point, and its position is expressed as $\boldsymbol{p}_b = [x_b, y_b]^T$. The position of the top end is denoted as $\boldsymbol{p}_e = [x_e, y_e]^T$. In a similar manner as in Section 4.4.2, the angles and the joint torques are denoted as θ_{ai} and τ_{ai} ($i = 1,2$), and expressed in vector forms as $\boldsymbol{\theta}_a = [\theta_{a1}, \theta_{a2}]^T$,

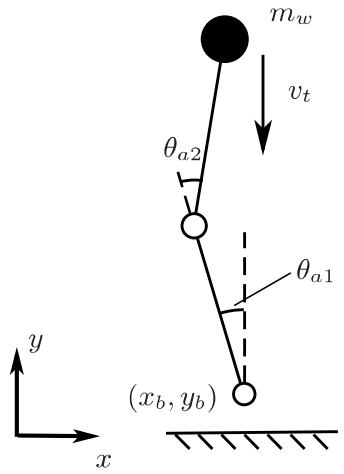

Figure 4.26: Simple model of a legged robot with a heavy mass point (body)

$\boldsymbol{\tau}_a = [0, \tau_{a2}]^T$, noting that $\tau_{a1} = 0$. The generalized coordinates and generalized forces for the system can be represented as $\boldsymbol{q} = [\boldsymbol{p}_b^T, \boldsymbol{\theta}_a^T]^T$ and $\boldsymbol{\tau} = [0,0,0,\tau_{a2}]^T$.

The variables just before and after the collision with the ground are denoted by superscripts $-$ and $+$ respectively. Similarly as in (4.15), the generalized velocities are chosen as $\dot{\boldsymbol{\theta}}_a^- = [0,0]^T$ and $\dot{\boldsymbol{p}}_b^- = [0,-v_t]^T$. The angular velocity $\dot{\boldsymbol{\theta}}_a^+$ and the impulse applied at the contact point will be analyzed under the following assumptions:

1. A perfectly inelastic collision occurs; the velocity of the bottom end of the robot becomes zero just after collision, that is, $\dot{\boldsymbol{p}}_b^+ = [0,0]^T$.
2. The mass of the body is much larger than the ones of link 1 and link 2, namely, $m_w \gg m_{a1}, m_{a2}$.

The equations of motion for the robot are expressed as follows:

$$\boldsymbol{M}(\boldsymbol{q})\ddot{\boldsymbol{q}} + \boldsymbol{h}(\boldsymbol{q},\dot{\boldsymbol{q}}) + \boldsymbol{\tau}_g = \boldsymbol{\tau} + \boldsymbol{J}_b^T \boldsymbol{F}, \tag{4.18}$$

where

$$\boldsymbol{M} = \begin{bmatrix} \boldsymbol{M}_1 & \boldsymbol{M}_2 \\ \boldsymbol{M}_2^T & \boldsymbol{M}_3 \end{bmatrix}, \tag{4.19}$$

$$\boldsymbol{M}_1 = \begin{bmatrix} m_{a1} + m_{a2} + m_w & 0 \\ 0 & m_{a1} + m_{a2} + m_w \end{bmatrix}, \tag{4.20}$$

$$\boldsymbol{M}_2 = m_{a1}\boldsymbol{J}_{g1} + m_{a2}\boldsymbol{J}_{g2} + m_w\boldsymbol{J}_e, \tag{4.21}$$

$$\boldsymbol{M}_3 = \boldsymbol{M}_a + m_w \boldsymbol{J}_e^T \boldsymbol{J}_e. \tag{4.22}$$

The matrix $\boldsymbol{M}_a$ is the inertia matrix of the leg composed of two links, and does not include the inertia of the heavy mass point. The matrices $\boldsymbol{J}_b$, $\boldsymbol{J}_{g1}$, $\boldsymbol{J}_{g2}$ and $\boldsymbol{J}_e$ are the Jacobian matrices with respect to $\boldsymbol{p}_b$, the mass centers of link 1 and link 2, and $\boldsymbol{p}_e$, respectively. Note that $\boldsymbol{J}_b$ and $\boldsymbol{J}_e$ are expressed as

$$\boldsymbol{J}_b = \begin{bmatrix} 1 & 0 & 0 & 0 \\ 0 & 1 & 0 & 0 \end{bmatrix}, \tag{4.23}$$

$$\boldsymbol{J}_e = -\begin{bmatrix} \mathrm{c}\theta_{a1} & -\mathrm{s}\theta_{a1} \\ \mathrm{s}\theta_{a1} & \mathrm{c}\theta_{a1} \end{bmatrix} \begin{bmatrix} l_{a1} + l_{a2}\mathrm{c}\theta_{a2} & l_{a2}\mathrm{c}\theta_{a2} \\ l_{a2}\mathrm{s}\theta_{a2} & l_{a2}\mathrm{s}\theta_{a2} \end{bmatrix}, \tag{4.24}$$

where c$*$ and s$*$ mean $\cos(*)$ and $\sin(*)$. The vector $\boldsymbol{F} = [F_y, F_y]^T$ represents the ground reaction force.

In a similar way as in [30], it is assumed that the impact with the ground occurs in an infinitesimally small period of time δt and a finite translational momentum $\bar{\boldsymbol{F}}$ is supplied from $\boldsymbol{F}$ during the period. Integrating (4.18) during the period, the following equation is obtained:

$$\lim_{\delta t \to 0} \int_0^{\delta t} (\boldsymbol{M}(\boldsymbol{q})\ddot{\boldsymbol{q}} + \boldsymbol{h}(\boldsymbol{q}, \dot{\boldsymbol{q}}) + \boldsymbol{\tau}_g) dt = \lim_{\delta t \to 0} \int_0^{\delta t} (\boldsymbol{\tau} + \boldsymbol{J}_b^T \boldsymbol{F}) dt. \tag{4.25}$$

The above equation is rewritten as

$$\boldsymbol{M}(\boldsymbol{q})(\dot{\boldsymbol{q}}^+ - \dot{\boldsymbol{q}}^-) = \boldsymbol{J}_b^T \bar{\boldsymbol{F}}. \tag{4.26}$$

From the assumption 1 and (4.26), the impulse $\bar{\boldsymbol{F}}$ is derived as

$$\bar{\boldsymbol{F}} = -(\boldsymbol{J}_b \boldsymbol{M}^{-1} \boldsymbol{J}_b^T)^{-1} \boldsymbol{J}_b \dot{\boldsymbol{q}}^-. \tag{4.27}$$

By substituting (4.27) into (4.26), $\dot{\boldsymbol{q}}^+$ is obtained as

$$\dot{\boldsymbol{q}}^+ = (I_{4\times 4} - \boldsymbol{M}^{-1} \boldsymbol{J}_b^T (\boldsymbol{J}_b \boldsymbol{M}^{-1} \boldsymbol{J}_b^T)^{-1} \boldsymbol{J}_b) \dot{\boldsymbol{q}}^-. \tag{4.28}$$

By using (4.19) and (4.23), the impulse and the joint angular velocity just after the collision are represented as

$$\bar{\boldsymbol{F}} = -(\boldsymbol{M}_1 - \boldsymbol{M}_2 \boldsymbol{M}_3^{-1} \boldsymbol{M}_2^T) \dot{\boldsymbol{p}}_b^- = -(\boldsymbol{M}_1 \dot{\boldsymbol{p}}_b^- - \boldsymbol{M}_2 \dot{\boldsymbol{\theta}}_a^+), \tag{4.29}$$

$$\dot{\boldsymbol{\theta}}_a^+ = \boldsymbol{M}_3^{-1}\boldsymbol{M}_2^T\dot{\boldsymbol{p}}_b^- \ . \tag{4.30}$$

From (4.29) and (4.30), the values of $\bar{\boldsymbol{F}}$ and $\dot{\boldsymbol{\theta}}_a^+$ are varied by the posture of the robot $\boldsymbol{\theta}_a$ and the link parameters such as l_{a1} and l_{a2}. The solutions of $\bar{\boldsymbol{F}}$ and $\dot{\boldsymbol{\theta}}_a^+$ in (4.29) and (4.30) are a little complicated to understand their variations for all the joint angles $\boldsymbol{\theta}_a$ and all the link lengths l_{a1} and l_{a2}. In this subsection, their variations will be investigated under the following conditions:

$$l_{a1} = l_{a2},\ \theta_{a2} = -2\theta_{a1},\ 0 \leq \theta_{a1} \leq \pi/4[\mathrm{rad}]. \tag{4.31}$$

The posture of the robot with the conditions can be changed from posture A to posture B as shown in Fig. 4.27, keeping the position of the mass point just above the contact point. For posture B, the leg is in the singular configuration with $\theta_{a1} = 0[\mathrm{rad}]$ and the matrix $\boldsymbol{J}_e$ is singular.

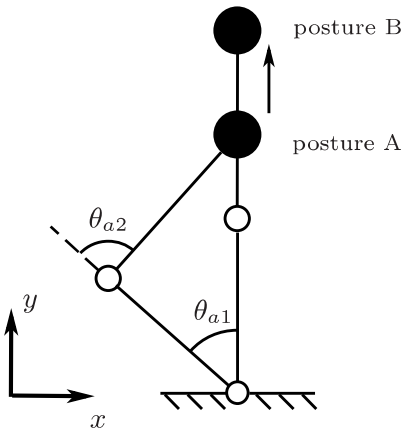

Figure 4.27: Range of postures: from posture A to posture B

Table 4.3: Physical parameters of the simple model

l_{a1}	0.6 [m]	l_{a2}	0.6 [m]
l_{g1}	0.3 [m]	l_{g2}	0.3 [m]
I_{a1}	0.01 [kgm^2]	I_{a2}	0.01 [kgm^2]
m_{a1}	1 [kg]	m_{a2}	1 [kg]
m_w	50 [kg]	v_t	1.5 [m/s]

From the assumption 2, (4.30) and (4.31), the approximate solution of $\dot{\boldsymbol{\theta}}_a^+$ can be obtained

as

$$\dot{\boldsymbol{\theta}}_a^+ = \begin{bmatrix} \dot{\theta}_{a1}^+ \\ \dot{\theta}_{a2}^+ \end{bmatrix} \approx \begin{bmatrix} \dfrac{2m_w l_{a1} v_t s(1-s^2)}{4m_w l_{a1}^2 s^2(1-s^2)+K} \\ \dfrac{-4m_w l_{a1} v_t s(1-s^2)}{4m_w l_{a1}^2 s^2(1-s^2)+K} \end{bmatrix}, \tag{4.32}$$

where $K = m_{a1} l_{g1}^2 + m_{a2}(l_{a1} - l_{g2})^2 + I_{a1} + I_{a2}$ and the variable s is defined as $s = \sin\theta_{a1}$. Under (4.31), the range of s satisfies $0 \le s \le \sqrt{2}/2$. Posture A and posture B correspond to $s = \sqrt{2}/2$ and $s = 0$ respectively. By substituting (4.32) into (4.29), the vertical impulse $\bar{F}_y$ can be approximately calculated as

$$\bar{F}_y \approx m_w v_t - \frac{4m_w^2 l_{a1}^2 v_t s^2(1-s^2)}{4m_w l_{a1}^2 s^2(1-s^2)+K}. \tag{4.33}$$

Furthermore, the kinetic energy of the robot just after the collision, $E^+ = (\dot{\boldsymbol{\theta}}_a^{+T} \boldsymbol{M}_3 \dot{\boldsymbol{\theta}}_a^+)/2$, can be calculated from (4.32) as

$$E^+ \approx \frac{2m_w^2 l_{a1}^2 v_t^2 s^2(1-s^2)}{4m_w l_{a1}^2 s^2(1-s^2)+K} \approx \frac{1}{2} v_t (m_w v_t - \bar{F}_y). \tag{4.34}$$

From (4.32), the variation of $\dot{\boldsymbol{\theta}}_a^+$ can be seen explicitly. Noting that $\dot{\theta}_{a2}^+ = -2\dot{\theta}_{a1}^+$ in (4.32), the behavior of $\dot{\theta}_{a2}^+$ will be emphasized below. The absolute value of $\dot{\theta}_{a2}^+$ is zero at $s = 0$, and sharply increases as s becomes slightly larger. The peak of $|\dot{\theta}_{a2}^+|$ occurs at $s = s^*$ where

$$s^* \approx \frac{1}{2l_{a1}} \sqrt{\frac{K}{m_w}}. \tag{4.35}$$

As s approaches $\sqrt{2}/2$ from s^*, $|\dot{\theta}_{a2}^+|$ monotonically decreases. Therefore, $|\dot{\theta}_{a2}^+|$ has the maximum value for the posture where $s = s^*$. Since s^* is small from (4.35) and the assumption 2, the posture is close to posture B where the leg is in a singular configuration. As a result, $|\dot{\theta}_{a2}^+|$ has the maximum value at the posture close to the singular posture B, while it is zero at posture B. The profile of $\dot{\theta}_{a2}^+$ as a function of s is drawn in Fig. 4.28, by using the physical parameters in Table 4.3.

From (4.29), $\bar{F}_y$ has the maximum value at $s = 0$, and monotonically decreases as s approaches $\sqrt{2}/2$. That is to say, $\bar{F}_y$ increases as the posture becomes close to the singular posture B. Figure 4.29 shows the profile $\bar{F}_y$ as a function of s by using the physical parameters in Table 4.3.

Moreover, the similar behavior of $\dot{\theta}_{a2}^+$ and $\bar{F}_y$ can be obtained, even if $\theta_{a2} \neq -2\theta_{a1}$ and $l_{a1} \neq l_{a2}$. This is easily verified by calculating their variations numerically by using (4.29) and

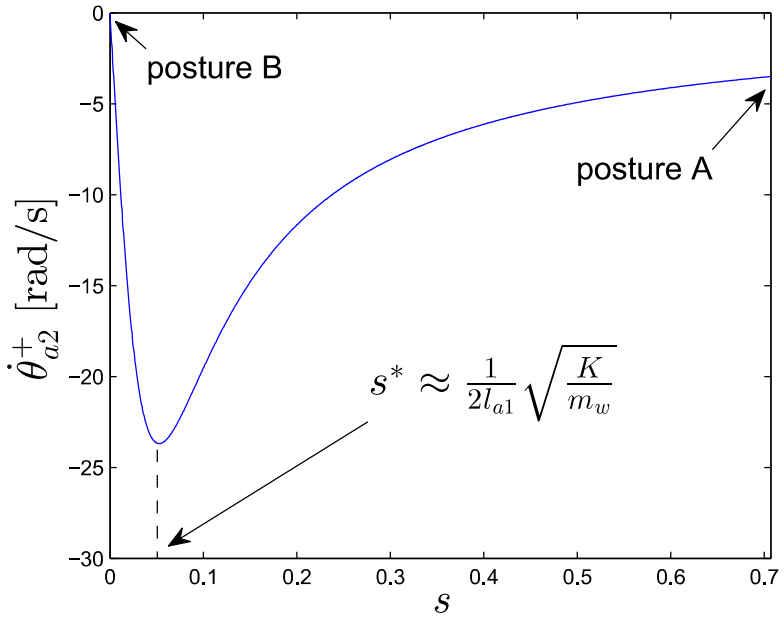

Figure 4.28: Variation of $\dot{\theta}_{a2}^{+}$ with respect to s

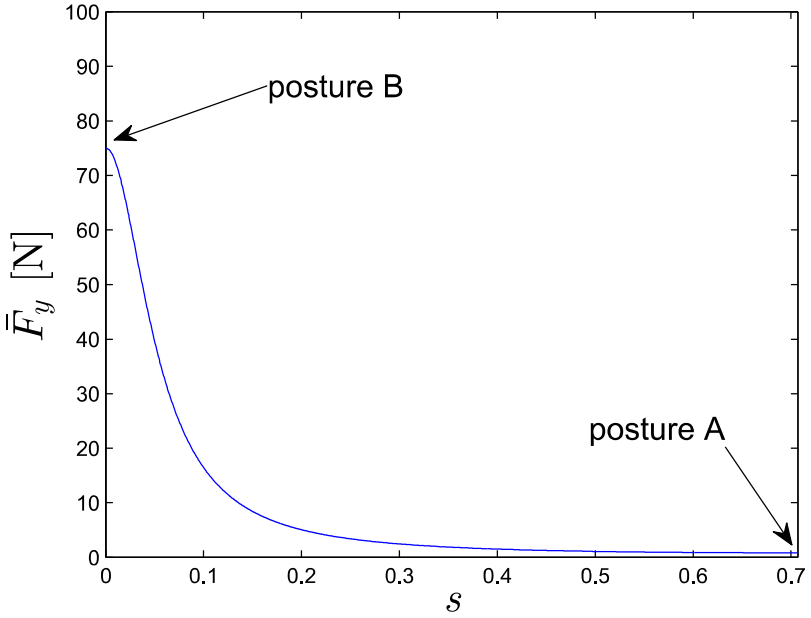

Figure 4.29: Variation of $\bar{F}_y$ with respect to s

(4.30).

As the above results, the posture where the leg is bent is advantageous in reducing the impulse $\bar{F}_y$ that would correspond to W_1 in Section 4.4.3. On the other hand, the posture around $s = s^*$ can be useful for reducing the joint torques necessary for the landing motion. For the simple model, the rate of work done by joint torques after the impact can be expressed as

$$P_a = \boldsymbol{\tau}_a^T \dot{\boldsymbol{\theta}}_a = \tau_{a2} \dot{\theta}_{a2}. \tag{4.36}$$

Since $|\dot{\theta}_{a2}^+|$ has the maximum value at $s = s^*$, the kinetic energy of the robot can be absorbed most efficiently by τ_{a2}. The kinetic energy E^+ also depends on the posture as in (4.34). For the posture with $s = s^*$, a part of the kinetic energy $E^- = (m_{a1} + m_{a2} + m_w) v_t^2/2$ is eliminated by the inelastic collision with the ground, while almost all the energy E^- remains as E^+ for the posture close to posture A. Therefore, the posture around $s = s^*$, that is close to the singular posture B, is advantageous in reducing the joint torque τ_{a2} that would correspond to W_2 in Section 4.4.3.

4.4.5 Discussion

From the numerical results in Case 1 and the theoretical results in Section 4.4.4, the amount of joint torques necessary for the landing motion is reduced for the posture that is close to a singular one. As mentioned in Section 4.4.4, the kinetic energy E^+ for the simple model depends on the posture as in (4.34). For posture B where $s = 0$, E^+ becomes zero, though the impulse $\bar{F}_y$ has the maximum value. From the assumption 1 of the perfectly inelastic collision, all the energy E^- is eliminated despite $\tau_{a2} = 0$. The corresponding motion for the four-link legged robot in Section 4.4.3 is the motion where all the joints of the robot are fully extended and the robot bounces on the ground multiple times until all the energy E^- is eliminated. Although $W_2 = 0$ for the motion, it was not found in the numerical optimization for Case 1 from the constraints (4.15) and (4.17). Instead, for the motion obtained in Case 1, non-zero E^+ is provided to the robot at the posture around $s = s^*$, and W_2 is reduced from the large energy absorption rate P_a.

Regarding the subsystem composed of three links, Link 2, 3 and 4, as one link, the four-link legged robot can be considered as a simple model composed of Link 1 and the subsystem. From (4.30), the value of θ_{a1} that maximizes $|\dot{\theta}_{a2}^+|$ for the simple model can be obtained numerically. The obtained value θ_{a1}^* is 0.69 [rad], while the corresponding values in Case 1 and 2 are 0.47 [rad] and 1.15 [rad]. In Case 1, θ_1 at the initial posture is close to θ_{a1}^*, $|\dot{\theta}_2^+| \left(\approx |\dot{\theta}_{a2}^+|\right)$ becomes large after collision as shown in Fig. 4.19, and the joint torque τ_2

absorbs the kinetic energy of the robot efficiently as shown in Fig. 4.21. On the other hand, in Case 2, $|\dot{\theta}_2^+|$ is much smaller than in Case 1 as shown in Fig. 4.23. The absorption of energy at Joint 2 is not sufficient to stop the motion of the robot, and the torques τ_3 and τ_4, also absorb the energy as shown in Fig. 4.25.

It should be noted that the value of cost function W_2 also depends on the posture of the robot around the end time. Since the robot is in the contact state (d) around the end time, the posture of the subsystem composed of Link 2, 3 and 4 affects highly the joint torques necessary to sustain the heavy body due to the feature a). In Case 1, the posture of the subsystem is kept near the singular posture where the three links are aligned in a straight line, and the joint torques become very small around the end time from the feature a) as shown in Fig. 4.20. In Case 2, the posture of the subsystem is far from the singular one around the end time, and large joint torques continue to be required as shown in Fig. 4.24.

Moreover, optimization results for other values of c_1 show that, as the value of c_1 approaches 0, the obtained optimal motion becomes similar to the one in Case 1. For the value of c_1 larger than 1, the optimal motion is almost the same as in Case 2.

4.5 Conclusion

Both the numerical optimization results in Sections 4.2 and 4.3 showed that the features a) and d) of singular configurations are advantageous in the vertical jumping motions (in stance phase) of two-link and four-link legged robots. In Section 4.4, numerical optimization results with different weights for the cost function showed that the posture of the leg close to a singular posture is useful for reducing the joint torques during landing, partly because of the feature a). According to the investigation of the impact dynamics, just after collision, the energy absorption rate for the posture around $s = s^*$ is much larger than the one for the posture far away from the singular posture, when the joint torques are limited. Meanwhile, the rest of the kinetic energy after collision for the posture around $s = s^*$ is much smaller. Thus, the kinetic energy that needs to be eliminated can be efficiently absorbed by the joint torques at the posture close to the singular one. Moreover, the flexion of the leg is advantageous in reducing the reaction force. Those results were explained by a theoretical analysis of a simplified model for the legged robot.

Chapter 5

Conclusions

This dissertation illustrated the advantages of singular configurations in robot motions by theoretical analysis and numerical simulations, for the purpose of understanding the dynamics of the robot near singular configurations.

Firstly, a general expression of kinematic and dynamic equations for a multibody system which is designed as a series of rigid links was introduced in Section 2.2. Sections 2.4 and 2.5 listed the features of singular configurations. These features are shown as follows:

a) Large loads can be sustained by small joint torques near singular configurations.

b) Joint torques can generate the kinetic energy efficiently near singular configurations.

c) The energy is stored in the manipulator and causes large acceleration near singular configurations.

d) The torque-dependent acceleration of the object has its largest value when the robot configuration is close to, but not exactly, a singular configuration.

The features a) and b) have been derived from the theoretical analysis of the Jacobian matrix and the inertia matrix respectively. To give a theoretical explanation of the features c) and d), the Jacobian and inertia matrices were combined together, and the end-effector acceleration of a two-link manipulator with a heavy object and a fixed base was investigated by using a simplified model. The acceleration was divided into three components, torque-dependent, gravity-dependent and velocity-dependent accelerations. The features c) and d) were explained clearly, based on the analytical solutions to the velocity-dependent and torque-dependent accelerations respectively.

The numerical simulation results in Chapters 3 and 4 showed that they are applicable to several kinds of robots and robot motions, that are classified in Table 1.1. All the features

a) to d) can be utilized in the motions of lifting up a heavy object by a two-link manipulator (with fixed base in a vertical plane) as shown in Sections 3.2 and 3.3. The features b), c) and d) can be utilized in the motions of pulling a heavy object by a two-link mobile manipulator (with unfixed base in a horizontal plane) as shown in Section 3.4. The features a) and d) can be utilized in the vertical jumping motions of two-link/four-link legged robot (with unfixed base in a vertical plane) as shown in Sections 4.2 and 4.3. Section 4.4 showed that the feature a) can be utilized in the landing motions of a four-link legged robot (with unfixed base in a vertical plane), and the posture of the robot close to a singular one at the impact instance is useful for reducing the necessary joint torques.

The dynamic features summarized in this dissertation could be utilized for a practical controller design. For a two-link manipulator, the ratios of joint torques to use the features b) and d) depend only on the lengths of links. The vector of joint velocities to use the feature c) are also parallel to them. Thus, there's no need to know the actual weight of the object, and to plan the robot motion in advance. The controller design for utilizing the singular configurations would be greatly simplified.

References

[1] Kazuo Hirai, Masato Hirose, Yuji Haikawa, and Toru Takenaka. The development of honda humanoid robot. In *Proceedings of the IEEE International Conference on Robotics and Automation*, volume 2, pages 1321–1326, 1998.

[2] Takayuki Kanda, Hiroshi Ishiguro, Michita Imai, and Tetsuo Ono. Body movement analysis of human-robot interaction. In *Proceedings of the 18th International Joint Conference on Artificial Intelligence*, pages 177–182, 2003.

[3] Junichi Urata, Yuto Nakanishi, Kei Okada, and Masayuki Inaba. Design of high torque and high speed leg module for high power humanoid. In *Proceedings of the IEEE/RSJ International Conference on Intelligent Robots and Systems*, pages 4497–4502, 2010.

[4] Sung-Hee Lee, Junggon Kim, Frank Chongwoo Park, Munsang Kim, and James E. Bobrow. Newton-type algorithms for dynamics-based robot movement optimization. *IEEE Transactions on Robotics*, 21(4):657–667, 2005.

[5] Ashutosh Saxena, Lawson L. S. Wong, and Andrew Y. Ng. Learning grasp strategies with partial shape information. In *Proceedings of the Twenty-Third AAAI Conference on Artificial Intelligence*, volume 3, pages 1491–1494, 2008.

[6] Ashutosh Saxena, Justin Driemeyer, and Andrew Y. Ng. Robotic grasping of novel objects using vision. *The International Journal of Robotics Research*, 27(2):157–173, 2008.

[7] Matei T. Ciocarlie and Peter K. Allen. Hand posture subspaces for dexterous robotic grasping. *The International Journal of Robotics Research*, 28(7):851–867, 2009.

[8] Taku Senoo, Akio Namiki, and Masatoshi Ishikawa. High-speed batting using a multi-jointed manipulator. In *Proceedings of the IEEE International Conference on Robotics and Automation*, volume 2, pages 1191–1196, 2004.

[9] Taku Senoo, Akio Namiki, and Masatoshi Ishikawa. Ball control in high-speed batting motion using hybrid trajectory generator. In *Proceedings of the IEEE International Conference on Robotics and Automation*, pages 1762–1767, 2006.

[10] Jens Kober and Jan Peters. Movement templates for learning of hitting and batting. In *Learning Motor Skills*, pages 69–82. Springer, 2014.

[11] Eric Aboaf, Christopher G. Atkeson, and David J. Reinkensmeyer. Task-level robot learning: Ball throwing. Technical report, DTIC Document, 1987.

[12] Heinz Frank, Anton Mittnacht, Thomas Moschinsky, and Friedrich Kupzog. 1-dof-robot for fast and accurate throwing of objects. In *Proceedings of the IEEE Conference on Emerging Technologies & Factory Automation*, pages 1–7, 2009.

[13] Hideyuki Miyashita, Tasuku Yamawaki, and Masahito Yashima. Control for throwing manipulation by one joint robot. In *Proceedings of the IEEE International Conference on Robotics and Automation*, pages 1273–1278, 2009.

[14] Yeuhi Abe, Benjamin Stephens, Michael P. Murphy, and Alfred A. Rizzi. Dynamic whole-body robotic manipulation. In *Proceedings of SPIE Defense, Security, and Sensing*, pages 87410V–87410V, 2013.

[15] Hitoshi Arisumi, Jean-Rémy Chardonnet, Abderrahmane Kheddar, and Kazuhito Yokoi. Dynamic lifting motion of humanoid robots. In *Proceedings of the IEEE International Conference on Robotics and Automation*, pages 2661–2667, 2007.

[16] Takateru Urakubo, Tomoaki Mashimo, and Takeo Kanade. Efficient pulling motion of a two-link robot arm near singular configuration. In *Proceedings of the IEEE/RSJ International Conference on Intelligent Robots and Systems*, pages 1372–1377, 2010.

[17] Michael P. Murphy, Benjamin Stephens, Yeuhi Abe, and Alfred A. Rizzi. High degree-of-freedom dynamic manipulation. In *Proceedings of SPIE Defense, Security, and Sensing*, pages 83870V–83870V, 2012.

[18] Akira Mohri, Seiji Furuno, and Motoji Yamamoto. Trajectory planning of mobile manipulator with end-effector's specified path. In *Proceedings of the IEEE/RSJ International Conference on Intelligent Robots and Systems*, volume 4, pages 2264–2269, 2001.

[19] Eliza Strickland. Fukushima's next 40 years. *Spectrum, IEEE*, 51(3):46–53, 2014.

[20] Keiji Nagatani, Seiga Kiribayashi, Yoshito Okada, Satoshi Tadokoro, Takeshi Nishimura, Tomoaki Yoshida, Eiji Koyanagi, and Yasushi Hada. Redesign of rescue mobile robot quince. In *Proceedings of the IEEE International Symposium on Safety, Security, and Rescue Robotics*, pages 13–18, 2011.

[21] Kui Qian, Aiguo Song, Jiatong Bao, and Huatao Zhang. Small teleoperated robot for nuclear radiation and chemical leak detection. *International Journal of Advanced Robotic Systems*, 9, 2012.

[22] Ryuma Niiyama, Akihiko Nagakubo, and Yasuo Kuniyoshi. Mowgli: A bipedal jumping and landing robot with an artificial musculoskeletal system. In *Proceedings of the IEEE International Conference on Robotics and Automation*, pages 2546–2551, 2007.

[23] Ryuma Niiyama, Satoshi Nishikawa, and Yasuo Kuniyoshi. Biomechanical approach to open-loop bipedal running with a musculoskeletal athlete robot. *Advanced Robotics*, 26(3-4):383–398, 2012.

[24] Keisuke Arikawa and Tsutomu Mita. Design of multi-dof jumping robot. In *Proceedings of the IEEE International Conference on Robotics and Automation*, volume 4, pages 3992–3997, 2002.

[25] Sang-Ho Hyon and Tsutomu Mita. Development of a biologically inspired hopping robot-" kenken". In *Proceedings of the IEEE International Conference on Robotics and Automation*, volume 4, pages 3984–3991, 2002.

[26] Sanghak Sung and Youngil Youm. Landing motion control of articulated legged robot. In *Proceedings of the IEEE International Conference on Robotics and Automation*, pages 3230–3236, 2007.

[27] Maarten F. Bobbert and Gerrit Jan van Ingen Schenau. Coordination in vertical jumping. *Journal of biomechanics*, 21(3):249–262, 1988.

[28] Jackie L. Hudson. Coordination of segments in the vertical jump. *Medicine & Science in Sports & Exercise*, 18(2):242–251, 1986.

[29] Ian D. Walker. The use of kinematic redundancy in reducing impact and contact effects in manipulation. In *Proceedings of the IEEE International Conference on Robotics and Automation*, pages 434–439, 1990.

[30] Ian D. Walker. Impact configurations and measures for kinematically redundant and multiple armed robot systems. *IEEE Transactions on Robotics and Automation*, 10(5):670–683, 1994.

[31] Jong Hyeon Park and Hoam Chung. Impedance control and modulation for stable footing in locomotion of biped robots. In *Proceedings of the IEEE/RSJ International Conference on Intelligent Robots and Systems*, volume 3, pages 1786–1791, 1999.

[32] Svetlana Rapoport, Joseph Mizrahi, Eitan Kimmel, Oleg Verbitsky, and Eli Isakov. Constant and variable stiffness and damping of the leg joints in human hopping. *Journal of Biomechanical Engineering*, 125(4):507–514, 2003.

[33] Claire T. Farley and David C. Morgenroth. Leg stiffness primarily depends on ankle stiffness during human hopping. *Journal of Biomechanics*, 32(3):267–273, 1999.

[34] Vladimir M. Zatsiorsky. *Kinetics of human motion*. Human Kinetics, 2002.

[35] Tsuneo Yoshikawa. Manipulability of robotic mechanisms. *The International Journal of Robotics Research*, 4(2):3–9, 1985.

[36] Lorenzo Sciavicco and Bruno Siciliano. A solution algorithm to the inverse kinematic problem for redundant manipulators. *IEEE Journal of Robotics and Automation*, 4(4):403–410, 1988.

[37] Daniel E. Whitney. The mathematics of coordinated control of prosthetic arms and manipulators. *Journal of Dynamic Systems, Measurement, and Control*, 94(4):303–309, 1972.

[38] Marko Vukobratovic and M. Kircanski. A dynamic approach to nominal trajectory synthesis for redundant manipulators. *IEEE Transactions on Systems, Man and Cybernetics*, (4):580–586, 1984.

[39] M. Kirćanski and M. Vukobratović. Trajectory planning for redundant manipulators in the presence of obstacles. In *Theory and Practice of Robots and Manipulators*, pages 57–63. Springer, 1985.

[40] Richard M. Murray, Zexiang Li, S. Shankar Sastry, and S. Shankara Sastry. *A mathematical introduction to robotic manipulation*. CRC press, 1994.

[41] Eric Marchand, François Chaumette, and Alessandro Rizzo. Using the task function approach to avoid robot joint limits and kinematic singularities in visual servoing. In *Proceedings of the IEEE/RSJ International Conference on Intelligent Robots and Systems*, volume 3, pages 1083–1090, 1996.

[42] Fumitoshi Matsuno and Hiroki Sato. Trajectory tracking control of snake robots based on dynamic model. In *Proceedings of the IEEE International Conference on Robotics and Automation*, pages 3029–3034, 2005.

[43] Jinhyun Kim, Giacomo Marani, Wan Kyun Chung, and Junku Yuh. Task reconstruction method for real-time singularity avoidance for robotic manipulators. *Advanced Robotics*, 20(4):453–481, 2006.

[44] D. Zlatanov, Robert G. Fenton, and Beno Benhabib. Singularity analysis of mechanisms and robots via a motion-space model of the instantaneous kinematics. In *Proceedings of the IEEE International Conference on Robotics and Automation*, pages 980–985, 1994.

[45] D. Zlatanov, R. G. Fenton, and B. Benhabib. A unifying framework for classification and interpretation of mechanism singularities. *Journal of Mechanical Design*, 117(4):566–572, 1995.

[46] K. Sugimoto, J. Duffy, and K. H. Hunt. Special configurations of spatial mechanisms and robot arms. *Mechanism and Machine Theory*, 17(2):119–132, 1982.

[47] C. H. Liu and Shengchia Cheng. Direct singular positions of 3rps parallel manipulators. *Journal of Mechanical Design*, 126(6):1006–1016, 2004.

[48] Vincent Kent Chan and Imme Ebert-Uphoff. Investigation of the deficiencies of parallel manipulators in singular configurations through the jacobian space. In *Proceedings of the IEEE International Conference on Robotics and Automation*, volume 2, pages 1313–1320, 2001.

[49] Jean-Pierre Merlet. Singular configurations of parallel manipulators and grassmann geometry. *The International Journal of Robotics Research*, 8(5):45–56, 1989.

[50] Jean-Pierre Merlet. On the infinitesimal motion of a parallel manipulator in singular configurations. In *Proceedings of the IEEE International Conference on Robotics and Automation*, pages 320–325, 1992.

[51] Ilian A. Bonev, Dimiter Zlatanov, and Cleḿent M. Gosselin. Singularity analysis of 3-dof planar parallel mechanisms via screw theory. *Journal of Mechanical Design*, 125(3):573–581, 2003.

[52] Bruno Monsarrat and Clément M. Gosselin. Singularity analysis of a three-leg six-degree-of-freedom parallel platform mechanism based on grassmann line geometry. *The International Journal of Robotics Research*, 20(4):312–328, 2001.

[53] Shaheen Ahmad and Shengwu Luo. Analysis of kinematic singularities for robot manipulators in cartesian coordinate parameters. In *Proceedings of the IEEE International Conference on Robotics and Automation*, pages 840–845, 1988.

[54] Dinesh K. Pai and M. C. Leu. Generic singularities of robot manipulators. In *Proceedings of the IEEE International Conference on Robotics and Automation*, pages 738–744, 1989.

[55] Nazareth S. Bedrossian. Classification of singular configurations for redundant manipulators. In *Proceedings of the IEEE International Conference on Robotics and Automation*, pages 818–823, 1990.

[56] Lars Nielsen, Carlos Canudas De Wit, and Per Hagander. Controllability issues of robots in singular configurations. In *Proceedings of the IEEE International Conference on Robotics and Automation*, pages 2210–2215, 1991.

[57] F. L. Litvin, Zhang Yi, V. Parenti Castelli, and C. Innocenti. Singularities, configurations, and displacement functions for manipulators. *The International Journal of Robotics Research*, 5(2):52–65, 1986.

[58] Krzysztof Tchoń and Robert Muszyński. Singularities of nonredundant robot kinematics. *The International Journal of Robotics Research*, 16(1):60–76, 1997.

[59] Roy Featherstone and David Orin. Robot dynamics: equations and algorithms. In *Proceedings of the IEEE International Conference on Robotics and Automation*, pages 826–834, 2000.

[60] V. Mata, S. Provenzano, F. Valero, and J. I. Cuadrado. Serial-robot dynamics algorithms for moderately large numbers of joints. *Mechanism and machine Theory*, 37(8):739–755, 2002.

[61] Abhinandan Jain and Guillermo Rodriguez. Diagonalized lagrangian robot dynamics. *IEEE Transactions on Robotics and Automation*, 11(4):571–584, 1995.

[62] Frank C. Park, James E. Bobrow, and Scott R. Ploen. A lie group formulation of robot dynamics. *The International Journal of Robotics Research*, 14(6):609–618, 1995.

[63] Roy Featherstone. The calculation of robot dynamics using articulated-body inertias. *The International Journal of Robotics Research*, 2(1):13–30, 1983.

[64] Tsuneo Yoshikawa. Dynamic manipulability of robot manipulators. In *Proceedings of the IEEE International Conference on Robotics and Automation*, volume 2, pages 1033–1038, 1985.

[65] Pasquale Chiacchio, Stefano Chiaverini, Lorenzo Sciavicco, and Bruno Siciliano. Reformulation of dynamic manipulability ellipsoid for robotic manipulators. In *Proceedings of the IEEE International Conference on Robotics and Automation*, pages 2192–2197, 1991.

[66] Haruhiko Asada. A geometrical representation of manipulator dynamics and its application to arm design. *Journal of Dynamic Systems, Measurement, and Control*, 105(3):131–142, 1983.

[67] J. R. Singh and J. Rastegar. Optimal synthesis of robot manipulators based on global dynamic parameters. *The International Journal of Robotics Research*, 11(6):538–548, 1992.

[68] Oussama Khatib and Joel Burdick. Optimization of dynamics in manipulator design: The operational space formulation. *International Journal of Robotics and Automation*, 2(2):90–98, 1987.

[69] Michael T. Rosenstein and Roderic A. Grupen. Velocity-dependent dynamic manipulability. In *Proceedings of the IEEE International Conference on Robotics and Automation*, volume 3, pages 2424–2429, 2002.

[70] Alan P. Bowling and ChangHwan Kim. Velocity effects on robotic manipulator dynamic performance. *Journal of Mechanical Design*, 128(6):1236–1245, 2006.

[71] Chia-Yu E. Wang, Wojciech K. Timoszyk, and James E. Bobrow. Payload maximization for open chained manipulators: finding weightlifting motions for a puma 762 robot. *IEEE Transactions on Robotics and Automation*, 17(2):218–224, 2001.

[72] Kevin Lawrence Brown. *Design and analysis of robots that perform dynamic tasks using internal body motion*. PhD thesis, Massachusetts Institute of Technology, 1994.

[73] Takateru Urakubo, Hiroki Yoshioka, Tomoaki Mashimo, and Xianglong Wan. Experimental study on efficient use of singular configuration in pulling heavy objects with two-link robot arm. In *Proceedings of the IEEE International Conference on Robotics and Automation*, pages 4582–4587, 2014.

[74] Takateru Urakubo, Tomoaki Mashimo, and Takeo Kanade. Optimal placement of a two-link manipulator for door opening. In *Proceedings of the IEEE/RSJ International Conference on Intelligent Robots and Systems*, pages 1446–1451, 2009.

[75] Mark Yim, David Duff, and Ying Zhang. Closed-chain motion with large mechanical advantage. In *Proceedings of the IEEE/RSJ International Conference on Intelligent Robots and Systems*, volume 1, pages 318–323, 2001.

[76] Feng Lin and Robert D. Brandt. An optimal control approach to robust control of robot manipulators. *IEEE Transactions on Robotics and Automation*, 14(1):69–77, 1998.

[77] Yao-Chon Chen. Solving robot trajectory planning problems with uniform cubic b-splines. *Optimal Control Applications and Methods*, 12(4):247–262, 1991.

[78] David G. Hull. Conversion of optimal control problems into parameter optimization problems. *Journal of Guidance, Control, and Dynamics*, 20(1):57–60, 1997.

[79] Nathan Ratliff, Matt Zucker, J. Andrew Bagnell, and Siddhartha Srinivasa. Chomp: Gradient optimization techniques for efficient motion planning. In *Proceedings of the IEEE International Conference on Robotics and Automation*, pages 489–494, 2009.

[80] Shinichiro Nakaoka, Shizuko Hattori, Fumio Kanehiro, Shuuji Kajita, and Hirohisa Hirukawa. Constraint-based dynamics simulator for humanoid robots with shock absorbing mechanisms. In *Proceedings of the IEEE/RSJ International Conference on Intelligent Robots and Systems*, pages 3641–3647, 2007.

[81] Jinichi Yamaguchi, Atsuo Takanishi, and Ichiro Kato. Experimental development of a foot mechanism with shock absorbing material for acquisition of landing surface position information and stabilization of dynamic biped walking. In *Proceedings of the IEEE International Conference on Robotics and Automation*, volume 3, pages 2892–2899, 1995.